6. Amorphous silicon solar cells

In the present chapter, different photovoltaic devices obtained at our laboratory will be presented and their performance analysed. Preliminary results of *p-i-n* structures will be presented and the influence of different strategies, especially those aiming to improve the front contact properties and the optical absorption (light trapping), will be investigated.

6.1. Introduction

Previous chapters dealt with intrinsic and doped hydrogenated amorphous silicon (a-Si:H) layers, so that parameters leading to our best material were identified. Nevertheless, not a straightforward correlation between suitable properties of the different layers and satisfactory performance of the whole device can be established [Rech and Wagner, 1999]. In this chapter, the properties of solar cells deposited at different deposition conditions will be described. Special attention will be paid to the front contact (involving both the transparent conductive oxide (TCO) and the p-type layer) and to light trapping strategies.

As far as the TCO is concerned, both fluorinated tin oxide, SnO_2:F (commercially available as U-type TCO by Asahi Glass Co.), and ZnO:Al coated Asahi-U were used. Asahi-U is a well known material that fulfils the two basic requirements for its application in *superstrate* (*p-i-n*) technology, that is, high transmittance (> 85% over the entire range of interest) and low sheet resistance (R_{sheet} < 10 Ω/□). Besides, it is natively textured, so the optical path of photons is increased by scattering, thus leading to enhanced absorption in the active layer. Unfortunately, SnO_2:F suffers from instability problems that lead to its reduction when exposed to atomic hydrogen (H) rich atmospheres [Antoine and Drevillon 1988, Wanka et al. 1996, Masuda et al. 2002]. The resulting metallic Sn and SnO reduce the transmittance of the front contact, limiting the solar cell conversion efficiency. On the contrary, ZnO:Al exhibits high stability when exposed to H [Kumar and Drevillon 1989, Imamori et al. 2001]. Consequently, ZnO:Al coated Asahi-U substrates were also used in this work, whose combination was expected to join both the suitable electrical and texture properties of Asahi-U and the chemical stability of ZnO:Al. In particular, 50 nm thick ZnO:Al layers, whose deposition details can be found in [Fonrodona 2003], were used.

The properties of the p-type layer must be also carefully considered, as they play a key role on the device performance. High conductivity is required to attain acceptable *built-in* voltage (V_{bi}) and to ensure good contact properties at both the p/i and the p/TCO interfaces. Special attention must be paid to the p/i interface, as it clearly determines the behaviour of solar cells [Herbst et al. 1995, Bauer et al. 1996, Matsui et al. 2003]. Furthermore, optical features do play an important role, as the illumination of the device is commonly performed through the p-layer to enhance hole collection [Guha et al. 1986, Chatterjee et al. 1998]. Low optical absorption in the short wavelength region is required, as carriers generated in the p-type layer do not contribute to the photogenerated current.

In the following sections, solar cells grown with different p-type materials (a-Si:H, nc-Si:H or both) and deposited on either bare or ZnO:Al coated Asahi-U will be described.

6.2. p-type a-Si:H front contact

A dramatic improvement was observed in p-type a-Si:H after annealing the samples (see *Chapter 5*). A doping activation process seemed to occur, which led to higher dark conductivity at room temperature (σ_d) and lower activation energy (E_A). Consequently, an annealing process (1 hour at around 225ºC) after the deposition of the p-type material was carried out during the solar cell growth. Unfortunately, the annealing temperature had to be kept at a relatively low value to permit the use of low cost substrates. The annealing was performed in the Hot-Wire CVD reactor itself, so no air breaks were introduced in the whole process. The structure of the photovoltaic devices presented in this section was

Asahi-U (ZnO:Al)/p(a-Si:H)/i(a-Si:H)/n(a-Si:H)-n(nc-Si:H)/ZnO:Al/Ag/Al

where both bare and ZnO:Al coated Asahi-U were simultaneously employed. The use of a double n-type structure as well as that of a ZnO:Al layer in the back contact are related to different issues concerning the back reflector implementation, which consisted of a silver contact offering excellent reflectivity and an aluminium layer to provide contact easiness. More details concerning the back reflector incorporation will be given in section 6.4.

Table 6.1 shows the deposition conditions for the semiconducting layers constituting our first *p-i-n* device (labelled 030926c). A linear Ta wire resulting in growth rates (r_d) ~ 3 - 4 Å/s was used in this case for the intrinsic and the nc-Si:H doped layers. On the other hand, r_d ~ 7 Å/s were measured for both p- and n-type doped a-Si:H layers.

Layer	***T_s (ºC)***	***T_f (ºC)***	***P (mbar)***	***ϕ_{SiH4} (sccm)***	***D_H (%)***	***[P]/[Si] (%)***	***[B]/[Si] (%)***	***d (nm)***
p	*125*	*1800*	*1.0×10^{-2}*	*4*	*0**	*-*	*1*	*10*
i	*200*	*1700*	*1.0×10^{-2}*	*4*	*0*	*-*	*-*	*250*
n(a)	*200*	*1690*	*1.0×10^{-2}*	*4*	*0*	*1*	*-*	*10*
n(nc)	*200*	*1640*	*3.0×10^{-2}*	*4*	*95*	*1*	*-*	*70*

Table 6.1. *Deposition conditions for layers constituting solar cell 030926c.* B_2H_6 was diluted in hydrogen (95%), so approximately 0.4 sccm of H_2 were in fact added to the mixture.*

The J(V) curve and the corresponding parameters for cell 030926c are shown in Fig. 6.1.

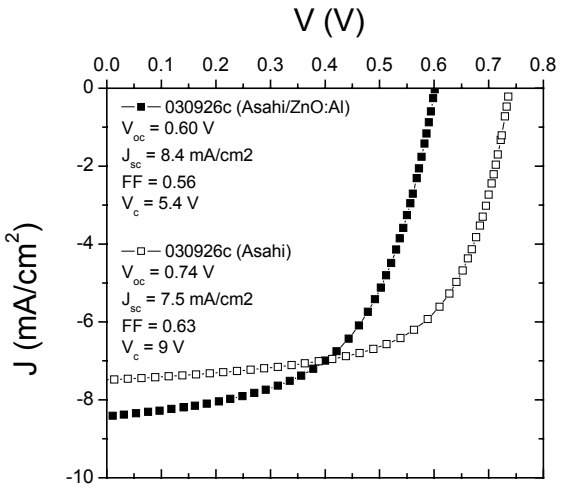

Figure 6.1. *J(V) curves for cell 030926c deposited simultaneously on both bare and ZnO:Al coated Asahi-U.*

Remarkably enhanced performance was achieved on bare Asahi-U, for which an open-circuit voltage (V_{oc}) around 0.74 V and a fill factor (FF) of 0.63 approximately were measured. These values lowered to 0.60 V and 0.56 for the coated substrate. Conversely, higher short-circuit current (J_{sc}) was measured for that sample grown onto the coated

substrate, this result being probably linked to the chemical reduction of Asahi-U. Nevertheless, J_{sc} was too low in both cases to allow acceptable conversion efficiencies.

Additional insight into the solar cell performance could be gained from Variable Illumination Measurements (VIM) as seen in Figure 6.2. The evolution of the open-circuit resistance (R_{oc}) evidenced a similar trend to that observed in a typical *p-i-n* PECVD solar cell, whose VIM curves were extracted from [Merten et al. 1998] (Fig. 6.2(d)). R_{oc} is expected to saturate at high illuminations to a value that can be identified as the series resistance (R_s). In our case, this saturation limit was not reached, thus pointing to a low R_s value (< 2 Ωcm^2) and, consequently, to a reduction of FF only for J_{sc} > 10 mA/cm^2.

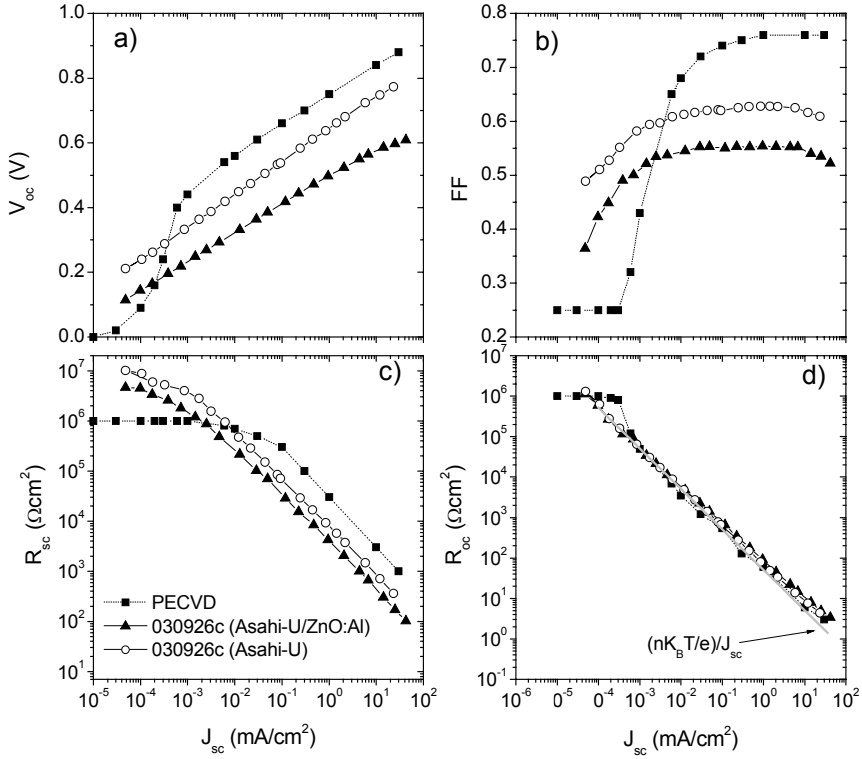

Figure 6.2. *VIM results for cell 030926c. Clear different performance between devices deposited onto Asahi-U or ZnO:Al coated Asahi-U was observed. Typical curves for an a-Si:H p-i-n solar cell [Merten et al. 1998] are also plotted for comparison.*

The saturation of R_{sc} at low illumination levels, which corresponds to the parallel resistance (R_p), reached a very high value (around 10^7 Ωcm^2), thus manifesting the absence of significant leakage currents. Regarding the intermediate illumination range, R_{oc} stayed

very close to the ideal behaviour, as it only separated from the diode curve, $R_{diode} = (nK_BT/e)/J_{sc}$ [Merten et al. 1997], at either very low or very high illumination levels due to R_p and R_s respectively (Fig. 6.2(d)).

As also seen in the J(V) curve, VIM experiments gave evidence of improved photovoltaic operation for solar cells deposited onto bare Asahi-U, whose V_{oc} and FF remained higher over all the illumination range (Fig. 6.2(a) and 6.2(b)). Moreover, the dependence on the substrate could also be observed in R_{sc}, which also exhibited higher values over the whole range of illuminations for the bare Asahi-U substrate. R_{sc} is not expected to depend critically on parasitic effects at intermediate illuminations, so that valuable information concerning the device physics can be obtained from its evolution. In that sense, the collection voltage ($V_c = R_{sc} \cdot J_{sc}$) is linked to the carrier transport and recombination parameters of the intrinsic layer [Merten et al. 1998, Asensi et al. 1999]

$$V_c = R_{sc} \cdot J_{sc} = \frac{\mu\tau_{eff} \cdot V_{bi}^2}{L^2} \tag{6.1}$$

where V_{bi} is the *built-in* potential, L is the thickness of the intrinsic layer and $\mu\tau_{eff}$ is the effective mobility-lifetime product. $\mu\tau_{eff}$ combines the transport properties of both majority and minority carriers, so it is clearly affected by carrier recombination in defects, which contribute negatively to the current. Accordingly, $\mu\tau_{eff}$ is expected to reach high values (above 10^{-8} cm^2/V).

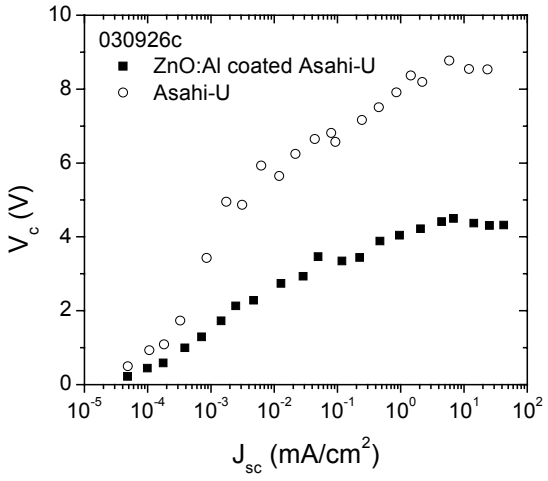

Figure 6.3. *V_c for device 030926c showing the substrate dependence.*

Under standard operating conditions, and for a-Si:H solar cells with proper performance, the most relevant recombination mechanism involves mainly neutral dangling bonds (D^0). Anyhow, that might not be the case when highly defective regions exist as, in this case, recombination due to charged defects (D^+ near the p-type layer and D^- near the n-type one) becomes increasingly important. The evolution of V_c for cell 030926c is presented in Fig. 6.3, where higher values are observed on bare Asahi-U. Improved contact properties leading to lower density of defects near the p/i interface might account for such behaviour.

The above-seen substrate dependence might be related to the presence of H during the growth process. H leads to changes on the optoelectronic properties of the TCO, which depend on the TCO material. As already commented, the H-SnO_2 interaction leads to a reduction process, which lowers the TCO transparency and, consequently, limits J_{sc}. Nevertheless, a beneficial effect arises from that reduction, as a Schottky barrier is built at the TCO/p interface which correlates with the metal-rich region near the TCO surface. This Schottky barrier enhances V_{oc} when compared with TCO materials not showing the above-mentioned reduction (as ZnO:Al) [Drevillon et al. 1989]. Besides, tunnel conduction through the Schottky junction is expected to improve ohmic contact leading to low resistive losses.

As far as the H-ZnO interaction is concerned, some deleterious effects that lower both V_{oc} and FF could be identified. Thus, H is observed to penetrate into ZnO, provoking an increase of the conductivity near its surface [An et al. 1994, Kubon et al. 1996]. As a result, an accumulation layer at the surface of the n-type ZnO is formed. According to the semiconducting junction theory, this interaction induces the depletion of the p-layer, which finally leads to a stronger down bending of the bands in the region close to the junction. This down bending leads to larger depletion zones, which affect the contact properties, mainly increasing R_s and reducing its ohmic character as tunnel conduction becomes hindered. Furthermore, not only H is expected to play a role, as an additional deleterious effect might result from the ZnO:Al coating itself, which is known to increase R_s and, consequently, to lower FF [Kubon et al. 1996]. In that sense, results shown in section 5.4.2 already anticipated a significant voltage drop at the ZnO:Al/p interface. Unfortunately, the behaviour of Asahi-U was not tested in that study. Therefore, thinner ZnO:Al coatings might have been needed to achieve better results [Franken et al. 2004]. Hence, the ZnO:Al

coating should be thick enough to prevent the reduction of Asahi-U, while maintaining low R_s. Besides, thick ZnO:Al layers might lead to increased optical losses due to optical absorption, especially in the short wavelength region of the spectrum [Seto et al. 2003].

In our case, p-type a-Si:H was grown with no hydrogen dilution, so relatively low H concentration was involved, making it possible for Asahi-U to keep its suitable properties. Moreover, it has been reported that the growth of a very thin (around 10 nm) a-Si:H layer onto Asahi-U protects it from further degradation [Imamori et al. 2001].

Referring once more to the J(V) curve of cell 030926c (Fig. 6.1), it was clearly seen that too low J_{sc} values were achieved regardless the substrate used, especially if we consider that a back reflector had been implemented. In order to get additional insight into the current generation, the spectral response on bare Asahi-U was measured (Fig. 6.4).

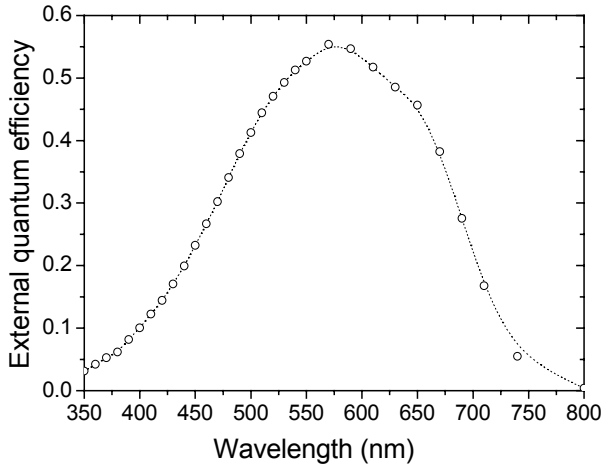

Figure 6.4. *Spectral response of cell 030926c exhibiting especially significant collection problems at short wavelengths.*

Very low quantum efficiencies at short wavelengths leading to low J_{sc} can be observed, which might be imputable to the front p-type a-Si:H layer, whose absorption coefficient was remarkably high. In that sense, a-SiC:H, whose band gap is higher than the a-Si:H one, is widely employed [Merten 1996, Franken et al. 2004, Müller et al. 2003] to lower optical losses while keeping good enough electrical properties. On the other hand, thinner p-type a-Si:H layers might also help to reduce optical losses. Nevertheless, the low doping efficiency observed in our previous studies limited this option as will be shown next.

In order to get deeper insight into the role of the amorphous p-type layer, solar cells with p-type layers exhibiting varying thicknesses (d_p) and doping ratios were grown on bare Asahi-U substrates. Regarding the thickness study, d_p = 5 nm (031201c), 10 nm (031127c), 20 nm (031124c) and 40 nm (031205c) were tested. Small d_p was expected to minimize optical absorption, thus leading to enhanced photogeneration. Anyhow, d_p had to be kept large enough to allow the formation of V_{bi}. All layers were grown at a [B]/[Si] ratio of 3%, except for cell 031205c (d_p = 40 nm), for which a ratio of 1% was used. Moreover, this cell had a thicker intrinsic layer (0.4 vs. 0.25 μm in the other devices). Figure 6.5(a) shows the measured spectral response for the different devices, which give evidence of a clear dependence on d_p.

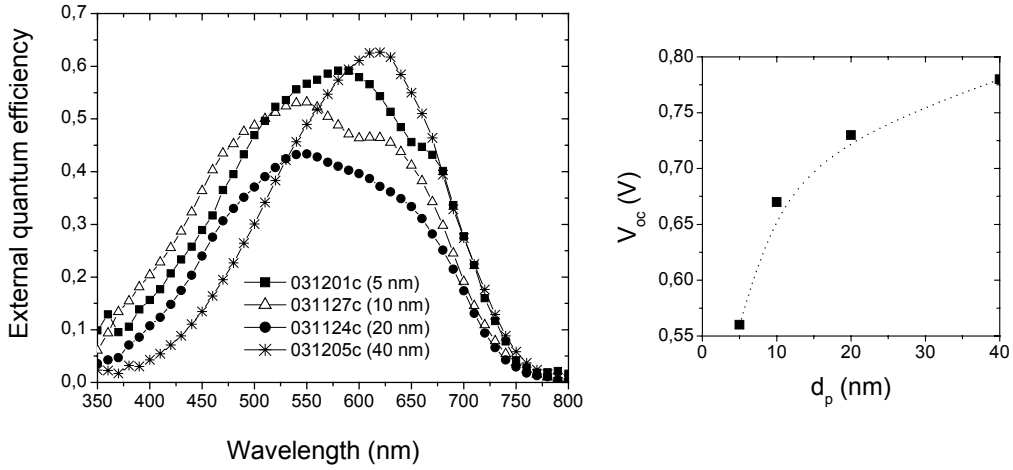

a) *b)*

Figure 6.5. *Spectral response (a) and V_{oc} (b) for solar cells exhibiting different p-type layer thickness.*

The lowest external quantum efficiencies in the short wavelength region were observed for cell 031205c, whose p-type layer thickness (40 nm) led to very significant (or even critical) optical losses. On the other hand, enhanced photogeneration in this region was achieved for samples exhibiting d_p ~ 20 and 10 nm. Nevertheless, further reduction in d_p (5 nm) did not lead to higher quantum efficiencies. Furthermore, Figure 6.5(b) clearly showed the improved V_{oc} at increased d_p. In particular, a minimum d_p was necessary to ensure the formation of the *built-in* voltage and a proper charge carrier collection. Therefore, d_p had to be larger than the depletion zone to allow the correct performance of the device, leading to acceptable V_{oc} values, as also reported for PECVD devices [Isomura et al. 1993]. The

thickness of the depletion zone is correlated with the [B]/[Si] ratio, so that larger (narrower) depletion zones are obtained at lower (higher) doping. Consequently, the role of the doping ratio was also studied.

Solar cells with [B]/[Si] ratios of 1% (030926c), 3% (031127c) and 10% (031027c) were compared while keeping d_p constant at 10 nm. Highly doped p-type layers give place to increased V_{bi}, though they result in high defect densities at the p/i interface, which lead to recombination losses. Thus, a compromise must be reached between sufficiently high V_{bi} and low defect density. Furthermore, the growth of high-quality p-type a-Si:H by Hot-Wire CVD proved to be a difficult step, and electrical properties comparable to those required could only be achieved at very high doping ratios, for which a dramatic influence of boron diffusion leading to increased defects at the interface can be expected. Figure 6.6 shows the J(V) curves for solar cells under study, where a dramatic worsening at increasing doping ratios is observed. In fact, several cells deposited at [B]/[Si] = 10% were shunted. Although p-type layers deposited at high doping ratios (5 and 10%) showed quite satisfactory electrical properties (*Chapter 5*), results shown in this section indicated that doping-induced defects seemed to determine the device operation, so that low doping ratios were required to achieve acceptable performance despite the resulting lower σ_d.

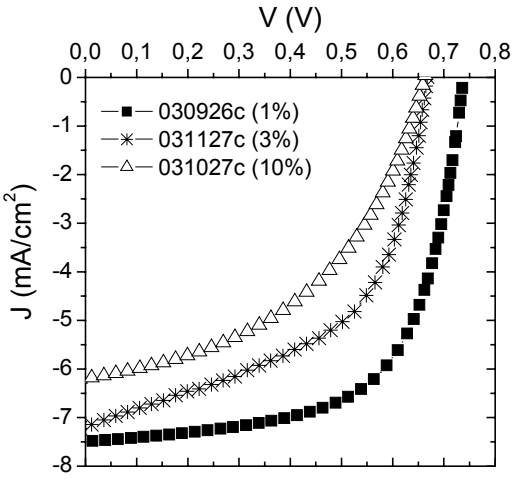

Figure 6.6. *J(V) curves of solar cells with p-layers deposited at different [B]/[Si] ratios.*

In summary, and as far as purely amorphous front contacts are concerned, thick p-layers, which unfortunately exhibited very high optical absorption, deposited at low [B]/[Si] ratios, led to our best solar cells. That approach was applied to the deposition of one last

cell incorporating a p-type a-Si:H layer (031205c), whose spectral response has already been presented in Fig. 6.5(a). In this case, d_p ~ 40 nm and [B]/[Si] = 1% were chosen. Moreover, d_i = 0.4 μm was selected to increase the absorption of the active layer. This approach led to our best solar cell with entirely amorphous front contact, whose J(V) curve and deposition conditions are presented in Fig. 6.7 and Table 6.2 respectively. Linear Ta wires, which led to r_d around 3 Å/s for the a-Si:H intrinsic and the nc-Si:H n-type doped layers, and to r_d of approximately 7 Å/s for the a-Si:H doped material, were employed.

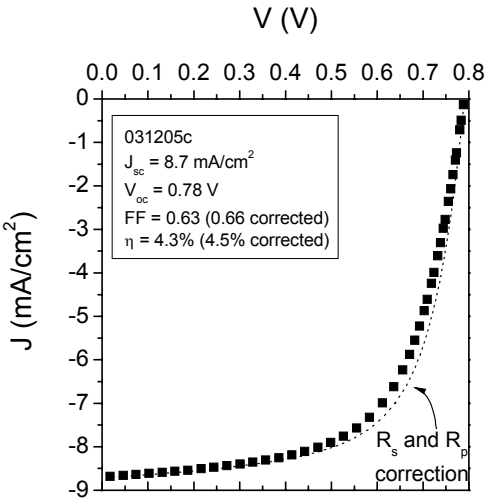

Figure 6.7. *J(V) curve of cell 031205c. The dotted line corresponds to the J'(V') calculated after conveniently considering the influence of parasitic resistances.*

Layer	***T_s (ºC)***	***T_f (ºC)***	***P (mbar)***	***ϕ_{SiH4} (sccm)***	***D_H (%)***	***[P]/[Si] (%)***	***[B]/[Si] (%)***	***d (nm)***
p	*125*	*1800*	*1.0×10^{-2}*	*4*	*0**	*-*	*1*	*40*
i	*200*	*1710*	*1.0×10^{-2}*	*4*	*0*	*-*	*-*	*400*
n(a)	*200*	*1680*	*1.0×10^{-2}*	*4*	*0*	*1*	*-*	*10*
n(nc)	*200*	*1610*	*3.0×10^{-2}*	*4*	*95*	*1*	*-*	*70*

Table 6.2. *Deposition conditions for layers constituting solar cell 031205c. * B_2H_6 was diluted in hydrogen (95%), so around 0.4 sccm of H_2 were in fact added to the mixture.*

VIM measurements (Fig. 6.8) gave us some additional insight into the solar cell operation. V_{oc} was observed to exhibit a satisfactory evolution (Fig. 6.8(a)), reaching relatively high values. On the other hand, parasitic effects were observed to limit the photovoltaic

performance. R_p (Fig. 6.8(c)) reached a value of ~ 10^4 Ωcm^2, which was around one order of magnitude lower than those values typically required to avoid significant leakage currents. Leakage currents were expected to be effectively reduced by dry-etching the devices by following the same approach as that presented in *Chapter 5*, where dry-etching of doped samples was performed to analyse electrical properties perpendicular to the substrate. Nevertheless, several attempts were carried out which led to shunted devices. Consequently, further investigation is required involving the dry-etching step, so that a more controlled process can be achieved. Similarly, R_s exhibited a relatively large value when compared with standard PECVD devices, so that a certain saturation seemed to be observed at high illumination (Fig. 6.8(d)). The increase in R_s could be linked to the use of a thick p-type layer, which was expected to increase R_s due to the poor transport properties of p-type a-Si:H. Accordingly, FF (Fig. 6.8(b)) decreased for $J_{sc} > 5$ mA/cm^2.

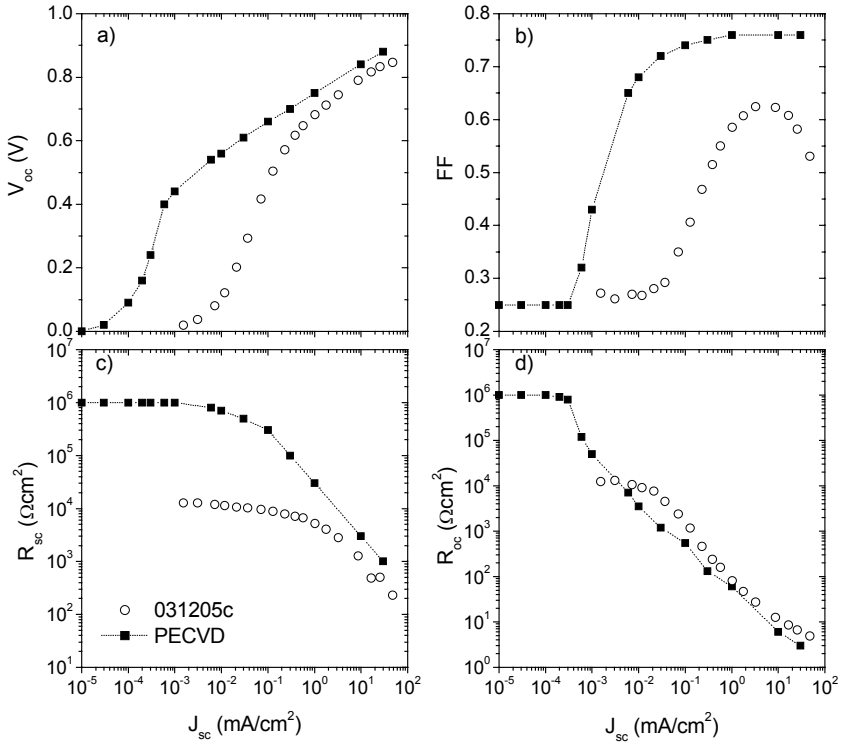

Figure 6.8. *VIM results for cell 031205c. Typical PECVD device data extracted from [Merten et al. 1998].*

The influence of R_p and R_s can be analysed by taking into account the equivalent electrical circuit of a solar cell (Fig. 2.7) presented in section 2.3. On one hand, an additional voltage drop is provoked by R_s, so that the real voltage over the *p-i-n* structure (V') results

$$V' = V - J \cdot R_s \tag{6.2}$$

On the other hand, R_p leads to leakage currents given by

$$J_{leak} = \frac{V'}{R_p} \tag{6.3}$$

Consequently, the current density after removing the influence of parasitic elements results

$$J' = J - \frac{V'}{R_p} \tag{6.4}$$

The J'(V') curve of cell 031205c obtained after removing the influence of parasitic resistances is also presented in Figure 6.7, where a slight improvement, especially in FF (from 0.63 to 0.66), can be observed. Nevertheless, neither R_s nor R_p were observed to drastically limit the behaviour of our solar cell at one sun illumination in this case.

6.3. p-type nc-Si:H front contact

Suitable electrical properties and low optical absorption (especially at short wavelengths) have led p-type nc-Si:H to its application in amorphous silicon solar cells [Guha et al. 1986, Rath and Schropp 1998, Miyajima et al. 2003]. Increased V_{bi}, and consequently V_{oc}, is seen when highly doped p- layers exhibiting very low E_A are used. Anyhow, some drawbacks arise from the use of nc-Si:H p-layers, namely, TCO reduction due to the large concentration of H, and back diffusion of carriers due to the band discontinuity (Figure 6.9) [Van Cleef et al. 1997, Chatterjee et al. 1998].

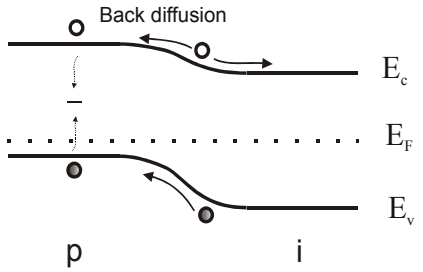

Figure 6.9. *Back diffusion of photogenerated carriers. In this case, electrons (o) back diffuse to the p-type layer contributing negatively to the majority carrier (holes) current.*

As seen in section 6.2, the use of uncoated Asahi-U was preferable in entirely amorphous devices. Anyhow, larger H concentration is involved in the growth of nc-Si:H, so ZnO:Al coated Asahi-U was used in this section to prevent TCO degradation. d_p around 50 nm, which was expected to ensure the formation of the *built-in* voltage while allowing a sufficient amount of light to reach the active layer, was used. Table 6.3 shows the growth conditions of the different semiconducting layers that constituted the solar cell under study (labelled 030304c). In this case, no annealing was performed after the deposition of the p-type layer, as suitable optoelectronic properties were already achieved at 125ºC (see *Chapter 5*). Moreover, no back reflector (which had been used in the previous section) was incorporated in this case. On the other hand, r_d was 3 - 4 Å/s for both the intrinsic and the nanocrystalline p-type layer, whereas $r_d \sim 9$ Å/s was measured for the n-type material.

Layer	T_s (ºC)	T_f (ºC)	*P (mbar)*	ϕ_{SiH4} (sccm)	D_H (%)	[P]/[Si] (%)	[B]/[Si] (%)	*d(nm)*
p	*125*	*1820*	3×10^{-2}	*4*	*96*	-	*1*	*50*
i	*200*	*1610*	1×10^{-2}	*4*	*0*	-	-	*270*
n	*200*	*1640*	1×10^{-2}	*4*	*0*	*1*	-	*20*

Table 6.3. *Deposition conditions for cell 030304c.*

Regarding the structure of the solar cell, a standard *p-i-n* architecture was selected

Asahi-U/ZnO:Al/p(nc-Si:H)/i(a-Si:H)/n(a-Si:H)/Cr/Al

The J(V) curve obtained at AM1.5 illumination is shown in Fig. 6.10. J_{sc} reached a value around 8.2 mA/cm^2, which was still too low to permit acceptable efficiencies. Nevertheless, it is worth mentioning that this value was similar to those seen in purely a-Si:H based solar cells (030926c), despite the lack of a back reflector. On the other hand, low V_{oc} values below 0.7 V were measured. In this case, the role of the substrate texture on the operation of solar cells with p-type nc-Si:H was further studied. A solar cell (030226c) was deposited at similar growth conditions than cell 030304c (except for the use of higher dopant concentration, 5%, for the p-type layer) on both ZnO:Al coated flat glass and ZnO:Al coated Asahi-U. Higher V_{oc} and lower J_{sc} were observed for the device grown on

the flat substrate. The lower V_{oc} in the coated Asahi-U substrate might be linked to a deleterious effect of the roughness due to the increased electric field at sharp features [Rech and Wagner, 1999], where electric charge accumulates. On the other hand, the increased current on Asahi-U could be explained by enhanced light scattering.

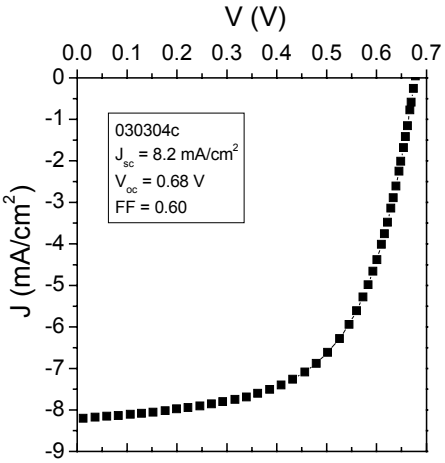

Figure 6.10. *J(V) curve for cell 030304c. The corresponding parameters can be seen in the inset.*

In summary, the use of p-type nc-Si:H did not lead to enhanced performance of our devices when compared with a-Si:H. Thus, our best device obtained with a nanocrystalline p-type layer (030304c) exhibited a poorer performance than either solar cell 030926c or 031205c (section 6.2). Nevertheless, a slight improvement in J_{sc} could be observed, as comparable J_{sc} values to those measured in cell 030926c were determined despite the lack of a back reflector. Unfortunately, both lower V_{oc} and FF were measured for cell 030304c leading to a poor overall behaviour. Our results could be related to the high crystallinity of our p-type material. Recent results give evidence of clearly enhanced performance when nc-Si:H p-type layers prepared near the transition to amorphous growth are employed [Kumar et al. 2004]. In particular, the valence band offset between highly crystalline doped p- and intrinsic layers might lead to low V_{oc}, while, in addition, highly crystalline material is unstable leading to irreversible changes in the solar cell performance.

6.4. p-type double structure: nc-Si:H/a-Si:H front contact

The addition of a buffer layer between the p-type and the intrinsic layers leads to less defective p/i regions [Isomura et al. 1993, Taira et al. 2003]. Besides, the use of a high

band gap material for the buffer lowers back diffusion of carriers [Schropp et al. 1994, Wang et al. 2000] and reduces the diffusion of boron into the intrinsic layer, which worsens the solar cell performance leading to S-shaped J(V) curves [Rath and Schropp, 1998]. In particular, a combination of p-type nc-Si:H and a-Si:H in a double structure (Fig. 6.11), which has already been successfully applied in a-Si:H based solar cells [Franken et al. 2004], is expected to effectively block electrons back diffusing [Chaterjee et al. 1998]. Besides, this approach allows good electrical contact between the TCO and the nc-Si:H p-type layer while maintaining suitable V_{oc} by introducing the a-Si:H p-type layer [Rech and Wagner 1999, Müller et al. 2001, Franken et al. 2004].

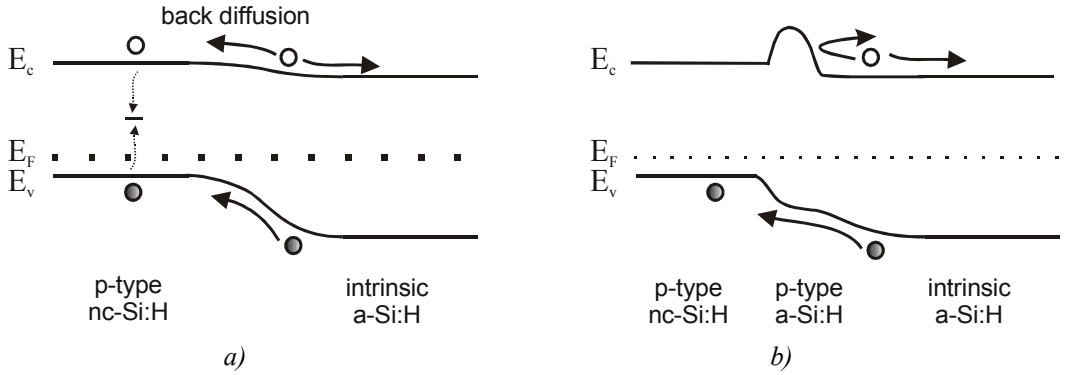

Figure 6.11. *Back diffusion of minority carriers near the p/i interface (a) and insertion of a p-type a-Si:H thin layer to reduce back diffusion (b).*

As also seen in the previous section, ZnO:Al coated Asahi-U was employed, as the growth of p-type nc-Si:H was observed to worsen the properties of the TCO. Consequently, the general structure of the solar cells deposited in this section was

Asahi-U/ZnO:Al/p(nc-Si:H)-p(a-Si:H)/i(a-Si:H)/n(a-Si:H)-n(nc-Si:H)/Cr/Al

A double n-type layer was incorporated for reasons concerning the future implementation of the back reflector. An inverted-basket shaped wire was employed, whereas the deposition conditions for our first device with the above mentioned structure (030305c) were those leading to our state-of-the-art material as seen in *Chapters 4* and *5* (Table 6.4). Deposition rates around 3 - 4 Å/s for the active and the nc-Si:H doped layers were measured, whereas r_d was approximately 10 Å/s for the a-Si:H doped ones.

Layer	T_s (ºC)	T_f (ºC)	P (mbar)	ϕ_{SiH4} (sccm)	D_H (%)	[P]/[Si] (%)	[B]/[Si] (%)	d(nm)
p(nc)	125	1820	3.0×10^{-2}	4	96	-	1	50
p(a)	200	1900	1.0×10^{-2}	4	0*	-	1	10
I	200	1610	1.0×10^{-2}	4	0	-	-	270
n(a)	200	1640	1.0×10^{-2}	4	0	1	-	10
n(nc)	200	1740	3.0×10^{-2}	4	95	1	-	70

Table 6.4. *Deposition conditions for cell 030305c. * B_2H_6 was diluted in hydrogen (95%), so 0.4 sccm of H_2 were added to the gas mixture.*

As a first result, Figure 6.12 shows the J(V) curve obtained at standard illumination.

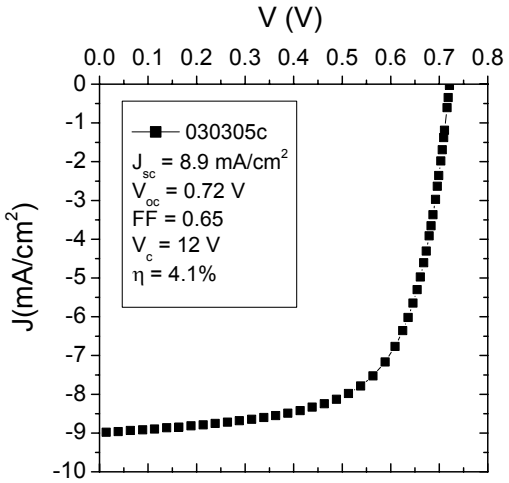

Figure 6.12. *J(V) curve for cell 030305c. The corresponding cell parameters can be seen in the inset.*

An acceptable fill factor was achieved (FF ~ 0.65), this result being probably related to enhanced properties at the front contact junctions. Besides, V_c reached a value of around 12 V, which also pointed out improved properties in the front contact leading to lower defect density near the p/i interface. On the other hand, V_{oc} ~ 0.72 V was obtained, this value being lower than the one achieved in entirely amorphous devices as seen in section 6.2 (030926c or 031205c).

VIM measurements for cell 030305c can also be seen in Fig. 6.13. Both R_{sc} (Fig. 6.13(c)) and R_{oc} (Fig. 6.13(d)) attested quite satisfactory performance. Relatively high R_{sc} values

were observed at intermediate illuminations leading to higher V_c values than those achieved in previously shown devices. Moreover, the evolution of R_{oc} was almost identical to that presented for the reference PECVD device considered [Merten et al. 1998], that is, very low R_s value and diode-like behaviour at intermediate illuminations. Accordingly, the FF (Fig. 6.13(b)) exhibited a slight decrease only for $J_{sc} \geq 10$ mA/cm^2. Nevertheless, and as already seen in the J(V) curve, relatively low V_{oc} was measured over the entire illumination range.

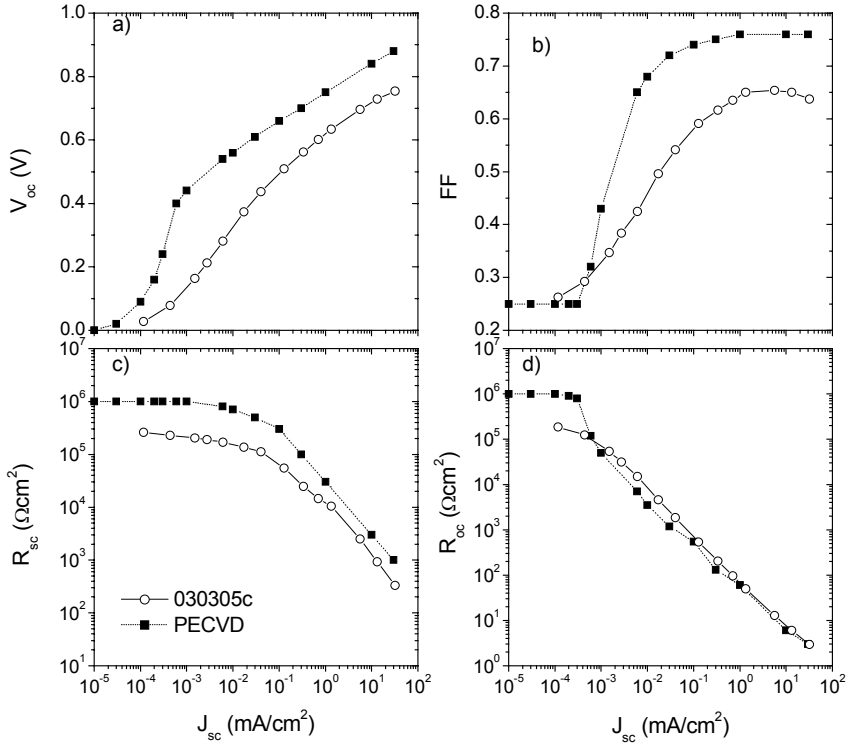

Figure 6.13. *VIM results for cell 030305c.*

Additional studies were performed while keeping the p-type double structure. In particular, the effect of the gas phase doping concentration was evaluated. On one hand, a doping concentration of 0.1% instead of 1% was used for the amorphous doped layers (cell 030306c). In addition, different doping ratios for the nc-Si:H layers (5% for p-type and 2% for n-type) were analysed (cell 030317c) following those results observed in nc-Si:H devices grown at our laboratory [Fonrodona 2003]. The corresponding J(V) curves for the different cells involved in this study are presented in Fig. 6.14. The best performance was obtained at doping ratios around 1% (cell 030305c). Low J_{sc} and V_{oc} values were obtained

for cell 030306c, which might be indicative of poor charge collection. In particular, the use of low doping concentrations might have required the use of larger d_p values. On the other hand, higher doping concentrations for the nanocrystalline layers (cell 030317c) led to poor performance, probably due to diffusion effects or cross contamination issues. Thus, and in accordance with presented results, doping concentrations of 1% for all doped layers were selected for the subsequent work.

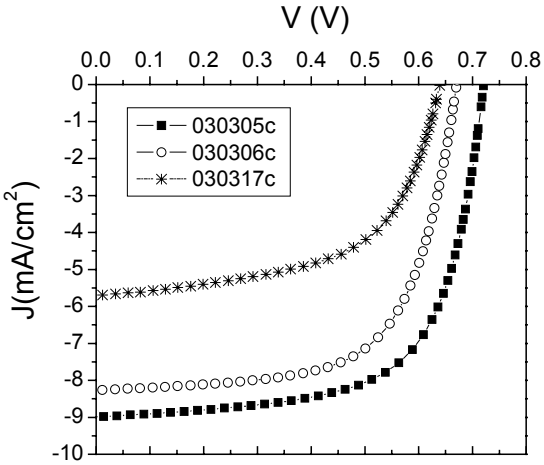

Figure 6.14. *J(V) curves for solar cells exhibiting p-type double layer with varying doping ratios. 1% was used for all doped layers in cell 030305c (■). 1% and 0.1% were used for a-Si:H and nc-Si:H doped layers, respectively, in cell 030306c (○) and, finally, 1% for a-Si:H doped layers and 5% and 2% for p-type and n-type nc-Si:H layers respectively were used in cell 030317c (□).*

Summarizing, the use of a p-type double structure and ZnO:Al coated Asahi-U substrates led to the deposition of devices exhibiting acceptable V_{oc} and FF values, although J_{sc} was still considerably low. In order to increase J_{sc}, the implementation of a back reflector, as in the case of purely amorphous devices, was analysed in this case too. Moreover, further experiments should be performed to optimise the thickness of the p-type doped layers, thus leading to high V_{oc} while keeping low optical absorption [Franken et al. 2004]. In the next section, results obtained after the incorporation of the back reflector will be described.

6.5. Back reflector

In order to increase the absorption of light and, consequently, the carrier generation, light trapping strategies are applied. The use of textured substrate structures in *p-i-n* solar cells

increases the scattering of the incoming photons, so that their optical path is enhanced. On the other hand, the use of a back reflector improves the optical properties of the back contact by increasing its reflectivity (especially in the long wavelength region of the spectrum) [Schropp and Zeman 1998], also leading to an increase of the optical path. The behaviour of light in a *superstrate* (*p-i-n*) cell incorporating light trapping strategies both at the front (textured substrate) and at the back (back reflector) contacts is shown in Fig. 6.15.

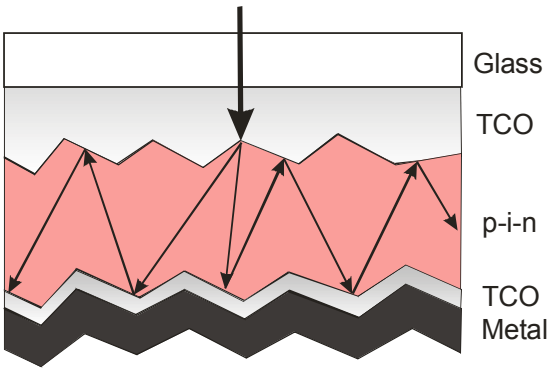

Figure 6.15. *Schematic representation of both front and back contact light trapping strategies.*

Back reflectors usually consist of a combination of a TCO material and a highly reflective metal. Enhanced absorption in the active layer is then accomplished by consecutive reflections. In this work, 80 nm thick ZnO:Al layers were used in combination with double Ag/Al structures. 100 nm thick Ag layers were evaporated on the TCO, as Ag is known to provide excellent reflection properties. In addition, 200 nm thick Al layers were used both as a protection against external factors and as a way to provide satisfactory electrical contact with the corresponding probe. Moreover, the TCO insertion between the n-type layer and the metal prevented Ag diffusion into the semiconducting layer, which would drastically damage its properties and, eventually, limit the device performance. Although the working principle of back reflectors can be easily understood, its application was not a straightforward process. First attempts led to shunted cells, probably due to a degradation process of a-Si:H layers during the ZnO:Al deposition by RF magnetron sputtering. It was not until the addition of the already seen double n-type structure (a-Si:H and nc-Si:H) that back reflectors could be successfully implemented. Moreover, the use of the double n-type structure was also expected to improve the electrical properties of the n/metal junction.

In order to test the role of the back reflector, two solar cells were simultaneously deposited onto identical substrates (ZnO:Al coated Asahi-U) using the growth conditions seen for cell 030305c. A back reflector was added to one of them, whereas a simple Cr/Al contact was evaporated on the second one. Figure 6.16 shows the resulting J(V) curves, where an increase of J_{sc} from 8.5 mA/cm^2 to 10.5 mA/cm^2 with the implementation of the back reflector can be observed. A slight decrease in both V_{oc} and FF was also evidenced, this result being possibly imputable to the persistence of some deleterious effect associated to the back reflector growth process [Bauer et al. 1997].

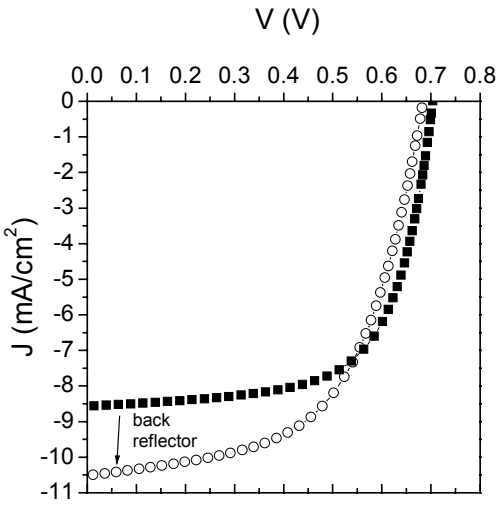

Figure 6.16. *Effect of the back reflector on the solar cell performance.*

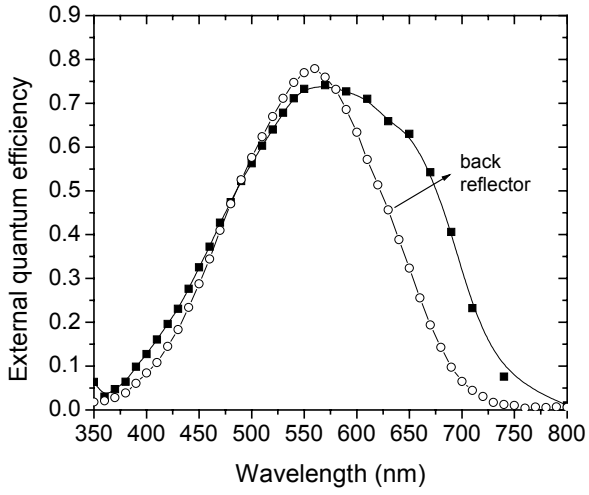

Figure 6.17. *Effect of the back reflector on the external quantum efficiency evidencing enhanced absorption at long wavelengths. These measurements correspond to the same devices plotted in Fig. 6.16.*

Clearer insight into the back reflector effect on the current generation could be gained from spectral response measurements (Fig. 6.17). Enhanced absorption at long wavelengths ($\lambda > 600$ nm) was obtained after the incorporation of the back reflector. Incoming light in the short wavelength region is mainly absorbed near the p/i interface, so not a clear difference could be measured after the back reflector addition. On the other hand, long wavelength radiation is not so effectively absorbed, so enhanced absorption is obtained at increased intrinsic layer thickness or, as in the case under study, after implementing a back reflector.

6.6. Our final step

Results shown in section 6.4 pointed to enhanced photovoltaic operation for those devices incorporating both p-type (front contact) and n-type (back contact) double structures. Accordingly, and once the ability to deposit back reflector structures was proved, further studies were performed on that kind of structure.

Solar cells exhibiting different intrinsic layer thickness (d_i) were tested: 0.2 μm (031203c), 0.3 μm (031202c) and 0.4 μm (031204c). Deposition conditions (Table 6.5) were kept similar to those already presented for cell 030305c. r_d around 3 Å/s for the i- and the nc-Si:H doped layers were measured, whereas r_d was ~ 9 Å/s for the a-Si:H doped layers. Regarding the geometry of the filament, a linear Ta wire was employed in all samples.

Layer	*T_s (ºC)*	*T_f (ºC)*	*P (mbar)*	*ϕ_{SiH4} (sccm)*	*D_H (%)*	*[P]/[Si] (%)*	*[B]/[Si] (%)*	*d(nm)*
p(nc)	*125*	*1830*	*3.0×10^{-2}*	*4*	*96*	*-*	*1*	*50*
p(a)	*125*	*1900*	*1.0×10^{-2}*	*4*	*0**	*-*	*1*	*10*
i	*200*	*1720*	*1.0×10^{-2}*	*4*	*0*	*-*	*-*	*200-400*
n(a)	*200*	*1690*	*1.0×10^{-2}*	*4*	*0*	*1*	*-*	*10*
n(nc)	*200*	*1640*	*3.0×10^{-2}*	*4*	*95*	*1*	*-*	*70*

Table 6.5. *Deposition conditions for cells 031203c, 031202c and 031204c with d_i = 0.2, 0.3 and 0.4 μm.*

Both electrical and optical considerations must be taken into account when evaluating the influence of d_i. The use of thin layers is expected to favour the collection of photogenerated carriers, as they must cover a shorter distance and the internal electric field throughout the active layer is enhanced, both results leading to low recombination probability. Nevertheless, lower absorption leading to a minor production of electron-hole pairs is also achieved. The opposite trend is expected for thick layers, for which larger distances must be covered by the carriers and weak E_i are obtained. Besides, large carrier photogeneration is expected in this case.

The photovoltaic performance of cells under study can be observed in Fig. 6.18, where the J(V) curves at standard illumination conditions are presented. Device 031203c (d_i = 0.2 μm) was too thin to allow proper photovoltaic activity. Thus, clearly lower J_{sc} and V_{oc} than for the other thicknesses were measured. In this case, E_i seemed to be too intense for the doped layers used. Therefore, larger doped layers might have been required to allow the proper formation of the corresponding depletion zones. Additionally, such thin devices were often mechanically degraded. On the other hand, similar results were observed for cells 031202c and 031204c, for which the thickness of the doped layers allowed the proper constitution of V_{bi}. Moreover, the lower collection efficiency in cell 031204c (d_i = 0.4 μm) seemed to be compensated by its higher optical absorption.

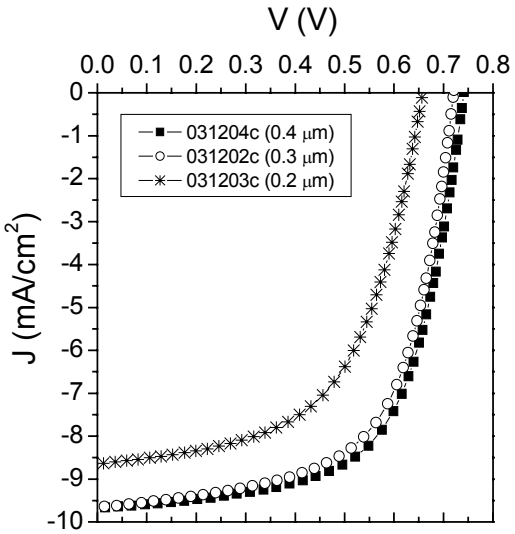

Figure 6.18. *J(V) curves as a function of d_i. Poor performance was observed for cell 031203c (d_i=0.2 μm), whereas similar results were achieved for $d_i \geq 0.3$ μm.*

The spectral response as a function of d_i (Fig. 6.19) was analysed to gain additional information, especially to discern the role of optical and electrical properties. Two different regions were observed according to the dominant mechanism. Electrical properties seemed to control the performance at short wavelengths (λ < 550 nm), for which photons are effectively absorbed even when dealing with low d_i values. Therefore, lower quantum efficiencies in this region were achieved for cell 031204c (d_i = 0.4 μm). Conversely, devices seemed to be optically limited at long wavelengths, so higher current generation for λ > 550 nm was observed at increasing thicknesses due to enhanced absorption.

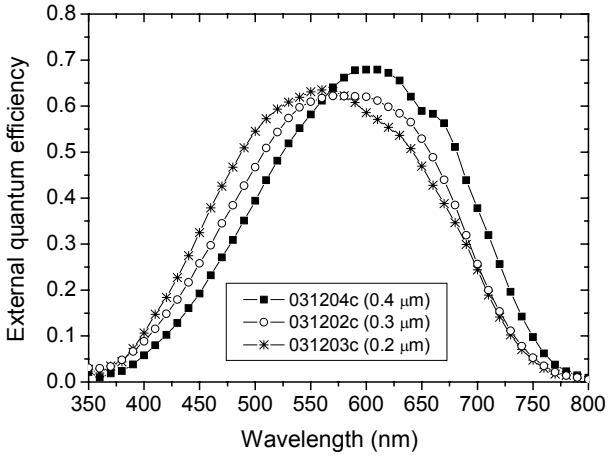

Figure 6.19. *Spectral response dependence on d_i for different cells exhibiting the same structure.*

In summary, and as far as our experimental results are concerned, improved performance was obtained with d_i = 0.4 μm (031204c), for which J_{sc} ~ 9.8 mA/cm^2, V_{oc} ~ 0.74 and FF ~ 0.63 were determined, leading to a conversion efficiency (η) around 4.5% (Fig. 6.18).

Additional insight into the photovoltaic performance of cell 031204c could be obtained by means of VIM results, which are presented in Fig. 6.20. Lower V_{oc} values than those observed in standard PECVD devices were achieved (Fig. 6.20(a)). As far as parasitic resistances are concerned, R_{sc} (Fig. 6.20(c)) at low illumination intensities evidenced the high value of R_p (~ 10^7 Ωcm^2), which can be also seen in the evolution of both V_{oc} and FF (Fig. 6.20(b)). On the other hand, R_{oc} (Fig. 6.20(d)) revealed the correct behaviour of the device at intermediate illuminations, where the measured curve was almost identical to the one observed in the PECVD device considered. Nevertheless, the influence of R_s was seen for $J_{sc} \geq 4$ mA/cm^2, this result pointing to some contact problems, most likely imputable to

unsuitable properties of the p-type layers (or corresponding interfaces) at the front contact. Accordingly, FF decreased dramatically for $J_{sc} \geq 4$ mA/cm^2. In particular, R_s between 4 - 5 Ωcm^2 was determined from the R_{oc} evolution after taking into account the slight saturation observed at high illumination intensities.

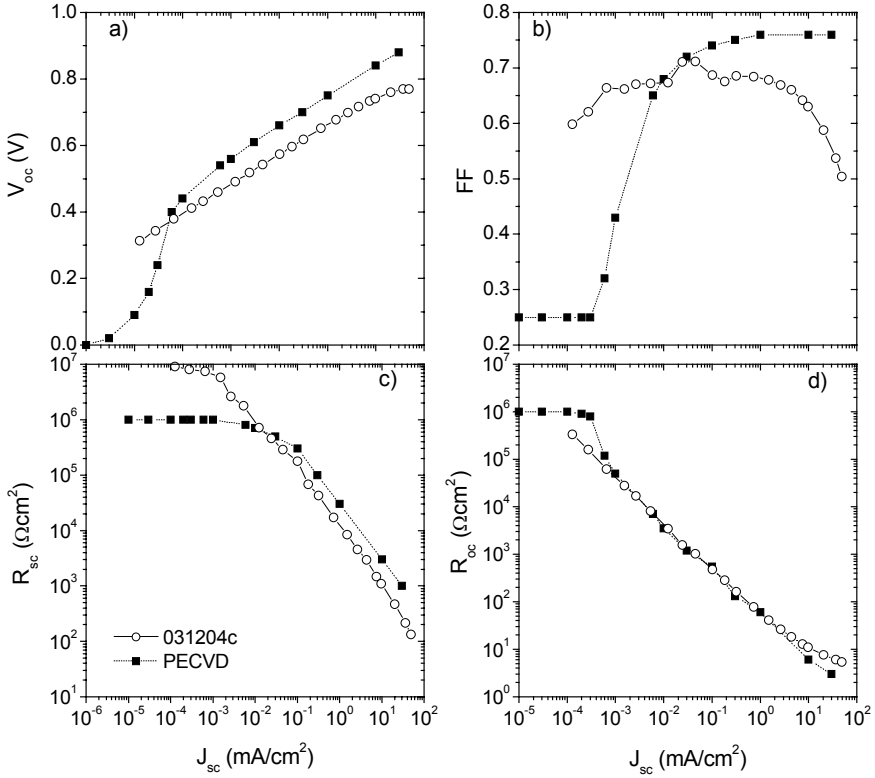

Figure 6.20. *VIM results for cell 031204c.*
Standard PECVD device data extracted from [Merten et al. 1998].

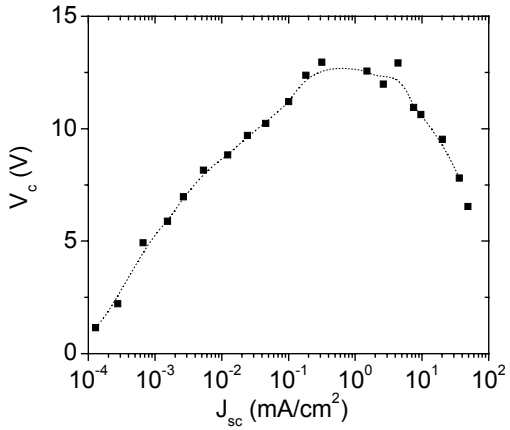

Figure 6.21. *Collection voltage as a function of the incoming light intensity for cell 031204c.*

Regarding the evolution of R_{sc} at intermediate illuminations, V_c values around 13 V were obtained (Fig. 6.21) although, unfortunately, the influence of the front contact seemed to limit its value, thus leading to lower V_c as J_{sc} was increased beyond 4 mA/cm^2.

Finally, and by following the same approach as in section 6.2, the effect of the parasitic resistances (R_s and R_p) on the device performance was filtered leading to the J'(V') curve presented in Fig. 6.22, for which FF of 0.66 and η of 4.8% were determined.

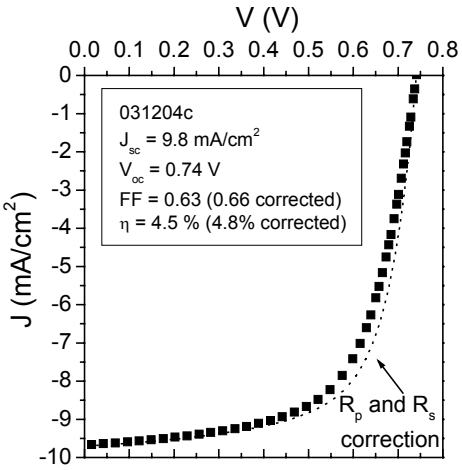

Figure 6.22. *J(V) curve for cell 031204c evidencing the importance of parasitic resistances, especially R_s in this case as R_p reached an acceptable large value.*

6.7. Device stability

Light induced degradation of a-Si:H (Staebler-Wronski effect) [Staebler and Wronski, 1977] constitutes one of the major obstacles in the development of a-Si:H based solar cells. Although much effort has been carried out during the last decades to solve this problem, light induced degradation is still an issue of great concern. Different studies have pointed to Hot-Wire CVD as a promising technique to enhance stability [Mahan et al. 1991, Bauer et al. 1998]. Nevertheless, even the best results for all Hot-Wire CVD devices reported to date give evidence of remarkable efficiency reduction (≥ 30%) after light soaking in both *n-i-p* [Wang et al. 2000] and *p-i-n* [Weber et al. 2000] structures. Special attention must be paid to the exciting work carried out at *Universiteit Utrecht* regarding protosilicon, which can be identified as a-Si:H exhibiting an enhanced degree of order [Schropp et al. 2004]. In

this case, *n-i-p* solar cells with degradation around 10% were reported, although only the intrinsic layer was deposited by Hot-Wire CVD [Van Veen 2003].

One of the most fundamental reasons limiting the results achieved is the lack of a satisfactory explanation for the Staebler-Wronski effect. Thus, whereas hydrogen has been widely accepted to play a key role in defect creation upon illumination, some questions are still unsolved. In particular, it remains unclear whether the most prominent role is played by the formation of defects in the bulk of the intrinsic layer or by the degradation of the p/i interface. In that sense, it has been shown that the nature of the degradation depends on the structure of the device (*p-i-n* or *n-i-p*) and on the light-soaking conditions. Thus, a worsening of the p/i interface has been observed for degradation experiments performed in short-circuit conditions, whereas enhancement of the defect density in the bulk of the material has been detected when evaluating the stability of the devices under open-circuit [Caputo 1999]. Taking into account that real operating conditions do not correspond to any of the mentioned conditions, a combination of both effects might be expected.

As far as our solar cells are concerned, very preliminary investigations were carried out, especially taking into account the still limited performance of our devices. Moreover, different results were found which need further investigation. Thus, shunting problems were observed, probably linked to mechanical stress after subsequent measurements. Additionally, solar cells exhibited certain irreversible changes that could not be recovered after annealing and which appeared even before submitting the devices to illumination. Similar results, which seemed to be attributable to the chemical stabilisation of surfaces and interfaces (boron diffusion from the p-type layer for instance), were observed in a-Si:H solar cells [Weber et al. 2000, Grunsky et al. 2004] and in our laboratory for nc-Si:H devices [Fonrodona 2003]. Despite these open questions, first results could be extracted from our measurements and are shown next.

Firstly, solar cell 031205c (section 6.2), which exhibited an initial efficiency around 4.3%, was degraded for 350 hours at one sun illumination and at similar conditions to the standard operation ones. The evolution of the different parameters can be seen in Fig. 6.23, where a typical degradation process can be observed. In particular, both J_{sc} and FF were clearly reduced after light-soaking, this result being commonly observed in *p-i-n* devices.

As a consequence, η was also reduced by more than 35%, this value being comparable to those reported.

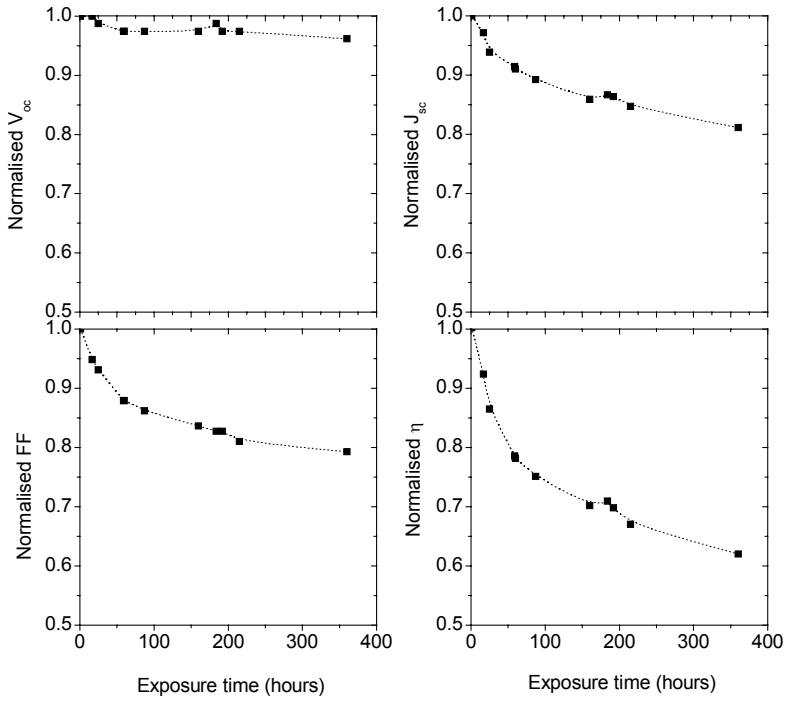

Figure 6.23. *Normalised parameters of device 031205c under light soaking.*

Additionally, solar cell 031204c, presented in section 6.5 (η ~ 4.5 %), was submitted to light soaking for 150 hours under open-circuit conditions. Figure 6.24 shows the VIM curves measured before and after illumination. VIM is a helpful tool to analyse the degradation of devices as, in particular, it allows to differentiate between technological (R_s, R_p) and physical aspects affecting the device performance [Merten et al. 1998]. As a first approach, Figures 6.24(a) and 6.24(b) clearly manifested a decrease of V_{oc} and, more evidently, of FF. On the other hand, R_{oc} (Fig. 6.24(d)) in the high illumination limit (related with R_s) did not show a dramatic difference between the initial and the degraded states, as only a subtle tendency to saturation could be observed in both cases. On the other hand, the lowest irradiance levels give us some insight into the possible existence of leakage currents. Thus, at such illumination conditions, R_p can be determined from the saturation of R_{sc} (Fig. 6.24(c)). In our case, only a slight decrease at the lowest illuminations could be observed in R_{sc} after prolonged illumination. Consequently, neither increased leakage currents nor degraded contact properties were observed after degradation

experiments. More valuable information could be extracted from the evolution of the different VIM curves at intermediate illuminations. In this regime, R_{sc} (Fig. 6.24(c)) was reduced by a factor of approximately 3 after degradation, whereas R_{oc} was slightly higher in the degraded state. In particular, and as already commented in previous sections, lower values of R_{sc} are indicative of poorer transport properties or, more directly, of increased defect density either in the bulk of the active layer or in the region close to the p/i interface. Regarding V_c, extracted from the R_{sc} evolution and directly linked to the transport properties of the active layer as previously shown, it was reduced from around 12 V to 4 V after light-soaking, this result manifesting the worsening of the material properties. Finally, the reduction of V_{oc} over all the illumination range could be linked to increased recombination at both interfaces (p/i and i/n) [Merten et al. 1998].

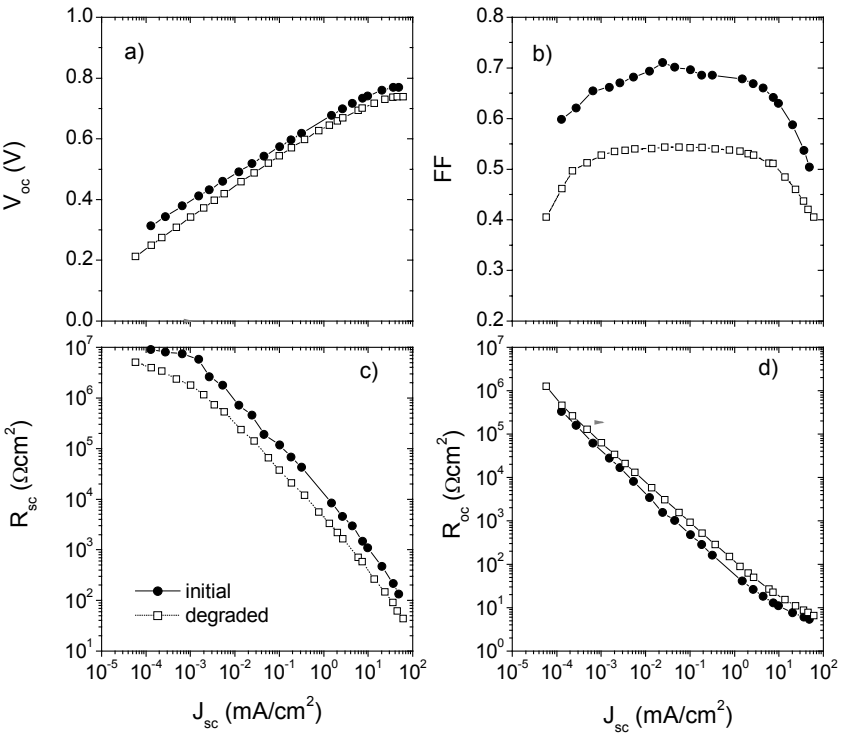

Figure 6.24. *Evolution of V_{oc}, FF, R_{sc} and R_{oc} for cell 031204c after 150 hours of 100 mW/cm^2 illumination.*

Summarizing, preliminary results presented for both 031205c and 031204c devices showed that the light induced degradation of our solar cells was mainly provoked by the degradation of the physical properties of the intrinsic layer and the p/i interface. A similar degradation to that typically observed was obtained, although further studies, especially

aiming to understand the initial irreversible degradation, are required to evaluate the stability of our devices.

6.8. Summary

Results shown in the previous chapters were used to obtain our first completely Hot-Wire CVD deposited a-Si:H based solar cells. Furthermore, low substrate temperature was used to allow the future utilization of low cost substrates ($T_s \leq 200$ºC). These preliminary results concerned the analysis of several structures involving different front and back contact strategies. In particular, different p-type layers (a-Si:H, nc-Si:H or double structures) and TCO (bare or ZnO:Al coated Asahi-U) were tested in the front contact, whereas the implementation of a back reflector was analysed for the back one.

Our best results were achieved either in entirely a-Si:H front contacts deposited on bare Asahi-U, or in solar cells having a p-type double layer (nc-Si:H/a-Si:H) grown on coated Asahi-U, for which initial efficiencies around 4.3 and 4.5%, respectively, were measured. Nevertheless, different observations gave evidence of the still limited performance of our devices, resulting especially in low J_{sc}.

The use of low T_s led to intrinsic a-Si:H with dangling bond densities around 5×10^{16} cm^{-3}, which might well have affected the behaviour of the solar cell as observed in the limited V_c values. Anyway, the response of our devices at long wavelengths attested the acceptable performance of both the active layer and the back contact, where a back reflector effectively improved the photovoltaic operation. Consequently, it was the front contact which seemed to mainly limit the achievable J_{sc}, which lay around 10 mA/cm^2 in the most favourable cases. Moreover, spectral response measurements clearly evidenced poor operation at short wavelengths, pointing to difficulties at the front contact and/or at the p/i interface. Different effects have been identified as especially critical and possibly responsible for such performance:

1) TCO: The use of bare Asahi-U was limited to completely a-Si:H devices, in which low TCO reduction is expected due to the low H concentration involved in the growth process. Conversely, ZnO:Al coated Asahi-U had to be used when front contacts

involving nc-Si:H layers were considered. Unfortunately, the use of bare Asahi-U was seen to lower J_{sc}, whereas ZnO:Al coated Asahi-U led to worse contact properties and, consequently, low FF.

2) TCO/p interface: The interface between the TCO and the p-type layer plays a key role when evaluating the device performance. In particular, results shown in *Chapter 5* gave evidence of a significant voltage drop at this interface.

3) p-type layer: Several problems arose from our difficulty to effectively dope p-type a-Si:H. On one hand, the low doping efficiency required the deposition of very thick layers ($d_p \sim 40$ nm) or double structures (combining both a-Si:H and nc-Si:H) with total thicknesses around 60 nm to ensure the correct diode behaviour. Unfortunately, such thick layers might have led to dramatic optical losses. On the other hand, the use of higher doping ratios, which were seen to improve the electrical properties of our p-type layers, led also to poor performance, most likely attributable to technological problems such as cross-contamination and/or boron diffusion.

4) p/i interface: Different mechanisms degrade the properties of the p/i interface, such as boron diffusion or dangling bond density. These phenomena result in enhanced recombination and changes of the E_i distribution over the intrinsic layer, thus leading to a deleterious effect on the response of the cell, especially at short wavelengths.

Finally, and although only very preliminary studies were carried out, the degradation of our solar cells after light exposure seemed to be mainly provoked by the worsening of the electrical properties of both the active layer and the p/i interface as expected. Nevertheless, a certain degradation, which could not be recovered after annealing, was observed even without submitting the devices to illumination. In this case, chemical stabilisation of surfaces and interfaces seemed to account for the behaviour observed.

7. Solar cell simulation

In this chapter, simulation results bringing some additional light into the device physics will be presented. Furthermore, simulations will be compared with experimental results presented in *Chapter 6*, where the behaviour of our Hot-Wire CVD devices was presented. In particular, special attention will be paid to the influence of the front contact and to the role of localized states, caused by dangling bonds and contaminants in the band gap.

7.1. p-i-n solar cell operation

In order to better understand simulation results, a brief overview on the operation of *p-i-n* solar cells is given next. The photovoltaic energy conversion requires the separation and collection of carriers generated by incoming photons. Hydrogenated amorphous silicon (a-Si:H) is a low mobility semiconductor ($\mu \sim 1\ cm^2V^{-1}s^{-1}$), especially when compared with crystalline silicon (c-Si), whose μ values are around 1000 times higher. Consequently, a-Si:H based devices can not be implemented with simple *p-n* junctions as when dealing with c-Si, in which the low recombination allows the diffusion of carriers. In contrast, *p-i-n* structures are employed, where an electric field (E_i) extends over the intrinsic layer allowing the separation of carriers, thus resulting in drift controlled solar cells. E_i is created by the doped layers at both ends of the intrinsic material, leading to a voltage drop in the active layer that, in equilibrium conditions, is known as *built-in* voltage (V_{bi}), and whose value is determined by the position of the Fermi level of the doped layers.

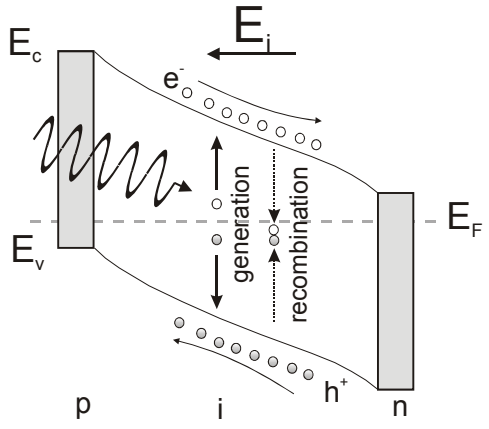

Figure 7.1. *Schematic band-diagram and photocarrier collection in an a-Si:H p-i-n solar cell.*

The basic operation of a *p-i-n* device can be seen in Figure 7.1. The illumination of the device creates electron-hole pairs, which are separated by E_i, so that holes and electrons are drifted towards the p- and the n-type layer respectively. Unfortunately, photogenerated pairs have a significant probability to recombine before reaching the doped layers due to the limited transport properties of a-Si:H. In particular, active layers exhibiting large dangling bond density are expected to present very high recombination rate and, consequently, poor carrier collection (and photovoltaic performance). Moreover, the E_i distribution over the intrinsic layer must be carefully analysed, as its profile drastically affects the carrier collection. In particular, the E_i distribution over the active layer is affected by different aspects such as the i-layer thickness or the local space charge due to dangling bonds, band-tail states and donor or acceptor centres caused by contaminants. As an example, increased E_i is required in highly defective material, thus compensating for its increased recombination rate. In that sense, thin devices with intense electric field exhibit better performance after prolonged light exposure than thick ones, for which the increased density of dangling bonds due to the Staebler-Wronski effect induces an elevated recombination rate. On the other hand, low E_i can lead to suitable operation when dealing with very low defect densities, thus allowing the use of thicker intrinsic layers favouring the absorption of incoming photons and, consequently, the photogeneration of carriers.

On the other hand, a-Si:H doped layers are highly defective and only carriers generated in the active layer do significantly contribute to the photogenerated current. Accordingly, low optical absorption in the doped layers is expected to lower optical losses, this effect being especially critical for the p-type layer at the front contact.

The behaviour of amorphous silicon solar cells can be numerically analysed by taking into account a series of equations that deal with carrier transport. First of all, the Poisson's equation must be considered

$$\frac{dE}{dx} = \frac{q}{\varepsilon}\left[(p-n) + Q(p,n)\right] \tag{7.1}$$

where E is the electric field, which is related by this equation to the local charge due to free carriers (n are p) and to trapped charge, Q.

On the other hand, the current density equations combining both drift and diffusion mechanisms must be evaluated

$$j_p(x) = q\mu_p p(x)E(x) - kT\mu_p \frac{dp(x)}{dx} \tag{7.2a}$$

$$j_n(x) = q\mu_n n(x)E(x) + kT\mu_n \frac{dn(x)}{dx} \tag{7.2b}$$

where j_p and j_n correspond to the hole and electron currents respectively. Besides, the two continuity equations considering the generation (G) and the recombination (R) rate, whose evaluation details can be found in [Asensi et al. 1999], are also necessary

$$\frac{dj_p(x)}{dx} = q\left[G - R(p,n)\right] \tag{7.3a}$$

$$\frac{dj_n(x)}{dx} = -q\left[G - R(p,n)\right] \tag{7.3b}$$

The presented set of equations defines a system of coupled equations that can be numerically treated to simulate the operation of solar cells. Nevertheless, a detailed description of the device would be too complicated, so different simplifications must be considered. In particular, the following assumptions were taken in our study:

a) The doped layers are not considered when solving the transport equations, and only boundary conditions are defined at the p/i and i/n interfaces.

b) Only dangling bonds are considered when determining the trapped charge (Q), whereas no influence of the localized states at the band tails is taken into account. Thus, the next expression for Q is proposed

$$Q = \left(f^+(p,n) - f^-(p,n)\right)N_{DB} \tag{7.4}$$

where N_{DB} is the density of dangling bonds and f^+ and f^- are the occupation of positive and negative dangling-bond states [Asensi et al. 1999], which depend on the capture cross-sections of both electron and holes at neutral, positive or negative

dangling bonds, and on the effective densities of states.

c) A uniform and constant distribution of defects over the intrinsic layer is considered.

Furthermore, several boundary conditions must be considered to solve the above-presented set of equations. These conditions are mainly linked to the doped layers at both ends of the solar cell and are listed next:

a) The voltage drop over the intrinsic layer is given by the difference between the *built-in* and the externally applied voltages

$$V(L) - V(0) = V_{bi} - V_{appl} \tag{7.5}$$

where L is the thickness of the intrinsic layer and V_{appl} is the applied voltage.

b) The interfaces behave as perfectly ohmic contacts for majority carriers, so that very high recombination values (S) at the electrodes are supposed. As a result, the concentration of majority carriers can be considered as independent of the current density and equal to those values in equilibrium

$$p(0) = p_{eq}(0) \tag{7.6a}$$

$$n(L) = n_{eq}(L) \tag{7.6b}$$

c) Regarding minority carriers, the opposite behaviour is expected, as highly blocking contacts are defined. In particular, the current of minority carriers at the contacts is given by

$$j_p(L) = qS_L\left(p(L) - p_{eq}(L)\right) \tag{7.7a}$$

$$j_n(0) = qS_0\left(n(0) - n_{eq}(0)\right) \tag{7.7b}$$

where very low S_L and S_0 values are chosen (perfectly blocking contacts would be represented by S_L=S_0=0 cm/s).

From the above presented set of equations and boundary conditions, it is clear that a large number of parameters are involved in numerical calculations. In particular, those values employed in our simulations are presented in Table 7.1.

Parameter	***Value***
Intrinsic Material	
Band gap E_g (eV)	1.70
Effective densities of states (N_c and N_v) cm^{-3}	2.5×10^{19}
Electron mobility μ_n ($cm^2/V/s$)	10
Hole mobility μ_p ($cm^2/V/s$)	10
Dangling bond density N_{DB} (cm^{-3})	10^{15} - 10^{18}
Energy level of the $D^+ \leftrightarrow D^0$ transition E^+-E_v (eV)	0.7
Effective correlation energy U_{eff} (eV)	0.3
Thickness (μm)	0.2 – 0.4
Capture cross-section by dangling bonds	
Capture cross-section of electrons by D^0 σ_n^0 (cm^2)	5×10^{-16}
Capture cross-section of electrons by D^+ σ_n^+ (cm^2)	2.5×10^{-14}
Capture cross-section of holes by D^0 σ_p^0 (cm^2)	1×10^{-16}
Capture cross-section of holes by D^- σ_p^- (cm^2)	5×10^{-15}
Capture times of free carriers by dangling bonds	
Capture time of electrons by D^0 τ_n^0 (s)	2×10^{-8}
Capture time of electrons by D^+ τ_n^+ (s)	4×10^{-10}
Capture time of holes by D^0 τ_p^0 (s)	10^{-7}
Capture time of holes by D^- τ_p^- (s)	2×10^{-9}
Doped material	
Dangling bond density N_{DB} (cm^{-3})	10^{18}
Interface recombination velocity of minority carriers S_L and S_0 cm/s)	10
p-type	
Impurity level E_A (eV)	0.2
Impurity density (cm^{-3})	10^{18}
n-type	
Impurity level E_D (eV)	1.5
Impurity density (cm^{-3})	10^{18}

Table 7.1. *Values of parameters used for numerical simulation.*

7.2. Numerical analysis

Results presented in *Chapter 6* manifested the limitations of our solar cells. In particular, very low external quantum efficiencies at short wavelengths leading to abnormally low J_{sc} were observed. Optical losses at the front contact and/or degraded electrical properties at the p/i interface leading to enhanced recombination might have been responsible for such behaviour. In order to deeply analyse those experimental results, a computer program that uses finite differences and the Newton technique to numerically solve the set of coupled equations [Asensi 1994] was used. Nevertheless, not only numerical resolution of the equations presented in the previous section was carried out, but also the *DICE* (dynamic inner collection efficiency) technique was used as a first approach to analyse the obtained results. Furthermore, the simulated photovoltaic structure in all cases was that leading to our best devices (*Chapter 6*), that is, *p-i-n* structure with both p- and n-type double layers

TCO /p(nc-Si:H)-p(a-Si:H)/i(a-Si:H)/n(a-Si:H)-n(nc-Si:H)/metal

where 50, 10, 10 and 70 nm were the thicknesses of the p(nc-Si:H), p(a-Si:H), n(a-Si:H) and n(nc-Si:H) layers respectively. Unfortunately, neither the front contact roughness nor the incorporation of the back reflector were taken into account in the present program, so only a qualitative approach could be carried out.

7.2.1. Optical absorption

Although the set of coupled equations was only solved for the intrinsic layer (boundary conditions were considered at the interfaces), the simulation of solar cells requires an accurate determination of the optical constants (especially the absorption coefficient, α) of the different materials. In particular, the absorption of p-type a-Si:H and nc-Si:H plays a key role, as pairs generated in any of these layers do not contribute to the collected current. In addition, the absorption spectrum of intrinsic a-Si:H is also necessary to describe the generation profile into the active layer.

Firstly, the optical constants of a-Si:H, which depend on the preparation method and on the deposition conditions, were analysed. The optical parameters of a-Si:H can vary over a

wide range, differently from c-Si, whose optical properties are defined by a unique set of parameters. In our case, optical constants were determined following the analytical model proposed by [Forouhi and Bloomer 1986]. The analytically calculated absorption spectrum was fitted to experimental data (a-Si:H samples grown at similar conditions to those of the active layer in our solar cells were used). Figure 7.2 shows the calculated results, from which a remarkably satisfactory fit at intermediate wavelengths can be observed. Conversely, enhanced absorption at low energies is experimentally observed, this fact pointing out the contribution of localized states in the band gap.

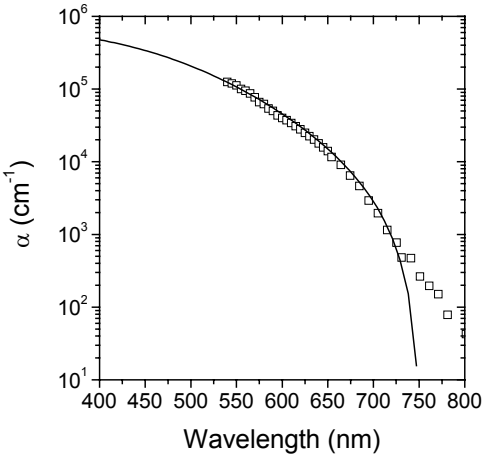

Figure 7.2. *a-Si:H absorption spectrum simulation. The solid line corresponds to the analytical solution, which remarkably fits experimental data.*

Regarding nc-Si:H, a two-phase material consisting of crystallites and a-Si:H was considered. Similarly to the treatment presented in section 3.2, where the electrical conductivity of nc-Si:H samples was analysed, the Bruggeman's effective medium approximation (EMA) was used. The resulting effective dielectric function ($\varepsilon^{eff} = \varepsilon' - i\varepsilon''$), from which the rest of parameters could be extracted, is given by equation 7.8 [Niklasson and Granqvist 1983, Stroud 1998]

$$f\frac{\varepsilon_c - \varepsilon^{eff}}{\varepsilon_c + 2\varepsilon^{eff}} + (1-f)\frac{\varepsilon_a - \varepsilon^{eff}}{\varepsilon_a + 2\varepsilon^{eff}} = 0 \qquad (7.8)$$

where ε_c and ε_a correspond to the complex dielectric functions of the crystalline and amorphous phase respectively and f refers to the crystalline volume fraction. The complex

effective refraction index ($n^{eff} = n - ik$) could be determined from ε^{eff} ($n^{eff} = \sqrt{\varepsilon^{eff}}$), thus allowing the determination of the extinction coefficient (k) and, finally, the evaluation of α ($\alpha = 2\omega k/c$, with ω being the angular frequency and c, the speed of light). Figure 7.3 shows different simulated absorption spectra obtained at different f values.

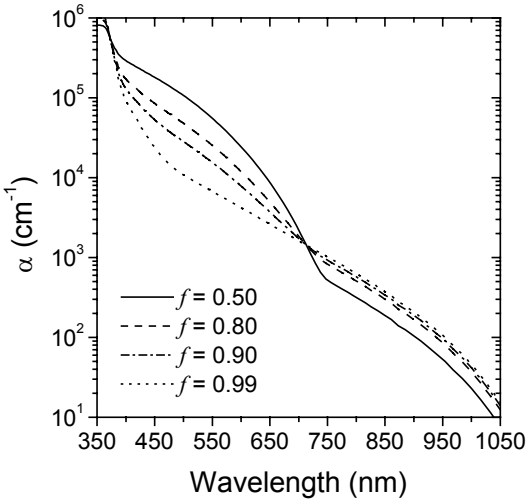

Figure 7.3. *Theoretically obtained absorption spectra for thin silicon films exhibiting varying crystalline volume fractions.*

A clear transition from typical a-Si:H to nc-Si:H absorption spectra was observed at increasing crystalline fractions. In particular, and as far as our simulations are concerned, a f value around 0.8 was considered. Nevertheless, it is important to remark that, despite its correlation, f and X_c can not be straightforwardly compared. In our case, f was chosen after suitably fitting the experimental data of p-type nc-Si:H layers deposited at similar conditions to those employed in solar cells.

7.2.2. DICE technique

DICE (dynamic inner collection efficiency) analysis is based on the division of the solar cell into different slices, each one given a certain thickness, absorption spectrum, and collection efficiency (CE) [Takahama et al. 1986, Fischer 1994, Nubile et al. 1998]. Consequently, *DICE* analysis permits the evaluation of J_{sc} (or the spectral response) by separately taking into account the contribution of each region of the device. In our case, *DICE* was used only as a first approach to enlighten the performance of our solar cells.

First results were obtained by considering a very simplified 5-layer model (double p-type layer, intrinsic a-Si:H and double n-type layer). Null CE was supposed for the doped layers due to their high recombination rate leading to poor transport properties, whereas optimum collection efficiency (CE = 1) was used for the intrinsic material (Fig. 7.4). Moreover, the effect of the active layer thickness was analysed (d_i = 0.2, 0.3 and 0.4 μm) to allow comparison with experimental results (section 6.6), leading to a better understanding of the device physics.

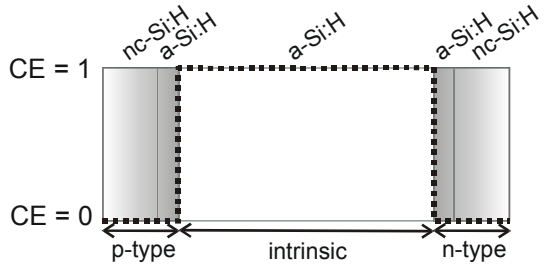

Figure 7.4. *DICE profile considering optimum collection (CE = 1) within the intrinsic layer.*

Simulation results are presented in Fig. 7.5(a), where the simulated absorbance profile, which limits the theoretically optimum external quantum efficiency, is also shown. The spectral response would be identical to the presented optical absorbance if CE = 1 could be considered over the whole structure. In addition, experimental curves are also plotted for comparison in Fig. 7.5(b).

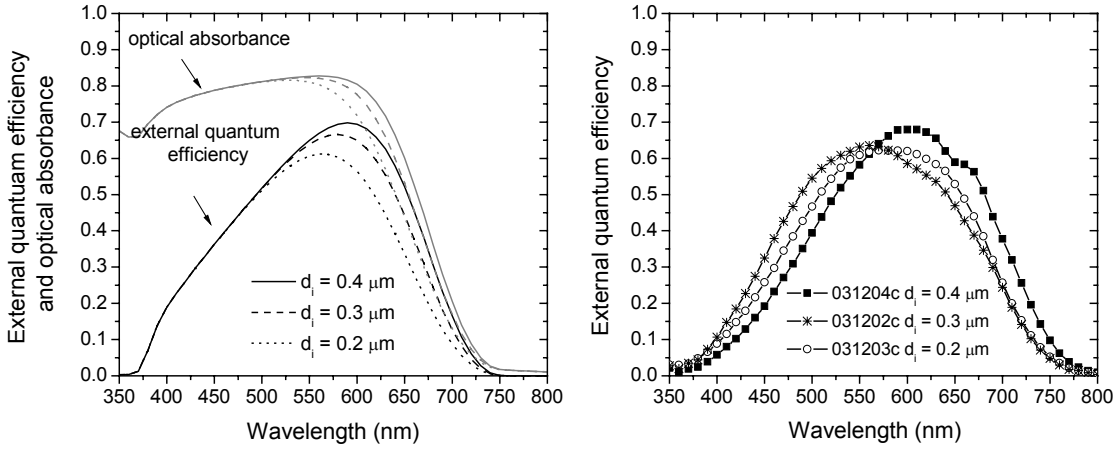

a) *b)*

Figure 7.5. *Spectral response and optical absorbance as simulated by DICE analysis (a) and experimentally obtained spectral response (b) as a function of d_i.*

Both simulated and experimental results gave evidence of remarkably low spectral response at high energies (λ between 350 and 450 nm). As ideal collection efficiency (CE = 1) was considered for the active layer in *DICE* simulations, this result might have been imputable to important optical losses at the p-type double layer, whose poor transport properties (CE = 0) hindered carrier collection. Furthermore, the use of textured substrates in our devices resulted in even higher absorption and, consequently, this effect might have been further enhanced in our experimentally obtained solar cells. On the other hand, both simulated and experimental data pointed out improved collection efficiency at low energies (λ > 550 nm) for increasing d_i, this result being related to enhanced optical absorption for thicker devices.

An experimentally obtained feature, not reproduced in our simulations, should be highlighted. Thus, poorer external quantum efficiencies in the short wavelength range were measured for the thickest sample and vice versa, this trend being opposed to the one observed at long wavelengths. Therefore, an intersection point around 550 nm was observed in Fig. 7.5(b). This result gave evidence of the non-ideal properties of the material (dangling bonds, contaminants), which result in worse collection properties at increasing d_i due to different reasons. On one hand, the mean distance the carriers have to cover before being collected is increased when higher d_i values are considered, thus enhancing the recombination probability and, obviously, degrading the device performance. Additionally, high d_i leads to low E_i, resulting in less efficient spatial separation of the pairs created and to lower velocity of the carriers, both effects leading again to increased recombination probability, especially when dealing with active layers with significant defect density. It is worth taking into account that these effects are present over the whole wavelength range, but the enhanced optical absorption at low energies might compensate for them, resulting in even higher quantum efficiencies at higher d_i as already commented.

As a first approach to qualitatively simulate the real properties of the active layer, constant CE over the whole active layer with lower values for increasing d_i was considered, so that the enhanced recombination at higher d_i values could be taken into account. In particular, CE = 1, 0.9 and 0.8 were chosen for d_i = 0.2, 0.3 and 0.4 μm respectively. On the other hand, a 6-layer *DICE* profile was also analysed, for which the intrinsic layer was divided

into two different slices. The first slice exhibited CE = 1 as in the ideal case, while CE = 0 was assigned to the second one ("death zone"), which was situated in the region close to the p/i interface. In this case, the different properties of the intrinsic layer were simulated by properly tuning the thickness of the death region (d_{death}), so that d_{death} = 5, 10 and 15 nm was selected for d_i = 0.2, 0.3 and 0.4 μm, respectively. Simulated results and the corresponding *DICE* profiles are presented in Figure 7.6, which led to a qualitatively similar trend to that experimentally observed.

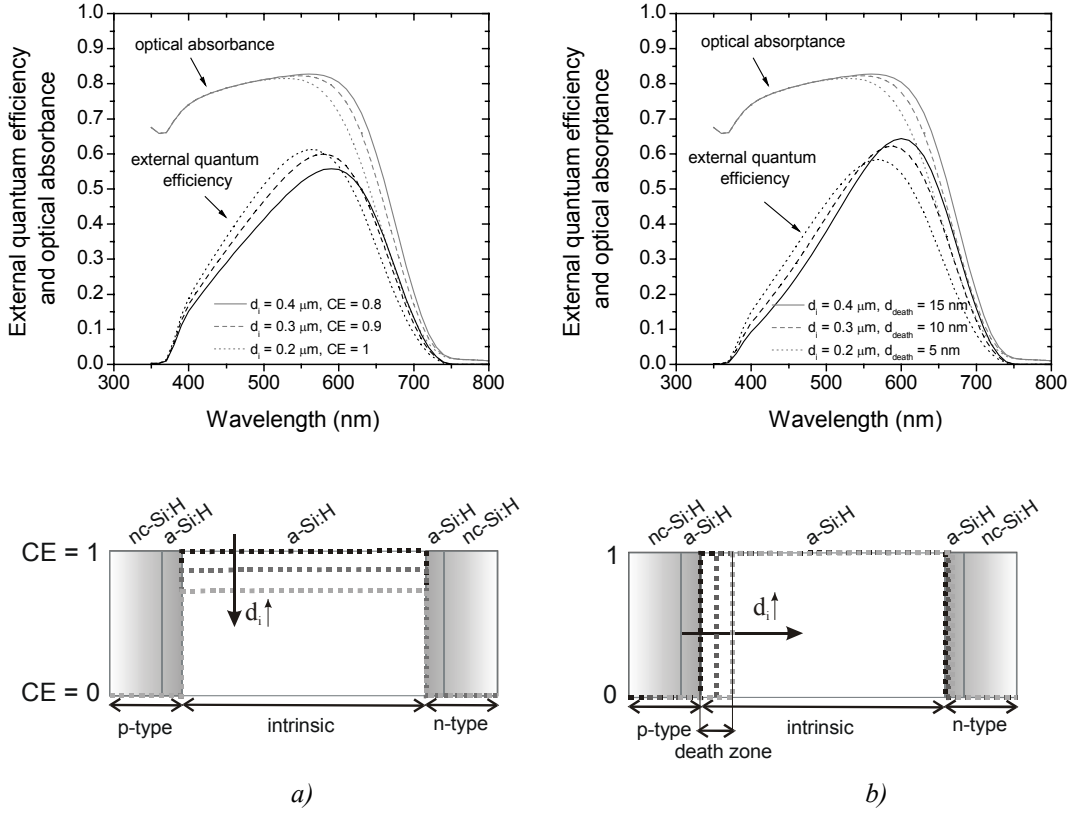

Figure 7.6. *Spectral response as simulated by DICE analysis after considering the effect of d_i on the collection properties. A 5-layer model exhibiting decreasing CE at increasing d_i (a) and a 6-layer model including a death zone with increasing thickness at higher d_i (b) were considered.*

As expected, increased optical absorption led to higher quantum efficiencies in the long wavelength region as d_i was increased, whereas electrical properties limited the response of the device at short wavelengths, so that poorer operation was achieved for the thickest solar cell. Nevertheless, if simulated results are carefully compared with experimental ones (Fig. 7.5(b)), the inhomogeneous treatment involving a death zone seemed to allow a better

fit. Therefore, the observed result seemed to be mainly associated to poor properties at the p/i interface. It is known that increased defect density near the p/i interface strongly degrades the device operation [Herbst et al. 1995]. In particular, simulation results [Bauer et al. 1996] manifested that a twofold increase in the defect density at the p/i interface resulted in a reduction of the solar cell efficiency comparable to that observed when the bulk defect density was increased by two orders of magnitude. Moreover, the same study indicated that comparable efficiencies could be obtained as long as similar properties were kept at the p/i interface. Besides, the bulk material density of defects was shown to play a relatively minor role as long as it was kept below a certain limit.

In summary, and as far as the *DICE* technique is concerned, the following conclusions could be extracted:

1) Experimentally observed poor response at short wavelengths might be mainly attributed to the dramatic absorption of photons at the p-type double structure.

2) The higher collection at long wavelengths for increasing d_i values was imputable to enhanced optical absorption.

3) The trend observed at high energies (opposed to that described at low ones) was reproduced after considering degraded transport properties at increasing d_i.

4) A so-called "death zone" near the p/i interface, where any carrier collection was forbidden, seemed to lead to the best fit of our experimental results.

In the following section, experimental and *DICE* results will be taken into account and different approaches involving varying N_{DB} densities and the incorporation of impurities in the active layer will be numerically simulated.

7.2.3. Numerical resolution of the equations

Numerical simulation of *p-i-n* devices is based on the simultaneous resolution of the Poisson and continuity equations for holes and electrons [Asensi 1994]. In our case, two

different approaches were followed to simulate our solar cells in agreement with experimental and *DICE* simulation results. On one hand, spectral responses were calculated for different N_{DB} values in the intrinsic layer, whereas, on the other hand, the incorporation of acceptor contaminants was taken into account. Both approximations lead to degraded properties at the p/i interface, which might, at least partially, reproduce those results experimentally observed. Besides, all simulations were performed with similar generation rates (G) to those employed in the experimental spectral response measurements, for which no bias-light was employed.

- *Dangling bonds*

N_{DB} is expected to affect the carrier transport through different mechanisms. On one hand, the recombination rate is obviously enhanced when the density of dangling bonds is increased, as they act as recombination centres which worsen the transport properties of the material. Additionally, the internal electric field is also affected by N_{DB}, so the separation and collection of photogenerated carriers results also affected. In order to analyse this second mechanism, both the simulated electric field profile and the band diagram for different N_{DB} values are presented in Figure 7.7.

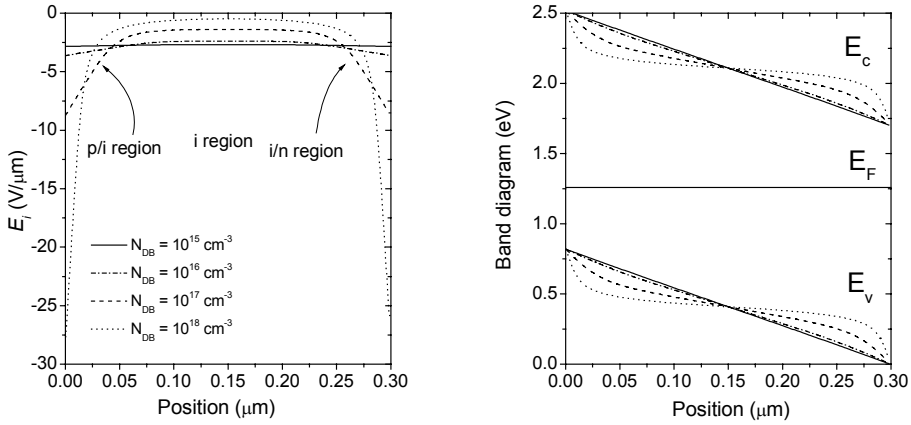

a) *b)*

Figure 7.7. *Simulated electric field profile (a) and band diagram (b) for different N_{DB} values giving evidence of the dramatic influence of dangling bonds on the photovoltaic performance.*

The presence of dangling bonds in the active layer leads to an increase of the trapped charge density at the p/i and i/n interfaces due to Fermi level shifts [Asensi et al. 1999].

Dangling bonds are positively ionized in the region close to the p-type layer, whereas a negatively charged region emerges in the vicinity of the n-type one, where dangling bonds are negatively ionized. The distribution of trapped charge in the intrinsic material leads to the appearance of a weak field region in the bulk of the intrinsic layer, whereas intense E_i is obtained in the regions close to the interfaces (Fig. 7.7(a)). In fact, an almost field free region in the bulk of the intrinsic layer would be obtained for large enough N_{DB}. The collection of photogenerated pairs is then hindered at increasing defect density, not only due to the obvious increase of the recombination probability at increasing recombination centres, but also due to the weak E_i in the bulk of the intrinsic layer not being capable of effectively separate them. From curves presented in Fig. 7.7, it can be deduced that $N_{DB} \leq 10^{16} cm^{-3}$ is expected to lead to acceptable electron-hole separation, as E_i remains high enough over the entire intrinsic layer. On the contrary, N_{DB} values above 10^{17} cm^{-3} clearly limit the solar cell behaviour, as E_i becomes very intense near the interfaces whereas it is clearly debilitated in the bulk of the i-layer. Regarding the energy band diagram, the trapped charge is seen to provoke the bending of the bands at both the p- and the n-type interfaces (Fig. 7.7(b)). It is worth noting that d_i of 0.3 μm was chosen for the presented simulations, this being a typical value for our deposited devices.

In order to allow comparison with experimental results, the simulated spectral responses for different N_{DB} and d_i values are presented in Fig. 7.8, where a dramatic dependence on the dangling bonds density can be easily observed, in agreement with above-mentioned mechanisms. Optical properties determined the overall behaviour when intrinsic layers exhibiting very low N_{DB} values (10^{15} cm^{-3}) were considered. Hence, Fig. 7.8(a) shows increased collection efficiency in the long wavelength region for that cell exhibiting $d_i = 0.4$ μm, whereas no influence is observed in the short wavelength range. In this case, the transport properties were satisfactory enough to allow the collection of photogenerated carriers in all studied cases, regardless the increased collection path at high d_i and its lower E_i. This observation is linked to previously mentioned results. Thus, in this case the density of recombination centres was low and E_i was high enough in all cases (even for the thickest device) to effectively separate the electron-hole pairs, both effects leading to low R values. On the other hand, the opposite trend was observed for $N_{DB} = 10^{18}$ cm^{-3} (Fig. 7.8(d)). In this case, the operation was controlled by the electrical properties, so that poorer performance over the entire range was obtained as d_i increased. In this case, very

significant recombination was obtained due to the very high N_{DB} considered. Moreover, E_i in the bulk region was significantly debilitated by the high N_{DB} value (Fig. 7.7(a)), resulting in a clearer dependence on d_i.

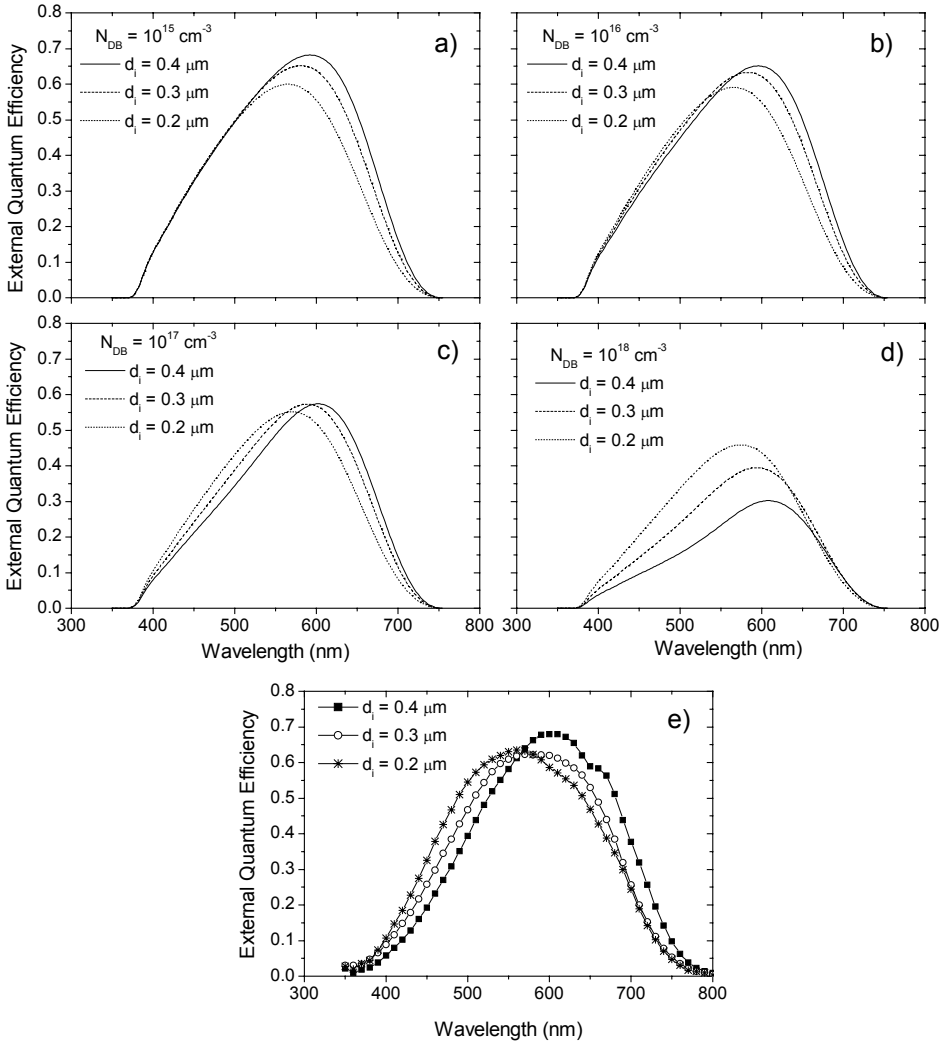

Figure 7.8. *Numerical simulation of the spectral response for solar cells exhibiting active layers with different thicknesses and N_{DB} values: 10^{15} cm^{-3} (a), 10^{16} cm^{-3} (b), 10^{17} cm^{-3} (c) and 10^{18} cm^{-3} (d). Experimental results are also presented for comparison (e).*

Finally, the most interesting (and realistic) case occurred when intermediate N_{DB} values were studied. In this situation, a similar result (especially for N_{DB} = 10^{17} cm^{-3}) to that experimentally observed was obtained. Optical enhancement seemed to determine the behaviour at long wavelengths, as increased absorption compensated for the poor electrical

properties observed at large d_i. On the other hand, electrical properties seemed to account for the cell performance at short wavelengths, for which increased d_i led to higher recombination probability due to the larger collection path and to the reduced electric field. In order to deeply analyse the behaviour observed at $N_{DB} = 10^{17}$ cm^{-3}, the one that more accurately fitted our experimental results, the internal electric field (Fig. 7.9) and both the generation (G) and the recombination (R) rates at λ = 450 and 700 nm were simulated (Fig. 7.10). Exceptionally, the doped layers were considered in the simulations of both G and R to attest the important recombination at these layers. As seen in Figure 7.9, clearly weakened E_i leading to degraded electrical properties was observed at increasing d_i

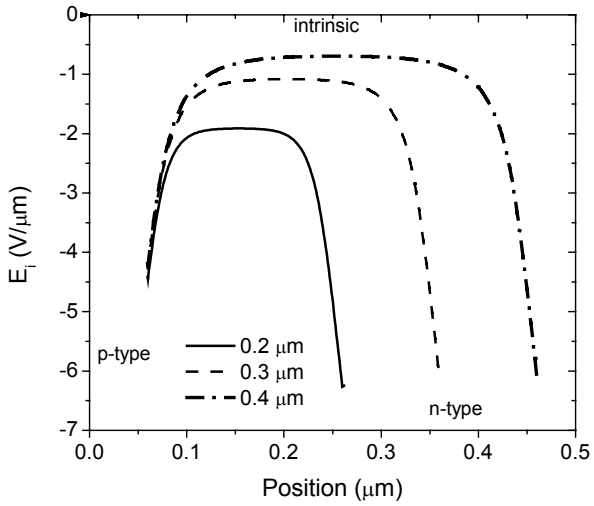

Figure 7.9. *Electric field profile as a function of d_i for $N_{DB} = 10^{17}$ cm^{-3}.*

Additionally, R for both wavelengths clearly increased as d_i was varied from 0.2 to 0.4 μm, thus giving evidence of increased recombination probability. In particular, very significant recombination was observed at the p/i (both wavelengths) and at the i/n (λ = 700 nm) interfaces, this result being a consequence of the charged defect states at these regions. Thus, dangling bonds are positively ionized in the region close to the p/i interfaces, so that electrons are very likely to be captured. A similar behaviour is observed at the i/n interface, whereas lower R values are achieved in the bulk of the active layer due to the neutrality of the defects in this zone. Regarding G, a remarkably different behaviour was observed at λ = 450 and 700 nm. Hence, most of the radiation with λ = 450 nm was absorbed within the first 0.2 – 0.3 μm, so that very similar absorption over the whole device was obtained

for the three d_i values analysed. Consequently, the increased recombination at the highest d_i determined its worse overall performance. On the contrary, an almost uniform absorption along the active layer was observed at low energy (λ = 700 nm), this fact leading to remarkably enhanced absorption (and, consequently, enhanced electron-hole pair generation) at larger d_i values and, eventually, to improved solar cell performance compensating for the higher recombination.

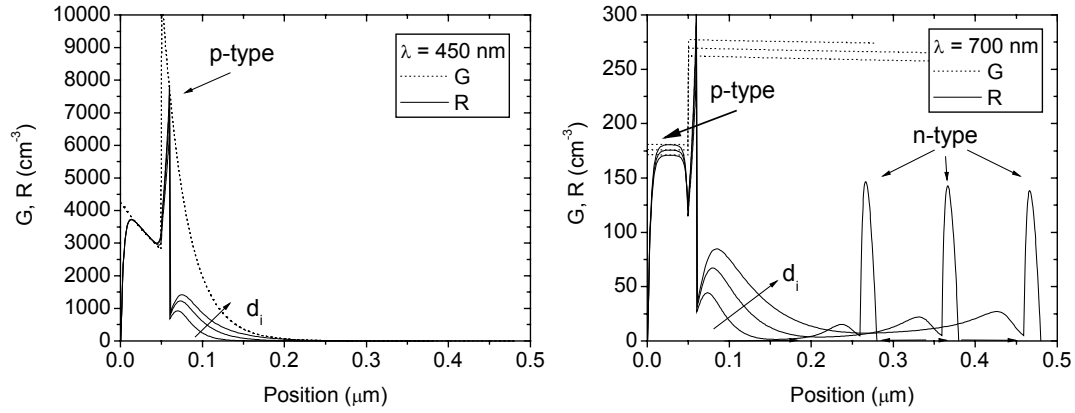

a) *b)*

Figure 7.10. *G and R at λ = 450 nm (a) and λ = 700 nm (b).*
High R is obtained in the doped layers due to their high defect concentration.

- *Contaminants*

The incorporation of contaminants into the active layer degrades the performance of photovoltaic devices due to the non-intrinsic character of the resulting material. Different contamination sources can exist, such as oxygen incorporation (n-type) or boron diffusion from the already deposited p-layer (p-type) [Matsui et al. 2003]. In particular, chemical stabilization of the p-type material and its influence on the corresponding junctions exhibits a dramatic role on the performance of the devices [Grunsky et al. 2004]. Contaminants can be simulated as a shallow distribution of either acceptor or donor states. Figure 7.11, where $N_{DB} = 10^{16}$ cm^{-3} and two different acceptor densities (N_A) of 10^{16} and 5×10^{15} cm^{-3} were considered, shows the influence of acceptor contaminants on E_i. Additionally, the electric field profile of a non-contaminated device is also plotted for comparison. Differently from what observed in the N_{DB} study, two different mechanisms coexist in this case leading to a significant density of trapped charge. Dangling bonds are

also positively (negatively) charged in the p/i (i/n) region, but additional charge density is given by the concentration of negatively charged acceptors being considered in this section, which enhance the electric field at the i/n region at the expense of the p/i one. As a result, an asymmetric behaviour is obtained (Fig. 7.11). The opposed behaviour is observed when dealing with donor-like impurities, for which E_i is enhanced at the p/i junction. In fact, *p-i-n* devices exhibiting a certain amount of acceptor-like impurities present a p^+-*p*-n^+ character, whereas the incorporation of donor-like contaminants leads to a p^+-*n*-n^+ behaviour.

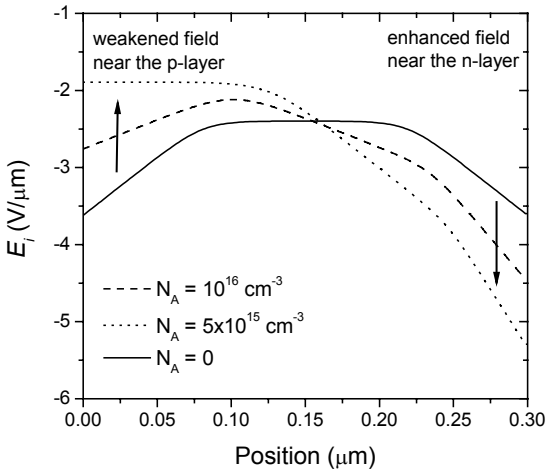

Figure 7.11. *Simulated electric field profile for a contaminated (p-type) active layer. Note the enhanced (weakened) electric field in the i/n (p/i) interface at increasing N_A values.*

DICE and experimental results pointed to poor properties at the p/i junction, whose behaviour is of crucial importance in the overall photovoltaic performance [Herbst et al. 1995, Isomura et al. 1993]. Thus, a non-uniform incorporation of contaminants (provoked by boron diffusion from the p-type layer for instance), instead of a uniform one (as that considered in Figure 7.11), should be considered. In this case, two different acceptor contaminant concentrations were simulated, $N_A = N_{DB} = 10^{17}$ cm^{-3} and $N_A = N_{DB} = 5\times10^{16}$ cm^{-3} for the first 100 nm near the p/i junction ("death zone"). Regarding the rest of the intrinsic layer, $N_{DB} = 10^{16}$ cm^{-3} and no acceptor contaminants were considered. Simulations shown in Fig. 7.12 exhibit a similar comportment to that experimentally observed, and to the one obtained when solar cells exhibiting clean active layers with intermediate N_{DB} (~10^{17} cm^{-3}) values were considered. Therefore, two different regions,

one of them optically limited (long wavelengths) and the other one controlled mainly by electrical properties (short wavelengths), could be distinguished.

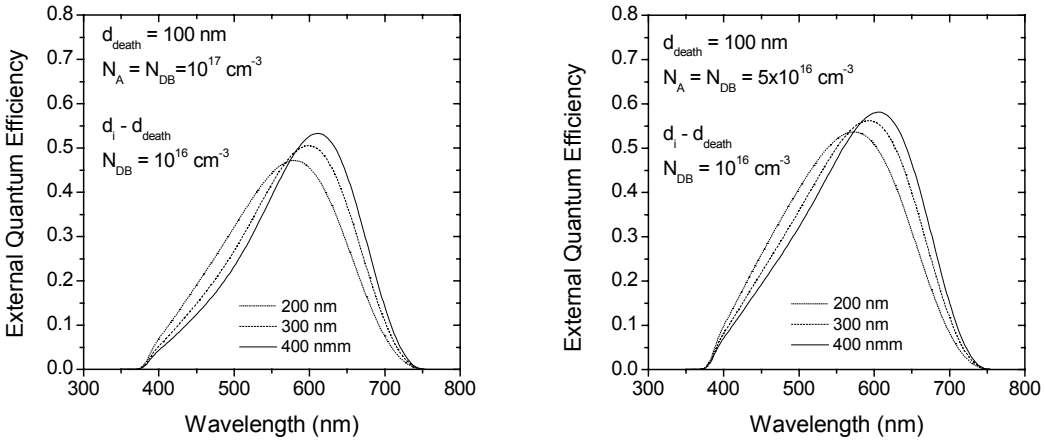

a) *b)*

Figure 7.12. *Numerical simulation of the spectral response of solar cells exhibiting contaminated (100 nm) active layers. Two different N_A values were considered: 10^{17} cm^{-3} (a) and 5×10^{16} cm^{-3} (b).*

7.3. Summary

The behaviour of solar cells was simulated by means of both *DICE* analysis and numerical resolution of the defining equations. These simulations allowed us to consider the effects of non-idealities, such as dangling bond distribution or incorporation of contaminants. Furthermore, the optical properties of the different layers, especially those referred to the front contact, were observed to play a very important role.

Optical losses were identified as one of the crucial aspects in our devices. Thus, and once the absorption spectra of both nc-Si:H and a-Si:H had been evaluated, spectral response simulations were performed. Very significant absorption at the front contact (p-type double structure) leading to very low external quantum efficiencies, especially in the short wavelength region, was observed as already predicted in *Chapter 6*.

Furthermore, the dependence on d_i permitted to extract additional information regarding our device physics. Thus, poor electrical properties (especially in the region close to the p/i

interface) at increasing thickness led to simulation results comparable (at least qualitatively) to experimental ones. Electrical features were seen to determine the photovoltaic operation of our devices at short wavelengths, whereas increased optical absorption achieved at higher d_i led to enhanced performance for increasing thicknesses at long wavelengths. Different reasons might be pointed as leading to the observed behaviour. Thus, relatively high N_{DB} values (10^{17} cm^{-3}) in clean (non-contaminated) devices led to a similar comportment to that experimentally observed. Our state-of-the-art a-Si:H exhibited a density of dangling bonds (N_{DB}) around 5×10^{16} cm^{-3} and both structural and optoelectronic properties were quite satisfactory. A comparable qualitative effect was observed in our simulation when contaminated active layer layers were considered (even when dealing with low N_{DB} values). In that sense, chemical instabilities at the p-type layer might lead to diffusion of boron atoms into the active layer and, eventually, to degradation of the p/i interface [Grunsky et al. 2004]. In fact, this result might be related with experiments presented in section 6.7, where chemical stabilization seemed to lead to irreversible changes in the device performance. Consequently, a combined effect could not be discarded, though the acceptable properties of the intrinsic material and its satisfactory behaviour at long wavelengths when incorporated as the active layer of solar cells seemed to point out the dominant role of the front contact instabilities, which was then identified as the main factor limiting the behaviour of deposited solar cells.

Conclusions

- Deposition of hydrogenated amorphous silicon for photovoltaic applications by Hot-Wire Chemical Vapour Deposition was carried out. The role of the different parameters involved in the growth mechanism (filament temperature, pressure, hydrogen dilution, substrate temperature) was analysed to optimise the properties of the deposited material. The substrate temperature was kept at relatively low values ($T_s \leq 200$ºC) throughout most of the work to allow the future use of low cost substrates.

- A wide range of microstructure features ranging from purely amorphous to highly crystalline ($X_c > 0.65$) was achieved after suitably tuning the deposition parameters. High T_f, *P* and/or D_H allowed the deposition of highly crystalline material, even when dealing with low substrate temperatures ($T_s = 200$ºC). In all cases, the enhanced production of atomic hydrogen was pointed as the fundamental mechanism leading to increased crystallinity, due to the selective etching of the amorphous tissue and the enhanced diffusion of precursors caused by the coverage of the growing surface. Furthermore, an abrupt transition from a-Si:H to nc-Si:H was observed, especially when the influence of either D_H or *P* were analysed. On the other hand, an increase of T_s alone in the range under study (actual substrate temperature below 400ºC) proved to be an insufficient procedure to grow nc-Si:H, as long as the rest of the deposition parameters were not shifted to conditions favouring the production of H.

- Intrinsic a-Si:H exhibiting a compact structure ($R^* \sim 0.11$, $E_u \sim 55$ meV) and suitable electrical features ($\sigma_d \sim 1\times10^{-10}$ $\Omega^{-1}cm^{-1}$, $\sigma_{ph} \sim 5\times10^{5}$ $\Omega^{-1}cm^{-1}$, $L_D > 200$ nm) was obtained. The set of growth conditions leading to our state-of-the-art material was identified, although its dependence on geometrical issues and the correlation between parameters did not allow to clearly define a unique set of optimised conditions. Anyhow, both the nature of the growth precursors and the concentration of atomic hydrogen were proved to play a leading role. High mobility species led to compact structures and, eventually, to enhanced optoelectronic properties. On the other hand, a sufficient amount of H leading to improved surface mobility and favouring the production of high mobility species through secondary reactions was also necessary.

- T_f between 1550 and 1650ºC led to our best a-Si:H when using inverted basket shaped filaments, as this range resulted in the appropriate generation of H. Nevertheless, filament characteristics clearly affected the atomic hydrogen production, so that increased T_f values were required when dealing with wires exhibiting lower areas and vice versa.

- The nature of the growth precursors was clearly affected by the process pressure. In particular, P and $d_{f\text{-}s}$ were clearly related, so that $P \cdot d_{f\text{-}s} \sim 4$ - 12 Pa·cm were required in our case to obtain device-quality a-Si:H. These values resulted in high mobility species through and adequate number of secondary reactions. In our case, $d_{f\text{-}s}$ ranged between 3 and 5 cm, so that P between 1×10^{-2} and 3×10^{-2} mbar were used.

- D_H was also observed to strongly affect the properties of the material. In that sense, the production of H in our reactor was very efficient, so that only a very subtle improvement could be observed at moderate hydrogen dilutions ($D_H \leq 25\%$). Larger D_H values led to unsuitable properties or to the growth of nc-Si:H.

- The ability to deposit both p- and n-type a-Si:H doped layers by means of Hot-Wire CVD after the addition of B_2H_6 and PH_3 respectively was evaluated.

- n-type a-Si:H was deposited at similar conditions to those leading to our state-of-the-art intrinsic a-Si:H. An atomic ratio gas phase ([P]/[Si]) of 1% was used, which led to acceptable electrical properties ($\sigma_d > 10^{-3}\ \Omega^{-1}cm^{-1}$ and $E_A < 0.3$ eV).

- The deposition of device-quality p-type a-Si:H was more complicated, as those conditions leading to our best intrinsic a-Si:H did not result in suitable material. Low σ_d ($\sim 10^{-6}\ \Omega^{-1}cm^{-1}$) was obtained when [B]/[Si] ratios between 1 and 2% were employed. Nevertheless, both annealing of the samples and utilization of higher doping ratios (~10%) led to satisfactory σ_d ($\sim 10^{-4}\ \Omega^{-1}cm^{-1}$) and E_A (0.4 eV) values. In particular, too high hydrogen concentrations ($C_H \sim 16\%$) might have been responsible for the observed behaviour. Boron atoms are known to form boron-hydrogen complexes, which can be removed after increasing the temperature, thus favouring the release of hydrogen and allowing the boron atoms to effectively contribute to the

doping of the material. On the other hand, the use of [B]/[Si] ~ 10% seemed to allow a sufficient number of boron atoms to effectively dope the material despite the formation of B-H complexes, although the large amount of B atoms in this case resulted in a too disordered material. Finally, p-type nc-Si:H was also deposited joining high conductivity and low optical absorption. In this case, suitable electrical properties ($\sigma_d > 2\ \Omega^{-1}cm^{-1}$ and $E_A < 0.02$ eV), even for thicknesses below 50 nm, were obtained.

- Doped layers are grown on different substrates when applied to solar cell structures. Therefore, the substrate influence on the doped layers properties was analysed. Stainless steel promoted crystalline growth when n-type layers were considered, whereas enhanced crystallinity on glass was achieved for p-type material. Moreover, the electrical properties in the direction perpendicular to the substrate were mainly determined by the junction properties, which were clearly better for the n-type material than for the p-type one.

- The above-mentioned results concerning material properties were applied in the deposition of our first a-Si:H based solar cells completely grown by Hot-Wire CVD. These preliminary results concerned the analysis of several structures involving different front and back contact designs. Our best results were achieved either in entirely a-Si:H structures deposited on textured SnO_2:F substrates (Asahi-U), or in solar cells having a p-type double layer (nc-Si:H/a-Si:H) grown on ZnO:Al coated Asahi-U, for which initial efficiencies around 4 and 4.5%, respectively, were measured.

- The response of our devices at long wavelengths attested the acceptable performance of the back contact, where the implementation of a back reflector effectively improved the photovoltaic operation. Nevertheless, the front contact limited the achievable J_{sc}, which lay around 10 mA/cm^2 in the most favourable cases, thus giving evidence of serious problems at both the TCO and the p-type layer. On one hand, the use of bare Asahi-U was limited to completely a-Si:H devices, as Asahi-U degrades when exposed to high H concentration involved. Conversely, ZnO:Al coated Asahi-U, whose optoelectronic properties were worse than those of bare Asahi-U, had to be used when front contacts involving nc-Si:H layers were considered. Regarding the p-type layer, several problems arose from the difficulty to effectively dope p-type a-Si:H obtained by Hot-Wire CVD.

Hence, the low doping efficiency required the use of very thick layers to ensure the correct diode behaviour. Unfortunately, such thick layers led to significant optical losses.

- The behaviour of our solar cells was simulated by means of both the dynamic inner collection efficiency analysis (*DICE*) and numerical resolution of the device defining equations. Coherently with experimental results, optical losses were identified as one of the crucial factors limiting the behaviour of our devices.

- Numerical simulation demonstrated that electrical features, which were degraded for increasing thickness of the active layer, determined the photovoltaic operation at short wavelengths. On the contrary, enhanced optical absorption at high active layer thickness led to improved performance at long wavelengths. From comparison between experimental and simulation results, problems associated to contaminants coming from the unstable p-type layer were identified as the main factor limiting the performance of the solar cells.

- Our first a-Si:H based solar cells completely grown by Hot-Wire CVD at low T_s were deposited. As far as intrinsic material is concerned, satisfactory results were obtained, thus making the employed technique a promising alternative for industrial application. Nevertheless, further research, especially in the front contact, is necessary before industrial implementation. In particular, the use of alternative p-type materials and the optimisation of both the TCO and the light trapping strategies are expected to be carried out.

Annexe: Additional applications

Although most of our efforts were devoted to the development of hydrogenated amorphous silicon (a-Si:H) by Hot-Wire Chemical Vapour Deposition (Hot-Wire CVD) for application in thin film silicon solar cells, our state-of-the-art material (both intrinsic and doped) was also incorporated in other devices. In particular, the implementation of our layers into thin film transistors and heterojunction solar cells was studied in cooperation with different research centres. It is not the objective of this annexe to deeply describe the implementation of such devices, so that only the motivation and the most remarkable results concerning such applications will be briefly presented.

A.1. Silicon based thin film transistors

A.1.1. Introduction

Nowadays, flat-panel displays (FPD) can be found in a wide range of products, such as, watches, portable computers, cellular phones, or personal digital assistants (PDAs). Among flat-panels displays, the active matrix liquid crystal displays (AMLCD), where thin film transistors (TFT) play a very remarkable role, are extensively used [Wagner et al. 2003]. These AMLCDs are composed of a matrix of picture elements (pixels), which create an image. Figure A.1 shows the structure of an AMLCD, where the path of light and the different layers building up the device can be seen.

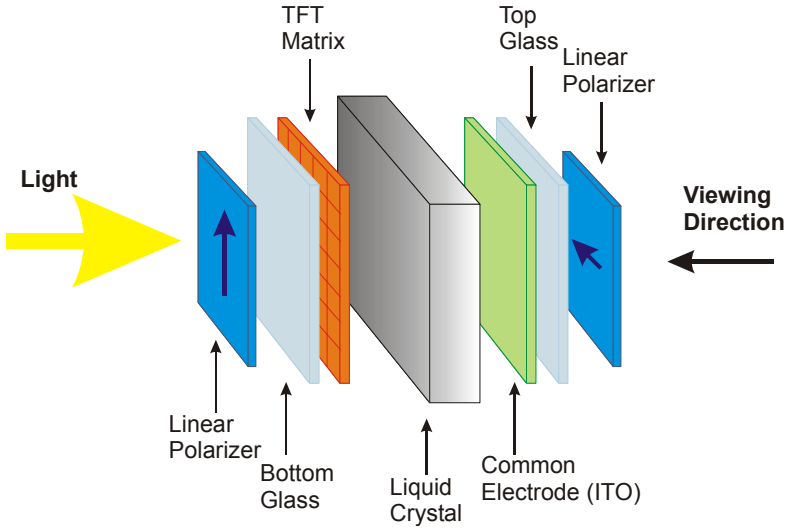

Figure A.1. *Schematic cross-section of an active matrix liquid crystal display.*

As seen in Fig. A.1, a standard AMLCD consists of two glass panels (top and bottom) with liquid crystal (LC) injected between them. The surfaces of both the bottom and the top glass are coated with lineal polarizers with perpendicular orientations, whereas a light source is positioned behind the bottom glass. Thus, light coming from the light source is polarized by the first polarizer before crossing the LC, whose state affects the polarization of the light. In the "off" state, the LC leads to the rotation of the incoming polarization (90º), so that light can cross the second polarizer, thus resulting in high transparency. On the other hand, if the pixel is "on", the LC molecules align in a single direction parallel to the incoming light, this fact allowing the light to cross unaltered. Consequently, the light is blocked and the pixel results black. The on/off states are defined by the electric field along the liquid crystal, formed between the common electrode (ITO in the figure) and the TFT matrix. Thus, the function of the TFTs as switching elements can be easily understood. When a voltage is applied to the pixel (by applying a pulse to the gate and the drain of the transistor), the LC molecules align themselves parallel to the induced electric field (off or blocking state). In this state, the pixel will appear black, whereas the opposite behaviour is observed when no voltage is applied. Besides, different grey levels can be achieved by properly tuning the voltage applied to the electrode.

The role of the TFTs as switching elements determines the requirements for their use [Stannowski 2002]. Thus, on-currents above 10^{-6} A allowing a short response time, high field-effect mobilities (μ around 1 cm^2/Vs) leading to the mentioned on-currents, low off-currents ($<10^{-12}$ A) preventing significant leakage currents, relatively low threshold voltage (V_T), defined as the gate-source voltage at which conduction electrons begin to appear in the channel, low inverse subthreshold slope (S) of the transfer characteristics in order to assure fast transitions between the "on" and the "off" state and, finally, stability upon gate-voltage stress, are demanded. Moreover, low processing temperatures (200ºC) are desirable for compatibility with low-cost substrate materials such as plastics.

Amorphous silicon TFTs have been proved to fulfil the above-presented demands, what has led to its wide application in AMLCDs. Besides, the use of Hot-Wire CVD has led to several advantages over PECVD, such as improved stability, high deposition rates, or easy scalability to large area. Consequently, TFTs were developed in collaboration with the *Université de Rennes 1*.

A.1.2. Experimental

n-type TFTs in top gate configuration (Figure A.2) were processed using 200 nm thick a-Si:H silicon films, exhibiting our state-of-the-art properties. 2×2 square inch glass substrates covered with 200 nm thick SiO_2 layers grown by Atmospheric Pressure CVD (APCVD) at *Université de Rennes 1* were employed.

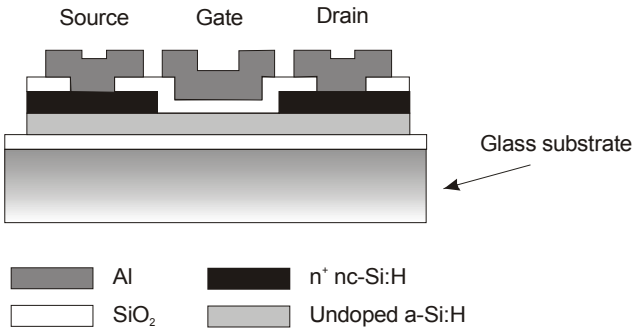

***Figure A.2**. Cross-section of the n-type TFTs.*

The growth of both the undoped and the n-type nc-Si:H layers was carried out at our laboratory. The deposition conditions for the 200 nm thick a-Si:H layer were those presented in *Chapter 4*, that is, filament temperature (T_f) of around 1680ºC, substrate temperature (T_s) of 200ºC, process pressure (P) of 1×10^{-2} mbar and no hydrogen dilution (D_H). A 150 nm-thick n-type nc-Si:H layer was deposited on the a-Si:H layer by adding PH_3 to the gas mixture so that [P]/[Si] was 2%, while T_f ~1610ºC, $P = 3\times10^{-2}$ mbar and D_H = 95% (4 sccm SiH_4 and 76 sccm H_2) were used. Besides, and as already seen in our solar cells, different chambers were employed to deposit intrinsic a-Si:H and n-type nc-Si:H. The doped layer was plasma etched to define the channel and the source and drain regions for each transistor as seen in Figure A.2. Then, a 100 nm-thick SiO_2 layer was deposited by RF sputtering to ensure the gate insulation. The gate insulator fabrication is one of the most crucial steps that determines the TFT performance and was carried out at the *University of Rennes 1*. Particularly, the use of low temperatures makes it difficult to attain high quality gate insulator. Details regarding the growth of this layer can be found in [Fonrodona et al. 2004]. Subsequently, aluminum was thermally evaporated and wet etched to form the source, drain and gate electrodes. Finally, post-metallization annealing was performed at 200ºC in an atmosphere of forming gas.

TFTs with different channel length (L between 20 and 80 μm) and width (W ranging from 20 to 100 μm) were fabricated. TFTs were characterized at 25ºC and the usual device parameters were measured: threshold voltage (V_T), transconductance (g_m), field effect mobility (μ) and subthreshold slope (S). V_T and g_m were deduced in the linear regime, for which V_T is the intercept of the transfer characteristics ($I_{DS}(V_{GS})$) with the gate voltage (V_{GS}) axis, and g_m is the slope of the linear fit. μ is then deduced from the relation:

$$\mu = g_m \cdot (L/W) \cdot (1/C_{ox}) \cdot (1/V_{DS}) \qquad (A.1)$$

where C_{ox} is the gate oxide capacitance per area unit, $C_{ox} = (\varepsilon_0 \cdot \varepsilon_{ox})/t_{ox}$, t_{ox} being the oxide thickness. S is the inverse slope of the transfer characteristics using logarithmic plot. Finally, stress experiments were performed using a negative gate voltage of -10 V.

A.1.3. Results

The transfer characteristics of the obtained TFTs can be seen in Fig. A.3(a), from where quite low S and V_T can be deduced. Thus, S of 0.6 V/dec indicating quite an abrupt transition and V_T around 3.5 V were determined. Besides, significantly high values around 1.3 $cm^2V^{-1}s^{-1}$ were obtained for the electric field mobility when compared with different reported values [Stannowski et al. 2002, Wagner et al. 2003], this fact pointing out the suitable properties of our state-of-the-art material.

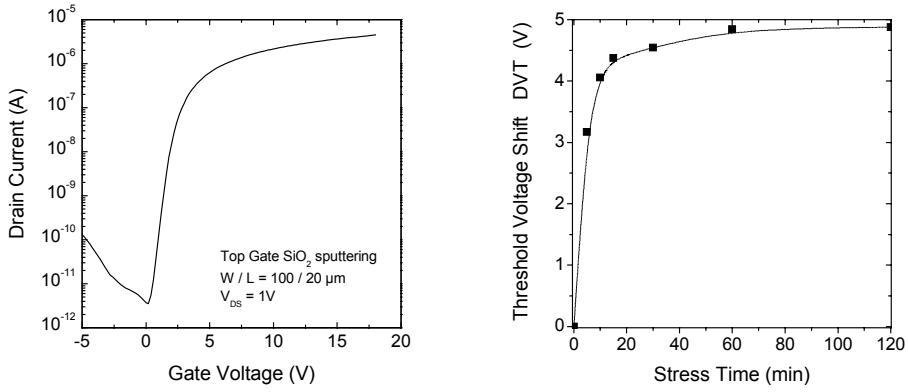

a) *b)*

Figure A.3*.Transfer characteristics of a Hot-Wire CVD a-Si:H TFT (a). Threshold voltage shift under –10 V gate bias (b).*

Regarding the stability analysis, the TFTs were stressed under -10 V gate bias. Fig. A.3(b) shows the variation of V_T under stress. A pronounced V_T shift was observed in accordance with expected results, which points to stability problems most likely attributable to metastable defect creation in the material [Stannowski and Schropp 2001].

In summary, our state-of-the-art amorphous deposited by Hot-Wire CVD at low substrate temperature (200ºC) was implemented in coplanar top gate n-type TFTs. Layers were deposited onto SiO_2 coated glass and gate insulation was achieved by means of high quality RF sputtered SiO_2. a-Si:H devices exhibited mobility values of 1.3 $cm^2V^{-1}s^{-1}$, which are remarkably high taking into account the amorphous nature of the material and comparable to best values reported.

A.2. Heterojunction solar cells

A.2.1. Introduction

Silicon-heterojunction solar cells combining both crystalline-silicon and amorphous silicon are among the most promising candidates for high efficiency solar cells processed at low temperatures. The junction of conventional crystalline silicon (c-Si) solar cells is formed by thermal diffusion at around 900ºC. On the other hand, the main recombination mechanism occurs at external surfaces, so that electrical passivation becomes a critical aspect. Moreover, the trend to reduce production costs leads to the employment of thinner wafers, for which this issue becomes increasingly important. In that sense, the passivation of silicon wafers is classically performed by thermal oxidation at high temperature (>1000ºC) [Voz et al. 2003].

High temperature steps are undesirable, as they lead to increased production costs. Furthermore, heterojunctions can be obtained at low temperatures (<300 ºC) by depositing thin silicon films on crystalline silicon wafers in the so-called heterojunction approach. The most usual technique to grow thin silicon films for heterojunction formation is Plasma-Enhanced Chemical Vapour Deposition (PECVD), which has led to commercially available modules. In particular, the HIT structure (Heterojunction with Intrinsic Thin layer) by Sanyo Electric Co., where a thin intrinsic layer is inserted between the p-type

a-Si:H and the n-type c-Si wafer, has allowed a highest efficiency of 19.5 % for mass-produced solar cells [Taguchi et al. 2000]. Moreover, Sanyo has applied the same principle to the back contact with excellent results, leading to satisfactory back contact passivation at low process temperature. Figure A.4 shows the structure of the heterojunction solar cells in which our Hot-Wire CVD layers were implemented. The architecture of the device is very similar to the HIT cell one, although p-type c-Si wafers are used. Regarding the role of the additional intrinsic layer between the heteroemitter (n-type a-Si:H) and the wafer, it is presumed that the intrinsic amorphous silicon thin layer reduces surface recombination resulting in satisfactory passivation. This effect increases the open circuit voltage of the solar cell due to the reduced saturation current density.

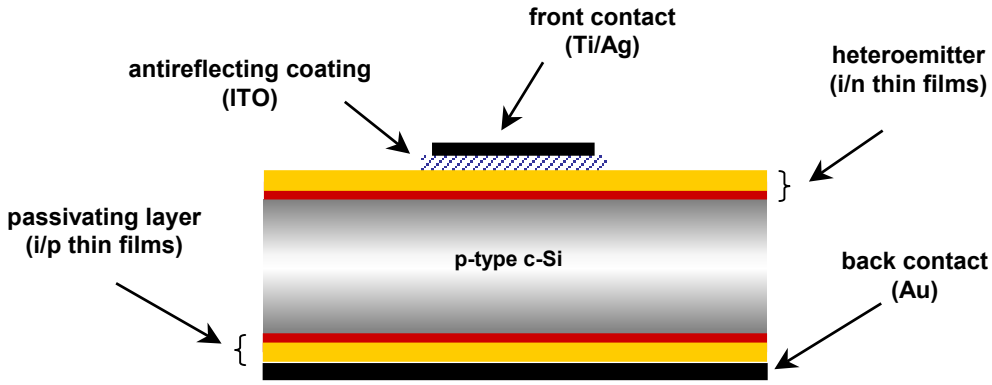

Figure A.4*.The structure of a heterojuncion solar cell.*

In our case, the possibility to fabricate heterojunction devices by Hot-Wire CVD was analysed in cooperation with the *Universitat Politècnica de Catalunya*. In particular, the lack of ion bombardment in Hot-Wire CVD could result beneficial for the interface between amorphous and crystalline silicon. Different groups have reported on heterojunction solar cells grown by Hot-Wire CVD. Among these, some of the most promising results have been presented by [Wang et al. 2003], whose solar cells exhibited V_{oc} = 580 mV, J_{sc} = 29.86 mA/cm^2 and FF = 0.773 for a conversion efficiency of 13.3 % under one-sun illumination. This group deposited an n-type μc-Si:H emitter on p-type c-Si with a thin (50 Å) intrinsic a-Si:H buffer layer. Moreover, improved results by using the same structure were reported very recently by the same group after lowering the substrate temperature [Iwaniczko et al. 2004]. Thus, solar cells with V_{oc} above 620 mV and η higher than 14% were obtained at T_s values around 100ºC. On the other hand, heterojunction solar

cells with a p-type μc-Si:H emitter on n-type c-Si with a thin (20 Å) p-type a-Si:H seed layer have been developed leading to V_{oc} = 532 mV, J_{sc} = 26.6 mA/cm^2 and FF = 0.74 for a conversion efficiency of 10.6 % [Mukherjee et al. 2001].

In our case, preliminary studies on electronic surface passivation of both p- and n-type doped c-Si wafers by means of intrinsic a-Si:H films were performed [Voz et al. 2003]. Subsequently, p-type nc-Si:H was deposited on intrinsic a-Si:H exhibiting varying thicknesses to form heteroemiters and back contacts on n- and p-type c-Si wafers respectively [Voz et al. 2003b]. Finally, n-type a-Si:H thin films were analysed to grow our first bifacial heterojunction solar cells with the structure shown in Fig. A.4. A p-type nc-Si:H was incorporated in the back contact, as p-type a-Si:H exhibited poor electronic properties as seen in *Chapter 5*.

A.2.2. Experimental

400 μm thick float zone (FZ) silicon wafers (100) were used for all heterostructures considered. Silicon wafers were cleaned in a H_2SO_4:H_2O_2 (2:1) solution, dipped in 5% HF and immediately introduced into the load lock chamber of the Hot-Wire CVD set-up at our laboratory. Deposition conditions leading to our state-of-the-art material were used for all Hot-Wire CVD grown layers (Table A.1). In this case, tantalum wires 0.5 mm in diameter were installed in both reactors leading to deposition rates around 2 Å/s for the p-type doped nc-Si:H and a-Si:H films and 4 Å/s for the n-type a-Si:H ones.

Type	***T_f (ºC)***	***T_s (ºC)***	***H_2 (sccm)***	***SiH_4 (sccm)***	***Doping (%)***	***P (mbar)***
i a-Si:H	*1680*	*200*	*-*	*4*	*-*	*1×10^{-2}*
n a-Si:H	*1680*	*200*	*-*	*4*	*1*	*1×10^{-2}*
p a-Si:H	*1850*	*125*	*-*	*4*	*1*	*1×10^{-2}*
p nc-Si:H	*1750*	*125*	*100*	*4*	*5*	*3×10^{-2}*

Table A.1. *Deposition conditions used in this work for the Hot-Wire CVD thin silicon films.*

Three different bifacial heterostructures were studied involving varying back contact

design and buffer layer thickness (Table A.2). In all cases, n-type a-Si:H emitters 50 nm thick were used.

Name	emitter		back conctact	
	n- doped	intrinsic	intrinsic	p-type
A	a-Si:H 50 nm	a-Si:H 10 nm	a-Si:H 10 nm	a-Si:H 50 nm
B	a-Si:H 50 nm	a-Si:H 5 nm	a-Si:H 5 nm	nc-Si:H 50 nm
C	a-Si:H 50 nm	a-Si:H 5 nm	-	nc-Si:H 50 nm

Table A.2. *Heterostructures with n-type amorphous silicon emitter under study.*

A.2.3. Results

First of all, passivation results as measured by Quasy-Steady-State Photoconductivity (QSS-PC) are shown in Figure A.5. QSS-PC is a contact less characterization technique which allows the determination of the effective surface recombination, the emitter saturation current density and the open circuit voltage limit [Sinton and Cuevas 1996, Martín et al. 2002].

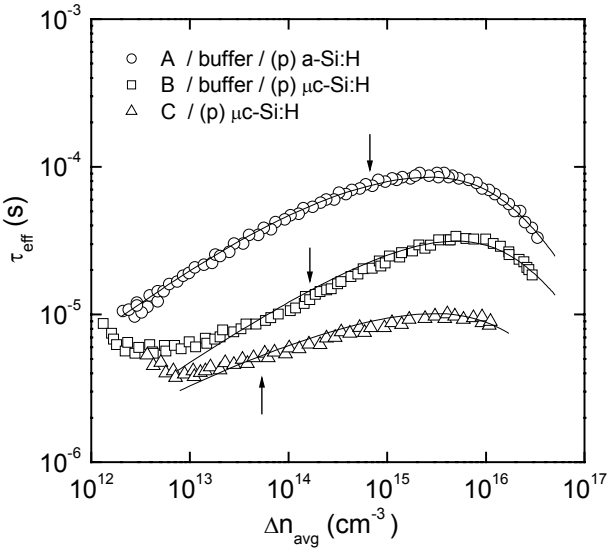

Figure A.5. *QSS-PC data of heterojunctions with n-type a-Si:H emitter.*
The design of the back contact is indicated. The arrows point τ_{eff} values at 1 sun irradiance.

As clearly seen in the figure, structure A yielded the most promising results, with the highest effective lifetime (τ_{eff}) values at one sun illumination. Nevertheless, diodes grown with this structure resulted in a poor carrier injection through the 10 nm thick buffer layer, especially at the back contact due to the poor electrical features of p-type a-Si:H films. Thus, further studies were continued with the thickness of the buffer layer reduced to 5 nm. Besides, a highly conductive p-type doped nc-Si:H layer replaced the a-Si:H one (structure B). The resulting τ_{eff} values were good enough in structure B but poor when the buffer layer at the back side was suppressed in C.

Following the above presented results, the heterostructure B was processed to obtain our first heterojunction solar cell by Hot-Wire CVD. The characteristic J(V) curve at standard illumination conditions can be observed in Fig. A.6. This preliminary device yielded a promising conversion efficiency of 9.0% with V_{oc} = 577 mV, J_{sc} = 24.2 mA/cm^2 and FF = 0.65. Remarkably high V_{oc} was achieved, whereas the low J_{sc} value can be attributed to the absorption of the probably too thick n-type a-Si:H layer. Besides, the grid design could be also improved to allow less shadowing, thus leading to higher J_{sc}. Additionally, the front ITO layer should be thinned to about 80 nm for optimum antireflection effect. Finally, the fill factor should improve after optimising some technological steps to reduce the series resistance.

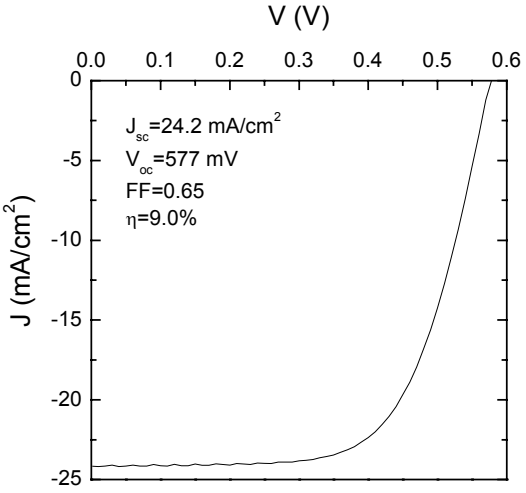

Figure A.6. *J(V) curve of first bifacial heterojunction solar cell by Hot-Wire CVD measured in one-sun conditions.*

In summary, bifacial heterojunction solar cells on p-type c-Si were deposited at low temperatures (200 ºC). Very encouraging results for future fabrication of high efficiency solar cells at low temperature by Hot-Wire CVD were achieved.

References

Abe K., Tsushima T., Ichikawa M., Yamada A., Konagai M., J. Non-Cryst. Solids **266-269** 105 (2000)

Alpuim P., Chu V., Conde J.P., J. Appl. Phys. **86** (7) 3812 (1999)

Alpuim P., Chu V., Conde J.P., J. Non-Cryst. Solids **266-269** 110 (2000)

Alpuim P., Chu V., Conde J.P., J. Vac. Sci. Technol. A **19** (5) 2328 (2001)

An I., Lu Y., Wronski C.R., Collins R.W., Appl. Phys. Lett. **64** (24) 3317 (1994)

Andújar J.L., PhD Thesis, Universitat de Barcelona (1990)

Antoine A.M., Drevillon B., J. Appl. Phys. **63** (2) 360 1988

Asensi J.M., PhD Thesis, Universitat de Barcelona (1994)

Asensi J.M. Merten J., Voz C., Andreu J., J. Appl. Phys. **85** 2939 (1999)

Bauer S., Dusane R.O., Herbst W., Diehl F., Schröder B., Oechsner H., Solar Energy Materials & Solar Cells **43** 413 (1996)

Bauer S., Herbst W., Schröder B., Oechsner H., Frammelsberger W., Schade H., Proc. of the 14th European Photovoltaic Solar Energy Conference, Barcelona, 617 (1997)

Bauer S., Schröder B., Herbst W., Lill M., Proc. of the 2nd Word Conference and Exhibition on Photovoltaic Solar Energy Conversion, Vienna, 363 (1998)

Bauer S., Schröder B., Oechsner H., J. Non-Cryst. Solids **227-230** 34 (1998b)

Beeman D., Tsu R., Thorpe M.F., Phys. Rev. B **32** (2) 878 (1985)

Beyer W., Solar Energy Materials & Solar Cells **78** 235 (2003) *and references therein*

Bourée J.E., Thin Solid Films **395** 157 (2001)

Branz H.M., Solid State Comm. **105**, 387 (1998)

Brockhoff A.M., Ullersma E.H.C., Meiling H., Habraken F.H.P.M., Weg W.F. van der, Appl. Phys. Lett. **73** (22) 3244 (1998)

Brogueira P., Conde J.P., Arekat S., Chu V., J. Appl. Phys. **79** (11) 8748 (1996)

Brogueira P., Chu V., Ferro A.C., Conde J.P., J. Vac. Sci. Technol. A **15** (6) 2968 (1997)

Brüggermann R., Kleider J.P., Longeaud C., Mencaraglia D., Guillet J., Bourée J.E., Niikura C., J. Non-Cryst. Solids **266-269** 258 (2000)

Brühne K., Schubert M.B., Köhler C., Werner J.H., Thin Solid Films **395** 163 (2001)

Bustarret E., Hachicha M.A., Brunel M., Appl. Phys. Lett. **52** (20) 1675 (1988)

Bustarret E., Vaillant F., Hepp. B., Mat. Res. Soc. Symp. Proc. **118**, 123 (1988b)

Caputo D., Solar Energy Materials & Solar Cells **59** 289 (1999)

Carlson D.E., Wronski C.R., Appl. Phys. Lett. **28** 671 (1976)

Chatam H., Bhat P., Benson A., Matovich C., J. Non-Cryst. Solids **115** 201 (1989)

Chatterjee P., Palit N., Hamma S., Proc. of the 2nd Word Conference and Exhibition on Photovoltaic Solar Energy Conversion, Vienna, 933 (1998)

Chittick R.C., Alexander J.H., Sterling H.F., J. Electrochem Soc. **116** 77 (1969)

Cifre J., Bertomeu J., Puigdollers J., Polo M.C., Andreu J., Lloret A., Appl. Phys. A **59** 645 (1994)

Cody G.D., Tiedje T., Abeles B., Brooks B., Goldstein Y., Phys. Rev. Lett. **47** 1480 (1981)

Collins R.W., Appl. Phys. Lett. **53** (12) 1086 (1988)

Conde J.P., Alpuim P., Boucinha M., Gaspar J., Chu V., Thin Solid Films **395** 105 (2001)

Curtins H., Veprek S., Solid State Communications **57** (4) 215 (1986)

Dalal V.L., Leonard M., Baldwin G., J. Non-Cryst. Solids **71** 164 (1993)

Dalal V.L., Maxson T., Han K., Haroon S., J. Non-Cryst. Solids **227-230** 1257 (1998)

Doyle J., Robertson R., Lin G.H., He M.Z., Gallagher A., J. Appl. Phys. **64** (6) 3215 (1988)

Drevillon B., Kumar S., Roca i Cabarrocas P., Siefert J.M., Appl. Phys. Lett. **54** (21) 2088 (1989)

Duan H.L., Zaharias G.A., Bent S.F., Extended Abstract on the Second International Conference on the Cat-CVD (Hot-Wire CVD) Process, Denver, 121 (2002)

Duan H.L., Zaharias G.A., Bent S.F., Current Opinion in Solid State & Materials Science **6** 471 (2002b)

Dusane R.O., Suvarna R., Dusane S.R., Bhide V.G., Kshirsagar S.T., Appl. Phys. Lett. **63** 2201 (1993)

Escarré J., Villar F., Fonrodona M., Soler D., Asensi J.M., Bertomeu J., Andreu J., presented at the 19th European Photovoltaic Solar Energy Conference and Exhibition, Paris (2004)

Feenstra K.F., PhD Thesis, Universiteit Utrecht (1998)

Feenstra K.F., Schropp R.E.I., Van der Weg W.F., J. Appl. Phys. **85** (9) 6843 (1999)

Fischer D., PhD Thesis, Université de Neuchâtel (1994)

Fonrodona M., Soler D., Bertomeu J. Andreu J., Thin Solid Films **395** 125 (2001)

Fonrodona M., PhD Thesis, Universitat de Barcelona (2003)

Fonrodona M., Soler D., Escarré J., Villar F., Bertomeu J., Andreu J., Saboundji A., Coulon N., Mohammed-Brahim T., presented at the 3rd Conference on Hot-Wire CVD (Cat-CVD) Process, Utrecht (2004)

Fontcuberta i Morral A., Roca i Cabarrocas P., Thin Solid Films **383** 161 (2001)

Forohui A.R., Bloomer I., Phys. Rev. B. **34** (10) 7018 (1986)

Franken R.H., Van Veen M.K., Van der Werf C.H.M, Löffler J., Rath J.K., Schropp R.E.I., presented at the 19th European Photovoltaic Solar Energy Conference and Exhibition, Paris (2004)

Fulop G., Doty M., Meyers P., Betz J., Liu C.H., Appl. Phys. Lett. **40** (4) 327 (1982)

Gallagher A., Thin Solid Films **395** 25 (2001)

Godet C., Layadi N., Roca i Cabarrocas P., Appl. Phys. Lett. **66** 3146 (1995)

Graf U., Meier J., Kroll U., Bailat J., Droz C., Vallat-Sauvain E., Shah A., Thin Solid Films, **47** 37 (2003)

Green M.A., SOLAR CELLS Operating Principles, Technology and System Applications, The University of New South Wales, Kensington (1992)

Green M.A., Emery K., King D., Igari S, Warta W., Progress in Photovoltaics: Research and Applications **12** 55 (2004)

Grunsky D., Kupich M., Schroeder B., presented at the 3rd International Conference on Hot-Wire CVD (Cat-CVD) Process, Utrecht (2004)

Guha S., Narasimhan K.L., Pietruszko S.M., J. Appl. Phys. **52** (2) 859 (1981)

Guha S., Yang J., Nath P., Hack M., Appl. Phys. Lett. **49** (4) 219 (1986)

Guha S., Yang J., Williamson D.L., Lubiniaker Y., Cohen J.D., Mahan A.H., Appl. Phys. Lett. **74** (13) 1860 (1999)

Guha S., Yang J., Banerjee A., Progress in Photovoltaics: Research and Applications **8** 107 (2000)

Guha S., Yang J., Banerjee A., Yan B., Lord K., Solar Energy Materials & Solar Cells 78 329 (2003)

Han D., Yue G., Lorentzen J.D., Lin J., Habuchi H., Wang Q., J. Appl. Phys. **87** (4) 1882 (2000)

Han D., Wang K., Owens J.M., Gedvilas L., Nelson B., Habuchi H., Tanaka M., J. Appl. Phys. **93** (7) 3776 (2003)

Han D., Lorentzen J.D., Weinberg-Wolf J., McNeil L.E., Wang Q., J. Appl. Phys. **94** (5) 2930 (2003b)

Hanafusa A., Aramoto T., Tsuji M., Yamamoto T., Nishio T., Veluchamy P., Higuchi H., Kumazawa S., Shibutani s., Nakajima J., Arita T., Ohyama H., Hibino T., Omura K., Solar Energy Materials & Solar Cells **67** 21 (2001)

Hazra S., Ray S., Solid State Communications **109** 125 (1999)

Heintze M., Zedlitz R., Wanka H.N., Schubert M.B., J. Appl. Phys. **79** (5) 2699 (1996)

Henini M., III-Vs Review **13** (4) 34 (2000)

Herbst W., Dudel J., Scholz A., Schröder B., Oechsner H., Solar Energy Materials & Solar Cells **37** 55 (1995)

Horbach C., Beyer W., Wagner H., J. Non-Cryst. Solids **137-138** 661 (1991)

Ichiwaka Y., Aizawa K., Shimabukuro H., Nagao Y., Sakai H., Technical Digest of the International PVSEC-3, Tokyo, Japan A-Ip-5 (1987)

Ichikawa M., Tsushima T., Yamada A., Konagai M., Jpn. J. Appl. Phys. **39** 4712 (2000)

Ide Y., Asakusa K., Yamada A., Konagai M., Jpn. J. Appl. Phys. **42** 1521 (2003)

Iiduka R., Heya A., Matsumura H., Solar Energy Materials & Solar Cells **48** 279 (1997)

Imamori K., Masuda A., Matsumura H., Thin Solid Films **395** 147 (2001)

Ishibashi K, Thin Solid Films **395** 55 (2001)

Isomura M., Takahma T., Tsuda S., Nakano S., Jpn. J. Appl. Phys. **32** 1902 (1993)

Iwaniczko E., Levi D.H., Page M.R., Wang Q., Yan Y., Teplin C.W., Branz H.M, Wang T.H., presented at the 3rd International Conference on Hot-Wire CVD (Cat-CVD) Process, Utrecht (2004)

Jackson W.B., Aimer N.M., Phys. Rev. B **25** (8) 5559 (1982)

Jackson W.B., Biegelsen D.K., Nermanich R.J., Knoghts J.C., Applf. Phys. Lett. **42** (1) 105 (1983)

Jadkar S.R., Sali J.V., Takwale M.G., Musale D.V., Kshirsagar S.T., Solar Energy Materials & Solar Cells **64** 333 (2000)

Jadkar S.R., Sali J.V., Musale D.V., Kshirsagar S.T., Takwale M.G., Solar Energy Materials & Solar Cells **71** 153 (2002)

Jadkar S.R., Sali J.V., Kshirsagar S.T., Takwale M.G. Thin Solid Films **437** 18 (2003)

Jansen F., Chen I., Machonkin A., J. Appl. Phys. **66** (12) 5749 (1989)

Kamei T., Hata N., Matsuda A., Uchuyama T., Amano S., Tsukamoto K., Yoshioka Y., Hirao T., Appl. Phys. Lett. **68** 2380 (1996)

Kang T.D., Lee H., Park S.J., Jang J., Lee S. J. Appl. Phys. **92** (5) 2467 (2002)

Kasaneva J., PhD Thesis, Universitat de Barcelona (1990)

Kessels W.M.M., Van de Sanden M.C.M., Schram D.C., Appl. Phys. Lett. **72** 2397 (1998)

Klazes R.H., Van Den Broek M.H.L.M., Bezemer J., Radelaar S., Phil. Mag. B **45** 377 (1982)

Klein S., Finger F., Carius R., Wagner H., Stutzmann M., Thin Solid Films **395** 305 (2001)

Klein S., Finger F., Carius R., Rech B., Houben L., Luysberg M., Stutzmann M., Mat. Res. Soc. Symp. Proc. **715**, A26.2 (2002)

Koh J., Ferlauto A.S., Rovira P.I., Wronski C.R., Collins R.W., Appl. Phys. Lett. **75** (15) 2286 (1999)

Kondo M., Toyoshima Y., Matsuda A., Ikuta K., J. Appl. Phys. **80** (10) 6061 (1996)

Kovácik J., Scripta Materialia **39** (2) 153 (1998)

Kubon M., Boehmer E., Siebke F., Rech B., Beneking C., Wagner H., Solar Energy Materials & Solar Cells **41-42** 485 (1996)

Kumar S., Drevillon B., J. Appl. Phys. **65** (8) 3023 (1989)

Kumar P., Kupich M., Grunsky D., Schroeder B., presented at the 3rd International Conference on Hot-Wire CVD (Cat-CVD) Process, Utrecht (2004)

Kupich M., Kumar P, Schröder B., Thin Solid Films **430** 236 (2003)

Langford A.A., Fleet M.L., Nelson B.P., Lanford W.A., Maley N., Phys. Rev. B **45** 13367 (1992)

Le Comber P.G., Spear W.E., Phys. Rev. Lett. **25** (8) 509 (1970)

Levi D.H., Nelson B.P., Perkins J.D., Moutinho H.R., J. Vac. Sci. Technol. A **21** (4) 1545 (2003)

Lucovsky G., Nemanich R.J., Knights J.C., Physical Review B **19** (4) 2064 (1979)

Mahan A.H., Carapella J., Nelson B.P., Crandall R.S., Balberg I., J. Appl. Phys. **69** 6728 (1991)

Mahan A.H., Yang J., Guha S., Williamson D.L., Phys. Rev. B **61** (3) 1677 (2000)

Mahan A.H., Xu Y., Nelson B.P., Crandall R.S., Cohen J.D., Palinginis K.C., Gallagher A.C., Appl. Phys. Lett. **78** 3788 (2001)

Mahan A.H., Xu Y., Williamson D.L., Beyer W., Perkins J.D., Vanecek M., Gedvilas L.M., Nelson B.P., J. Appl. Phys. **90** 5038 (2001b)

Mahan A.H., Xu Y., Iwaniczko E., Williamson D.L., Nelson B.P., Wang Q., Journal of Non-Crystalline Solids **299-302** 2 (2002)

Mahan A.H., Sol. Energy Materials & Solar Cells **78** 299 (2003)

Maley N. Lannin J.S., Phys. Rev. B **36** 1146 (1987)

Martín I., Vetter M., Orpella A., Puigdollers J., Voz C., Marsal L.F., Pallarès J., Alcubilla R., Thin Solid Films **403-404** 476 (2002)

Masuda A., Imamori K., Matsumura H., Thin Solid Films **411** 166 (2002)

Matsui T., Fujibayashi T., Nasuno Y., Fukuhori H., Kanemitsu Y., Kondo M., Matsuda A., Proc. of the 3rd Conference on Photovoltaic Energy Conference, Osaka, 1831, 5P-D4-29 (2003)

Matsumura H., Tachibana H., Appl. Phys. Lett. **47** (8) 833 (1985)

Matsumura H., Jpn. J. Appl. Phys. **25** L949 (1986)

Matsumura H., J. Appl. Phys. **65** (11) 4396 (1989)

Matsumura H., Umemoto H., Masuda A., Journal of Non-Crystalline Solids **338-340** 16 (2004)

Meier J., Dubail S., Platz R., Torres P., Kroll U., Anna Selvan J.A., Vaucher N.P., Hof C., Fischer D., Keppner H., Flückiger R., Shah A., Shklover V., Ufert K.D., Sol. Energy Mater. Sol. Cells **49** 35 (1997)

Merten J., PhD Thesis, Universitat de Barcelona (1996)

Merten J., Muñoz A., Voz C., Andreu J., Meier H., Torres P. Shah A., 14th European Photovoltaic Solar Energy Conference, Barcelona, 1424 (1997)

Merten J., Asensi J.M., Voz C., Shah A.V., Platz R., Andreu J., IEEE Transactions on Electron Devices **45** 423 (1998)

Mickelsen R.A., Chen W.S., Appl. Phys. Lett. **36** (5) 371 (1980)

Miyajima S., Kim M., Ide Y., Yamada A., Konagai M., Jpn. J. Appl. Phys. **42** 3328 (2003)

Molenbroek E.C., Mahan, A.H., Johnson E.J., Gallagher A.C., J. Appl. Phys.**79** (9) 7278 (1996)

Molenbroek E.C., Mahan, Gallagher A.C., J. Appl. Phys. **82** (4) 1909 (1997)

Mukherjee C., Weber U., Seitz H., Schröder B., Thin Solid Films **395** 310 (2001)

Müller J., Kluth O., Wieder S., Siekmann H., Schöpe G., Reetz W., Vetterl O., Lundszien D., Lambetz A., Finger F., Rech B., Wagner H., Solar Energy Materials & Solar Cells **66** 275 (2001)

Müller J., Schöpe G., Rech B., Schade H., Lechner P., Geyer R., Stiebig H., Reetz W., Proc. of the 3rd Conference on Photovoltaic Energy Conference, Osaka, 5P-D4-31 (2003)

Nakada T., Ohbo H., Watanabe T., Nakazawa H., Matsui M., Kunioka A., Solar Energy Materials & Solar Cells **49** 285 (1997)

Nelson B.P., Iwaniczko E., Schropp R.E.I., Mahan A.H., Molenbroek E.C., Salamon S., Crandall R.S., Proc. of the 12th European Photovoltaic Solar Energy Conference, Amsterdam, 679 (1994)

Nelson B.P., Iwaniczko E., Mahan A.H., Wang Q., Xu Y., Crandall R.S., Branz H.M., Thin Solid Films **395** 292 (2001)

Niklasson G.A., Granqvist C.G., J. Appl. Phys. **55** (9) 3382 (1984)

Nubile P., Beloto A.F., Solar Energy Materials & Solar Cells **51** 105 (1998)

Pankove J.I., Carlson D.E., Appl. Phys. Lett. **31** (7) 450 (1977)

Pankove J.I., Zanzucchi P.J., Magee C.W., Lucovsky G., Appl. Phys. Lett. **46** (4) 421 (1985)

Papadopoulos P., Scholz A., Bauer S., Schröder B., Oechsner H., J. Non-Cryst. Solids 164-166 87 (1993)

Peiró D., Bertomeu J., Voz C., Robin G., Andreu J., Proc. of the 2nd Word Conference and Exhibition on Photovoltaic Solar Energy Conversion, Vienna, 766 (1998)

Peiró D., PhD Thesis, Universitat de Barcelona (1999)

Perrin J., Leroy O, Brodage M.C., Contrib. Plasma Phys. **36** 3 (1996)

Puigdollers J., PhD Thesis, Universitat de Barcelona (1995)

Puigdollers J., Cifre J., Polo M.C., Asensi J.M., Bertomeu J., Andreu J., Lloret A., Appl. Phys. Surf. Sci., **86** 600 (1995)

Rath J.K., Schropp R.E.I., Solar Energy Materials and Solar Cells **53** 189 (1998)

Rech B., Wagner H., Appl. Phys. A **69** 155 (1999)

Ritter D., Weiser K., Optics Communications **57** 336 (1986)

Roca i Cabarrocas P., Kumar S., Drevillon B., J. Appl. Phys. **66** (7) 3286 (1989)

Roca i Cabarrocas P., Appl. Phys. Lett. **65** (13) 1674 (1994)

Roca i Cabarrocas P., Hamma S., Sharma S.N., Viera G., Bertran E., Costa J., J. Non-Cryst. Solids **227-230** 871 (1998)

Saito K., Sano M., Matuda K., Kondo T., Nishimoto T., Ogawa K. Kajita I., Proc. of the 2nd Word Conference and Exhibition on Photovoltaic Solar Energy Conversion, Vienna, 351 (1998)

Schlosser V., Breymesser A., Soler D., Fonrodona M., Voz C., Bertomeu J., Proceedings of the 16th ECPVSEC, Glasgow, 510 (2000)

Schröder B., Bauer S., J. Non-Cryst. Solids **266-269** 115 (2000)

Schropp R.E.I., Daey Ouwens J., Landweer G.E.N., Von der Linden M.B., Van der Werf C.H.M., Proc. of the 12th European Photovoltaic Solar Energy Conference, Amsterdam, 699 (1994)

Schropp R.E.I., Zeman M., Amorphous and Microcyrstalline Silicon Solar Cells: Modeling, Materials and Device Technology, Kluwer Academic Publishers (1998)

Schropp R.E.I., Van Veen M.K., Van der Werf, C.H.M., Williamson D.L., Mahan A.H., presented at the 3rd International Conference on Hot-Wire CVD (Cat-CVD) Process, Utrecht (2004)

Serra J., PhD Thesis, Universitat de Barcelona (1991)

Seto Y., Yamamoto T., Arai D., Kondo M., Matsuda A., Proc. of the 3rd Conference on Photovoltaic Energy Conference, Osaka, 5P-D4-26 (2003)

Shah A.V., Meier J., Vallat-Sauvain E., Wyrsh N., Kroll U., Droz C., Graf U., Solar Energy Materials & Solar Cells **78** 469 (2003) *and references therein*

Shimakawa K., J. Non-Cryst. Solids **226-229** 223 (2000)

Sinton R.A., Cuevas A., Appl. Phys. Lett. **69** 2510 (1996)

Smith Z.E., Wagner S., Phys. Rev. Lett. **59** (6) 688 (1987)

Solomon I., Drévillon B., J. Non-Cryst. Solids **164-166** 989 (1993)

Spear W.E., Le Comber P.G., Solid State Communications **17** 1193 (1975)

Staebler D.L., Wronski C.R., Appl. Phys. Lett. **31** 292 (1977)

Stannowski B., PhD Thesis, Universiteit Utrecht (2002)

Stannowski B., Schropp R.E.I, Thin Solid Films **383** 125 (2001)

Stannowski B., Schropp R.E.I, Wehrspohn R.B., Powell M. J., J. Non-Cryst. Solids **299-302** 1340 (2002)

Stöger M., Breymesser A., Schlosser V., Ramadori M., Plunger V., Peiró D., Voz C., Bertomeu J., Nelhiebel M., Schattscheneider P., Andreu J., Physica B **273-274** 540 (1999)

Stradins P., Solar Energy Materials & Solar Cells **78** 349 (2003) *and references therein*

Street R.A., Hydrogenated Amorphous Silicon, Cambridge University Press, Cambridge (1991)

Stroud D., Phys. Rev. B **12** (8) 3368 (1975)

Stroud D., Superlattices and Microstructures **23** (3/4) 567 (1998)

Stutzmann M., Phi. Mag. B **60** (4) 531 (1989)

Taguchi M., Kawamoto K., Tsuge S., Baba T., Sakata H., Morizane M., Uchihashi K., Nakamura N., Kiyama S., Oota O., Progress in Photovoltaics: Research and Applications **8** 503 (2000)

Taira S., Shima M., Murata K., Tanaka M., Proc. of the 3rd Conference on Photovoltaic Energy Conference, Osaka, 5P-D4-25 (2003)

Takahama T., Isomura M., Tsuda S., Tarui H., Hishikawa Y., Nakumura N., Nakashima Y., Matsuoka T., Hishiwaki H., Ohnishi M., Nakano S., Kuwano Y., Jpn. J. Appl. Phys. **25** (10) 1538 (1986)

Tange S., Inoue K., Tonokura K., Koshi M., Thin Solid Films **395** 42 (2001)

Tauc J., Amorphous and Liquid Semiconductors, Plenum Press, London (1974)

Torres P., Meier J., Flückiger R., Kroll U., Anna Selvan J.A., Keppner H., Shah A., Appl. Phys. Lett. **69** 1373 (1996)

Tsu R., Gonzalez-Hernandez J., Pollack F.H., J. Non-Cryst. Solids 66 109 (1984)

Tsu D.V., Chao B.S., Ovshinsky S.R., Guha S., Yang J., Appl. Phys. Lett. **71** (10) 1317 (1997)

Van Cleef M.W.M., Rath J.K., Rubinelli F.A., Van Der Werf C.H.M., Schropp R.E.I., Van der Weg W.F., J. Appl. Phys. **82** (12) 6089 (1997)

Van Veen M.K., Schropp R.E.I., Thin Solid Films **403-404** 135 (2002)

Van Veen M.K., PhD Thesis, Universiteit Utrecht, (2003)

Van Veen M.K., Schropp R.E.I., J. Appl. Phys. **93** (1) 121 (2003)

Van Veenendaal P.A.T.T., Gijzeman O.L.J., Rath J.K., Schropp R.E.I., Thin Solid Films **395** 194 (2001)

Vetterl O., Finger F., Carius R., Hapke P., Houben L., Kluth O., Lambertz A., Mück A., Rech B., Wagner H., Sol. Energy Mater. Sol. Cells **62** 97 (2000)

Villar F., Escarré J., Fonrodona M., Soler D., Asensi J.M., Bertomeu J., Andreu J., presented at the 3rd aSiNet Workshop on Thin Silicon, Bratislava, (2004)

Vink R.L.C., Barkema G.T., Weg W.F. van der, Phys. Rev. B **63** 115210-1 (2001)

Voz C., Fonrodona M., Soler D., Peiró D., Asensi J.M., Bertomeu J., Andreu J., Proceedings of the 16th ECPVSEC, Glasgow, 417 (2000)

Voz C., Peiró D., Bertomeu J., Soler D., Fonrodona M., Andreu J., Materials Science and Engineering B **69-70** 278 (2000b)

Voz C., PhD Thesis, Universitat de Barcelona (2001)

Voz C., Martín I., Orpella A., Puigdollers J., Vetter M., Alcubilla R., Soler D., Fonrodona M., Bertomeu J., Andreu J., Thin Solid Films **430** 270 (2003)

Voz C., Martin I., Orpella A., Vetter M., Puigdollers J., Alcubilla R., Soler D., Fonrodona M., Bertomeu J., Andreu J., Proc. 3rd World Conference on Photovoltaic Energy Conversion Vol. B 1225 Osaka (2003b)

Wagner S., Gleskova H., Cheng I-C., Wu M., Thin Solid Films **430** 15 (2003)

Waldauf C., Schilinsky P., Hauch J., Brabec C.J., Thin Solid Films **451-452** 503 (2004)

Wang Q., Iwaniczko E., Xu Y., Gao W., Nelson B.P., Mahan A.H., Crandall R.S., Branz H.M., Mat. Res. Soc. Symp. Proc. **609** A4.3.1 (2000)

Wang Q., Page M.R., Xu Y., Iwaniczko E., Williams E., Wang T.H., Thin Solid Films **430** 208 (2003)

Wanka H.N., Zedlitz R., Heintze M., Schubert M.B., Proc. of the 13th European Photovoltaic Solar Energy Conference, Nice, 1753 (1995)

Wanka H.N., Schubert M.B., Lotter E., Solar Energy Materials & Solar Cells **41-42** 519 (1996)

Weber U., Koob M., Dusane R.O., Mukherjee C., Seitz H., Schröder B., Proc. of the 16th European Photovoltaic Solar Energy Conference, Glasgow, 286 (2000)

Wiesmann H., Ghosh A.K., McMahon T., Strongin M.J., J. Appl. Phys. **50** 3752 (1979)

Xu X., Yang J., Guha S., J. Non-Cryst. Solids **198-200** 60 (1996)

Yamaguchi M., Morigaki K., Phil. Mag. B **79** (3) 387 (1999)

Yamaguchi M., Solar Energy Materials & Solar Cells **75** 261 (2003) *and references therein*

Yamamoto K., presented at the 29th IEEE Photovoltaic Specialist Conference (2002)

Yue G., Han D., Williamson D.L., Yang J., Lord K., Guha S., Appl. Phys. Lett. **77** (20) 3185 (2000)

Zedlitz R., Kessler F., Heintze M., J. Non-Cryst. Solids **164-166** 83 (1993)

Ziegler Y., PhD Thesis, Universite de Neuchatel (1997)

Acronym list

α: optical absorption coefficient
α_{dec}: decomposition efficiency
A_f: filament area
AM1.5: Air Mass 1.5
AMLCD: active matriz liquid crystal display
a-Si: amorphous silicon
a-Si:H: hydrogenated amorphous silicon
Cat-CVD: Catalytic Chemical Vapour Deposition
CE: collection efficiency
C_H: hydrogen content
CVD: Chemical Vapour Deposition
CPM: Constant Photocurrent Method
c-Si: crystalline silicon
d: thickness
d_i: intrinsic layer thickness
d_p: p-type layer thickness
$d_{f\text{-}s}$: filament-substrate distance
D_H: hydrogen dilution
DICE: dynamic inner collection efficiency
DOS: density of states
$\Delta\theta$: root-mean-square bond-angle variation
ε: pseudoelectric dielectric function
E_A: dark conductivity activation energy
E_c: conduction band energy
E_F: Fermi level
E_g: optical band gap
E_i: internal electric field
E_u: Urbach front energy
E_v: valence band energy
FPD: flat panel display
ϕ: flux
FF: fill factor
FTIR: Fourier Transform Infrared Spectroscopy
G: generation rate
η: solar cell efficiency
HIT: heterojunction with thin layer
Hot-Wire CVD: Hot Wire Chemical Vapour Deposition
ITO: indium tin oxide
$j_{n(p)}$: electrons (hole) currents
J: current density
J_{dio}: diode current density
J_{ph}: photogenerated current density
J_{rec}: recombination current density
J_{sc}: short circuit current density
k: extinction coefficient

L_D: diffusion length
λ_{mfp}: mean free path
mc-Si: multicrystalline silicon
μ: mobility
μc-Si:H: hydrogenated microcrystalline silicon
$\mu\tau$: mobility-lifetime product
n: refraction index
N_A,N_D: acceptor, donor concentrations
N_d: midgap density of states
N_{DB}: dangling bond density
nc-Si:H: hydrogenated nanocrystalline silicon
P: pressure
PDS: Photothermal Deflection Spectroscopy
PECVD: Plasma Enhanced Chemical Vapour Deposition
PID: Proportional-Integral-Derivative
pm-Si:H: hydrogenated polymorphous silicon
Q: trapped charge
R: recombination rate
R^*: microstructure factor
r_d: deposition rate
RF: radio frequency
R_{oc}: open circuit resistance
R_p: parallel resistance
R_s: series resistance
R_{sc}: short circuit resistance
S: recombination velocity
S: photoresponse
σ: dark conductivity
σ_d: dark conductivity at room temperature
σ_{ph}: steady state photoconductivity
$\sigma_\perp$: conductivity in the direction perpendicular to the substrate
SIMS: Secondary Ion Mass Spectrometry
SS: stainless steel
SSPC: Steady State Photoconductivity
SSPG: Steady-State Photocarrier Grating technique
TFT: thin film transistor
TCO: transparent conductive oxide
τ_{eff}: effective lifetime
T_f: filament temperature
T_s: substrate temperature
VIM: Variable Illumination Measurement technique
V_{bi}: built-in voltage
V_c: collection voltage
V_{oc}: open circuit voltage
V_T: threshold voltage
X_c: crystalline fraction

Figure list

d_i on the collection properties. A 5-layer model exhibiting decreasing CE at increasing d_i (a) and a 6-layer model including a death zone with increasing thickness at higher d_i (b) were considered.

Figure 7.7. *Simulated electric field profile (a) and band diagram (b) for different N_{DB} values giving evidence of the dramatic influence of dangling bonds on the photovoltaic performance.*

Figure 7.8. *Numerical simulation of the spectral response for solar cells exhibiting active layers with different thicknesses and N_{DB} values: 10^{15} cm^{-3} (a), 10^{16} cm^{-3} (b), 10^{17} cm^{-3} (c) and 10^{18} cm^{-3} (d). Experimental results are also presented for comparison (e).*

Figure 7.9. *Electric field profile as a function of d_i for $N_{DB} = 10^{17}$ cm^{-3}.*

Figure 7.10. *G and R at λ = 450 nm (a) and λ = 700 nm (b). High R is obtained in the doped layers due to their high defect concentration.*

Figure 7.11. *Simulated electric field profile for a contaminated (p-type) active layer. Note the enhanced (weakened) electric field in the i/n (p/i) interface at increasing N_A values.*

Figure 7.12. *Numerical simulation of the spectral response of solar cells exhibiting contaminated (100 nm) active layers. Two different N_A values were considered: 10^{17} cm^{-3} (a) and 5×10^{16} cm^{-3} (b).*

Table list

Resum en català

1. Introducció

L'estudi de fonts d'energia renovables ha estat objecte de gran interès des que la inviabilitat d'un panorama energètic dominat per les fonts d'energia tradicionals es posà de manifest. Tant l'augment de la sensibilitat ecològica com la escassetat dels combustibles emprats fins ara porten la humanitat a cercar formes alternatives d'energia. D'entre aquestes, l'obtenció d'energia de la radiació solar a través del conegut efecte fotovoltaic es presenta com a una de les alternatives més prometedores. La tecnologia fotovoltaica proporciona una forma d'energia neta i fàcilment integrable dins les nostres ciutats, a diferència del que succeeix amb altres tecnologies igualment netes, com ara l'eòlica, però difícilment integrables.

El ventall de materials que permeten obtenir dispositius fotovoltaics a partir dels quals extreure energia de la radiació solar és ampli. D'entre aquests però, el silici ha estat el més abastament acceptat al llarg de les darreres dècades degut, fonamentalment, al seu baix cost, al seu caràcter innocu i a les seves adequades propietats optoelectròniques. A més, el silici és un element molt abundant, fet que repercuteix directament en una reducció dels costos de producció. En definitiva, prop del 99% de la producció de cèl·lules solars per a aplicacions terrestres es basa en materials relacionats amb el silici.

El silici pot presentar-se en múltiples formes, fet que ha dut al desenvolupament de diferents tecnologies. En primer lloc, la tecnologia basada en silici monocristal·lí (c-Si) és la més establerta i permet disposar de cèl·lules solars amb funcionaments adequats i eficiències de conversió (η) superiors al 20% per a mòduls comercials. Tot i així, existeixen una sèrie d'inconvenients associats a la producció de c-Si, relacionats majoritàriament als elevats costos de producció del material cristal·lí d'alta puresa. Aquest fet ha dut al desenvolupament de tecnologies alternatives, com ara la basada en silici multicristal·lí (mc-Si), la qual també ha mostrat la seva capacitat per obtenir mòduls comercials amb elevades eficiències de conversió ($\eta \sim 15\%$). En conjunt, els resultats

obtinguts amb c-Si i mc-Si han dut aquests tecnologies a significar prop del 85% de la totalitat del mercat fotovoltaic per a aplicacions terrestres.

En les últimes dècades l'interès s'ha desplaçat cap a la fabricació de dispositius mitjançant tecnologies en capa prima, les quals permeten reduir encara més els costos degut, principalment, a la simplicitat dels processos de fabricació i a la necessitat d'una quantitat molt inferior de material. Cal tenir en compte que gruixos de l'ordre d'1 μm permeten obtenir rendiments acceptables amb dispositius en capa prima, mentre que cal incrementar aquests gruixos fins al voltant de 300 μm per tenir funcionaments dignes amb tecnologies basades en silici en fase volúmica (c-Si o mc-Si). Les característiques del silici en capa prima poden variar dins un ampli rang, definit principalment per la relació entre les seves fases amorfes i cristal·lines. En particular, el silici amorf hidrogenat (a-Si:H), el qual ha portat al desenvolupament de la tecnologia en capa prima més abastament emprada, presenta una estructura bàsicament desordenada. Malauradament, l'a-Si:H pateix de fenòmens de metaestabilitat quan és sotmès a la llum (!), els quals resulten en la degradació de les propietats del material (efecte Staebler-Wronski) fins arribar a un estat de saturació. Com és obvi, aquest efecte constitueix un seriós inconvenient per a l'aplicació d'aquest material a cèl·lules solars. Aquest fet ha dut els diferents grups d'investigació al dipòsit de materials en capa prima amb cert grau d'ordre en forma de petits cristalls: silici microcristal·lí (μc-Si:H) o nanocristal·lí (nc-Si:H), en funció de la mida d'aquests cristalls, els quals presenten una major estabilitat en ser exposats a la llum.

El material objecte del nostre estudi ha estat el silici amorf obtingut mitjançant la tècnica de dipòsit químic en fase vapor assistit per filament calent (Hot Wire Chemical Vapour Deposition, Hot-Wire CVD). Aquesta ha estat emprada en contraposició a la tècnica més àmpliament usada per al dipòsit de capes primes de silici: el dipòsit químic en fase vapor assistit per plasma (Plasma Enhanced Chemical Vapour Deposition, PECVD). En la tècnica de Hot-Wire CVD, una barreja de gasos (en el nostre cas silà, SiH_4, i hidrogen, H_2) és introduïda a la cambra de dipòsit, on s'hi disposa un filament calent escalfat fins a temperatures de l'ordre de 1500 – 2000ºC. El filament dóna lloc a un procés catalític de dissociació de les molècules que entren en contacte amb ell, i les espècies alliberades donen lloc a diferents processos en fase gas (amb altres espècies dissociades al filament o amb molècules de SiH_4/H_2), els resultats de les quals constitueixen els precursors del

creixement. Aquesta tècnica presenta una sèrie d'importants avantatges respecte al PECVD, especialment quan es té en compte la posterior aplicació a nivell industrial, com són els baixos costos associats a la seva implementació i posterior manteniment, o els elevats ritmes de dipòsits aconseguits. Cal remarcar que la recerca en l'àmbit de la tècnica de Hot-Wire CVD a nivell mundial ha portat a l'obtenció de cèl·lules solar amb eficiències inicials de conversió al laboratori per sobre del 8%, mostrant d'aquesta manera el potencial de la tècnica.

Pel que fa a la recerca duta a terme a la Universitat de Barcelona, els primers estudi referits a l'obtenció d'a-Si:H (amb PECVD) es dugueren a terme a finals dels anys 80. Aquests estudis van permetre obtenir a-Si:H amb bones propietats optoelectròniques, així com desenvolupar un ampli conjunt d'eines per al seu dipòsit i caracterització. Pel que fa a la tècnica del Hot-Wire CVD, els primers estudis es van focalitzar en el dipòsit de μc-Si:H i nc-Si:H, obtenint-se material amb bones propietats optoelectròniques així com, recentment, cèl·lules solars amb rendiments estabilitzats satisfactoris.

En resum, el principal objectiu del present treball fou l'estudi i optimització del a-Si:H (tant intrínsec com dopat) dipositat mitjançant Hot-Wire CVD per al seu ús en dispositius fotovoltaics. El paper de cadascun dels paràmetres tecnològics involucrats en la tècnica fou analitzat. Per altra banda, es pretenia obtenir les primeres cèl·lules solars basades en a-Si:H obtingudes íntegrament mitjançant Hot-Wire CVD en el nostre centre. Finalment, també es desitjava dur a terme estudis preliminars referits a les tècniques de confinament òptic destinades a millorar el comportament dels dispositius.

2. Sistema experimental i tècniques de caracterització

2.1. Sistema de dipòsit

Totes les mostres presentades en el present treball foren dipositades mitjançant Hot-Wire CVD en un sistema dissenyat i construït a la Universitat de Barcelona. L'equip de dipòsit consta de tres cambres d'ultra-alt buit, una de les quals actua com a precambra i incorpora un sistema de polvorització catòdica magnetró, el qual és emprat per al creixement d'òxids conductors i transparents (Transparent Conductive Oxide, TCO). Les altres dues cambres

(reactors), les quals només s'obren a l'aire per realitzar operacions de manteniment (canvi del filament per exemple), són usades pel dipòsit de capes primes de silici. Una d'elles és emprada per al dipòsit de material intrínsec, mentre que l'altra es reserva per al creixement de material dopat (tant tipus *p* com *n*). D'aquesta manera s'eviten els efectes perjudicials de la contaminació creuada.

Pel que fa a la configuració interna dels reactors de Hot-Wire CVD, cadascun d'ells consta dels següents elements: mesuradors de pressió (*P*), calefactor resistiu amb element regulador per al control de la temperatura del substrat (T_s), entrada dels gasos reactius, obturador per controlar l'inici i final del dipòsit, portasubstrats i, finalment, l'element clau de la tècnica, el filament. En el nostre estudi s'empraren filaments de tungstè (W) i de tàntal (Ta). Els filaments de W permeten arribar a temperatures de filament (T_f) més elevades, però esdevenen fràgils quan s'empren T_f baixes degut a la formació de siliciurs a la seva superfície. Com a contraposició, el Ta presenta el comportament invers, ja que la formació de siliciurs és menys significativa, permetent una operació òptima a baixes T_f, però pateix d'una certa tendència a deformar-se a T_f elevades, fet que n'impedeix l'ús en aquest règim. Del comentat fins ara es dedueix que la determinació de T_f juga un paper important. En el nostre cas, aquesta s'ha dut a terme mitjançant pirometria òptica, motiu pel qual cadascuna de les cambres incorpora una finestra.

2.2.Tècniques de caracterització

L'avaluació de les propietats del a-Si:H dipositat requereix d'un elevat nombre de tècniques experimentals, ja que el ventall de característiques (tant estructurals com optoelectròniques) que cal tenir en compte és molt ampli.

Com a primer pas, el gruix de les capes, a partir del qual és determina el ritme de dipòsit (r_d), es mesurà amb un perfilòmetre Dektak 3030 per a totes les mostres. Les característiques microstructurals de les capes foren analitzades mitjançant espectroscòpia d'infraroig per transformada de Fourier (Fourier Transform Infrared Spectroscopy, FTIR) i espectroscòpia Raman. L'espectroscòpia FTIR permet estudiar la resistència del material a l'oxidació, mostrant d'aquesta manera el seu grau de compacitat. A més, les mesures de FTIR també permeten analitzar la incorporació d'hidrogen en el material: tant pel que fa al

seu contingut total (C_H), com a la configuració dels seus enllaços amb els àtoms de silici (Si). Finalment, l'espectroscòpia Raman permet calcular la fracció cristal·lina de les capes (X_c).

Per altra banda, les propietats òptiques del material s'avaluaren mitjançant espectroscòpia de deflexió fototèrmica (Photothermal Deflection Spectroscopy, PDS) i transmitància òptica. Aquestes tècniques permeten obtenir l'espectre d'absorció en tot el rang d'energies d'interès. L'absorció per a energies inferiors a l'amplada de la banda prohibida (gap, E_g) permet quantificar la densitat de defectes profunds en el material. Per altra banda, l'absorció en la zona propera al gap dóna lloc a la determinació de l'amplada de les cues de banda (front d'Urbach, E_u), les quals es relacionen amb el grau d'ordre del material (valors d'E_u baixos són indicatius d'una estructura ordenada). Cal tenir en compte que, tot i tractar-se d'un material amorf, l'a-Si:H presenta cert ordre a curt abast, el qual es tradueix en la relativa semblança de les propietats del a-Si:H i el c-Si. Així, el grau de desordre pot representar-se com la dispersió en els angles i distàncies entre primers veïns. En concret, l'ús d'a-Si:H amb un ordre elevat repercuteix en unes millors propietats del material i del dispositiu, especialment pel que fa al capítol de l'estabilitat sota il·luminació prolongada.

Pel que fa a les propietats elèctriques, s'estudiaren la conductivitat en fosc a temperatura ambient (σ_d) i la seva dependència amb la temperatura, a partir de la qual es pot obtenir l'energia d'activació (E_A), la qual permet ubicar el nivell de Fermi dins la banda prohibida. Per altra banda, es dugueren a terme mesures de fotoconductivitat (σ_{ph}) en estat estacionari (*Steady State Photoconductivity*, SSPC) per estudiar les característiques del material sota il·luminació. Finalment, l'avaluació del material tant en fosc com sota il·luminació fou possible a través de la definició de la fotoresposta ($S = \sigma_{ph}/\sigma_d$).

Les cèl·lules solars foren analitzades mitjançant l'adquisició de corbes corrent(tensió) o J(V) sota condicions d'il·luminació estàndard (un sol), les quals permeten obtenir el paràmetres bàsics que defineixen l'operació d'un dispositiu fotovoltaic: tensió en circuit obert (V_{oc}), corrent en curtcircuit (J_{sc}), factor de forma (FF) i eficiència de conversió (η). A més, també es realitzaren mesures per a intensitats d'il·luminació variable (*Variable Illumination Measurement*, VIM), a partir de les quals és possible extreure informació addicional referida tant a aspectes físics com tecnològics (resistències paràsites) de les

cèl·lules solars obtingudes. Finalment, també es mesurà la resposta espectral dels dispositius per tal d'analitzar la generació de corrent.

3. a-Si:H i nc-Si:H

És sabut que l'ús de condicions properes a la transició a nc-Si:H permet obtenir a-Si:H amb propietats òptimes per a l'ús en cèl·lules solars degut a cert grau d'ordre. En concret, l'addició d'hidrogen a la cambra de dipòsit afavoreix el creixement d'a-Si:H amb major estabilitat. Conseqüentment, l'ús d'aquest material duu al dipòsit de dispositius amb un millor funcionament estabilitzat. Aquests resultats evidencien la necessitat de disposar d'una avaluació de l'efecte que els paràmetres de dipòsit tenen sobre la estructura del material. En concret, el nostre treball es va centrar en l'anàlisi del paper desenvolupat per T_f, P, la dilució en hidrogen (D_H) i T_s. Aquests paràmetres afecten en gran mesura la naturalesa dels precursors de creixement, els quals condicionen les propietats microestructurals (i de retruc les optoelectròniques) del material.

3.1. Temperatura de filament

L'estudi per tal d'avaluar la influència de T_f en la microestructura de les capes es va realitzar en les següents condicions: T_s = 200 ºC, $P = 3.8\times10^{-2}$ mbar, D_H = 0% i T_f entre 1600 i 1800 ºC. A més, es va emprar un filament de tàntal amb geometria de cistella invertida resultant en $r_d \sim 4$ Å/s. Els nostres resultats van mostrar un increment significatiu en la fase cristal·lina de les capes obtingudes amb $T_f > 1700$ºC. De fet, no només les propietats estructurals van posar de manifest la transició a-Si:H/nc-Si:H, sinó que les propietats optoelectròniques també evidenciaren un important canvi en el comportament de les capes. Per tal d'entendre la tendència observada cal tenir en compte l'evolució de les espècies alliberades pel filament en funció de T_f. És sabut que un increment en T_f porta associat un augment en l'eficiència de descomposició (α_{dec}) de les molècules de SiH_4, de manera que r_d i la concentració d'H dins la cambra s'incrementen. A més, per a T_f elevades s'observa una producció selectiva d'H a expenses de la de H_2. D'entre aquests mecanismes, la producció selectiva de H a T_f elevades va semblar ser el determinant en el nostre cas, ja que r_d es mantingué pràcticament invariable al llarg de tot l'estudi indicant una α_{dec} força constant.

3.2. Pressió

El conjunt de paràmetres usat en aquesta secció fou: T_s = 200 ºC, D_H = 0%, T_f = 1640 ºC i *P* variable entre 2.4×10^{-2} i 1.9×10^{-1} mbar. L'ús de pressions elevades (> 1×10^{-1} mbar) va resultar en el dipòsit de nc-Si:H, arribant-se a obtenir X_c per sobre de 0.75. r_d va mostrar l'increment esperat en augmentar *P* fins a 1×10^{-1} mbar degut al major temps de residència de les espècies i, conseqüentment, a la major probabilitat de col·lisió amb el filament calent. Tot i així, es va observar una davallada en r_d per a les pressions més altes, per a les quals s'obtingué nc-Si:H. En concret, una major concentració d'H a la cambra degut a la major dissociació de molècules de silà podria explicar tant la transició a nc-Si:H com l'obtenció de menors r_d a *P* altes degut a l'atac selectiu del material. Un cop més, la transició al voltant d'aquestes pressions es va manifestar també en les propietats optoelectròniques del material.

3.3. Dilució d'hidrogen

L'ús de dilució d'hidrogen és el mètode més evident per obtenir nc-Si:H. De fet, aquest és el procediment més comunament emprat pels diferents grups d'investigació, essent abastament usat en el dipòsit mitjançant PECVD. Com és lògic, l'increment de D_H es tradueix en un augment en la concentració d'hidrogen atòmic dins la cambra, el qual porta al creixement d'un material més ordenat i, finalment, al dipòsit de nc-Si:H. En el nostre cas, D_H es va variar entre 0 i 95% mentre T_s = 200ºC, T_f = 1640ºC i *P* = 3.8×10^{-2} mbar foren emprats. En aquestes condicions, les mostres dipositades a D_H = 75% van mostrar la presència d'una incipient fase cristal·lina, mentre que una fracció cristal·lina significativa ($X_c \sim 0.65$) fou mesurada per a la mostra crescuda amb D_H = 95%.

3.4. Temperatura de substrat

La influència de la temperatura de substrat en la cristal·linitat de les mostres fou també analitzada. T_s afecta la mobilitat superficial de les espècies precursores del creixement a través de diferents mecanismes que es contraposen. Per una banda, l'ús de T_s altes incrementa la mobilitat superficial de les espècies degut a l'aportació addicional d'energia però, per altra banda, l'increment de T_s dóna lloc a una major evaporació de l'hidrogen de

la superfície del substrat, reduint d'aquesta manera la mobilitat superficial. Per tal d'analitzar el paper d'aquests mecanismes es van dipositar dues sèries. La primera d'elles es va obtenir amb $D_H = 0\%$, $P = 1\times10^{-2}$ mbar, $T_f = 1550$ºC i T_s entre 300 i 500ºC, mentre que per a la segona es van emprar condicions que afavoriren la producció d'H: $D_H = 93\%$, $P = 3.0\times10^{-2}$ mbar i $T_f = 1600$ºC. Els resultats obtinguts van mostrar la impossibilitat d'obtenir nc-Si:H en la primera sèrie (fins i tot amb les T_s més altes), indicant com a insuficient l'increment en la mobilitat associat a T_s. En canvi, en la segona sèrie es va observar un creixement monòton de la cristal·linitat (fins a $X_c \sim 0.55$).

En resum, els resultats obtinguts en aquest capítol van posar de manifest la nostra capacitat per obtenir capes fines de silici amb un ampli ventall de microestructures: des de la purament amorfa ($X_c = 0$) fins a l'altament cristal·lina ($X_c > 0.7$). L'ús d'elevats valors de T_f, P o D_H van dur al dipòsit de nc-Si:H, essent l'increment en la producció d'H el mecanisme fonamental darrera aquesta transició. Una major concentració de H afavoreix la mobilitat superficial de les espècies i l'atac selectiu del material dipositat, explicant d'aquesta manera l'obtenció de nc-Si:H. Pel que fa a T_s, l'ús de T_s altes va permetre l'obtenció de nc-Si:H només quan la resta de paràmetres (D_H i P) van ser traslladats a un rang favorable per a la producció d'H.

4. a-Si:H intrínsec per Hot-Wire CVD

L'a-Si:H ha de satisfer una sèrie de requeriments per poder ésser considerat material amb qualitat de dispositiu. Així, tant les propietats estructurals com les optoelectròniques han de ser estudiades a fi d'avaluar la qualitat del material. Pel que fa a les propietats estructurals, la primera condició que cal satisfer és que el material sigui dens i no presenti una estructura excessivament desordenada, duent d'aquest mode a bones propietats optoelectròniques i d'estabilitat. Les propietats elèctriques juguen un paper molt destacat, ja que són les que determinen si els portadors generats són col·lectats. En concret, cal que el material presenti una baixa conductivitat en fosc ($\sigma_d < 10^{-10}\ \Omega^{-1}cm^{-1}$), indicant d'aquesta manera l'absència d'impureses electrònicament actives, i una fotoconductivitat elevada ($\sigma_{ph} > 10^{-5}\ \Omega^{-1}cm^{-1}$), evidenciant les bones propietats de transports dels portadors fotogenerats. Finalment, i pel que fa referència a les propietats òptiques, un ample de la

banda prohibida d'entre 1.6 i 1.8 eV i un coeficient d'absorció a 600 nm per sobre de 2×10^4 cm^{-1} són requerits per tal d'optimitzar l'absorció de la llum incident.

Pel que fa referència al nostre millor a-Si:H, aquest presentà una densitat elevada, mostrant-se resistent a l'oxidació segons les mesures de FTIR. Per altra banda, el grau d'ordre fou lleugerament inferior a l'habitualment obtingut amb altres tècniques (PECVD). Tot i així, valors del front d'Urbach lleugerament per sobre de 50 meV indicaren un grau d'ordre prou satisfactori. Coherentment, s'obtingueren valors de la densitat de defectes a la banda prohibida al voltant de 5×10^{16} cm^{-3}, essent aquest un valor també superior a l'obtingut amb PECVD ($\leq 10^{16}$ cm^{-3}). Pel que fa a les propietats elèctriques, es va dipositar material amb $\sigma_d \sim 10^{-10}$ $\Omega^{-1}cm^{-1}$, E_A entre 0.8 i 0.9 eV i σ_{ph} per sobre de 5×10^{-5} $\Omega^{-1}cm^{-1}$, mostrant-se aquests valors dins els marges establerts per al material de qualitat. Finalment, $E_g \sim 1.7$ eV fou obtingut, essent aquest un valor típic per al a-Si:H. De les propietats anteriorment esmentades es dedueix que el material obtingut va mostrar propietats prou satisfactòries per a la seva implementació en dispositius fotovoltaics, tot i un grau de desordre lleugerament superior, el qual sembla ser conseqüència d'una incorporació d'hidrogen excessiva ($C_H \sim 11\%$) degut, molt probablement, al baix valor de T_s emprat (≤ 200ºC). Cal recordar que l'ús de baixes T_s limita la mobilitat superficial de les espècies precursores del creixement i, per tant, és esperable que ens condueixi a material amb cert grau de desordre i, finalment, a estructures poroses.

A continuació es resumiran les condicions de dipòsit pel nostre millor a-Si:H i es mostrarà la influència que els diferents paràmetres van exercir sobre l'a-Si:H dipositat. Com a primera aproximació, podem dir que $T_f \sim 1600$ºC, permetent una adequada generació d'hidrogen atòmic, pressions intermitges (entre 1×10^{-2} i 4×10^{-2} mbar), resultant en espècies precursores del creixement amb elevada mobilitat superficial, i nul·la (o molt baixa) dilució en hidrogen van ser emprats. Pel que fa a l'estudi de la influència de cadascun dels paràmetres, s'observa una gran dependència de la qualitat de les capes d'a-Si:H amb la quantitat d'H i amb la naturalesa de les espècies precursores com es mostra a les seccions següents. Cal dir que les condicions de dipòsit emprades per a l'estudi de cadascun dels paràmetres (secs. 4.1-4.3) foren similars a les ja presentades en el *Capítol 3* (secs. 3.1-3.3).

4.1. Temperatura de filament

L'ús de temperatures entre 1550 i 1650ºC va dur al dipòsit d'a-Si:H amb bones propietats. Lleugeres variacions en les reaccions gas-metall entre les espècies introduïdes al reactor (SiH_4 i H_2) i el filament semblaren tenir doncs un efecte força crític en les espècies generades. En concret, el paper de l'H es mostrà com a clau, de manera que el rang intermig semblà conduir a la producció escaient d'H. L'ús de T_f per sota de 1500ºC va resultar en la degradació del filament i en una producció insuficient d'H. En canvi, i per a T_f per sobre del rang esmentat, l'excessiva producció d'H resultà en el dipòsit de nc-Si:H (*Capítol 3*). Cal tenir en compte que la generació d'H no depèn només de T_f, sinó que les característiques del filament també hi tenen un paper destacat. Així, l'ús de filaments lineals amb menor àrea que els de geometria de cistella invertida va dur a la necessitat d'incrementar T_f per tal de generar una quantitat similar de H .

4.2. Pressió

La pressió de procés determina el recorregut lliure mig (λ_{mfp}) de les espècies dins la cambra de dipòsit, de manera que quan més baixa és *P*, menor és la probabilitat de patir col·lisions i major és λ_{mfp}. La probabilitat de patir reaccions secundàries també depèn de la distància entre el filament i el substrat ($d_{f\text{-}s}$), de manera que *P* i $d_{f\text{-}s}$ es troben estretament lligats. Un nombre insuficient de reaccions secundàries (degut a una *P* i/o a una $d_{f\text{-}s}$ molt baixa) dóna lloc a material de baixa qualitat degut a que bona part del Si generat al filament (el qual presenta una mobilitat molt baixa) actua com a precursor del creixement. Per altra banda, l'ús de *P* i/o $d_{f\text{-}s}$ excessivament elevades es tradueix en un excessiu nombre de reaccions secundàries que dóna lloc a espècies que també presenten baixa mobilitat superficial. Així, els millors resultats es van obtenir en el rang intermig, en concret a $P{\cdot}d_{f\text{-}s} \sim 4 - 12$ ($\times 10^{-2}$) Pa(mbar)·cm, pels quals es produí el nombre de reaccions escaients per generar espècies precursores del creixement amb mobilitat elevada (SiH_3 per exemple).

4.3. Dilució en hidrogen

Tenint en compte el paper determinant de l'hidrogen atòmic i els resultats mostrats al capítol anterior, és obvi que lleugeres variacions en D_H poden dur al material a variar de

forma molt significativa les seves propietats. Tot i així, en el nostre cas només es va observar una lleugera millora en el propietats quan s'usaren dilucions moderades ($D_H \sim 25\%$). L'ús de valors més elevats van resultar en a-Si:H amb propietats no acceptables per al seu ús en cèl·lules solars o, com s'ha vist al *Capítol 3*, en la cristal·lització del material. Aquest resultat apunta a una eficient generació de H, fet que és característic de la tècnica de Hot-Wire CVD, i que sembla encara més afavorit per la geometria del nostre sistema.

5. Material dopat obtingut mitjançant Hot-Wire CVD

L'obtenció de material dopat de qualitat (tant tipus *p* com *n*) juga un paper fonamental en la fabricació de dispositius fotovoltaics, ja que el funcionament d'aquests depèn en bona part del comportament de les capes dopades situades als extrems de l'estructura. La possibilitat de dopar a-Si:H no va ser demostrada fins a mitjans de la dècada dels 70, fet que va disparar un gran interès pel material degut a les aplicacions que aquest fet obria en el camp de la microelectrònica. Fins aleshores es creia que l'estructura desordenada del material permetia als àtoms dopants incorporar-se amb la seva coordinació ideal, impedint d'aquesta manera l'efecte de dopatge. La tècnica del Hot-Wire CVD ha mostrat la seva capacitat per obtenir a-Si:H intrínsec amb propietats comparables a les del material obtingut amb PECVD, però s'han publicat poc estudis referits al creixement de material dopat. En el nostre treball es va estudiar el dipòsit d'a-Si:H tipus *n*, mentre que pel que fa al material tipus *p*, es va analitzar la possibilitat d'emprar tant nc-Si:H com a-Si:H. Finalment, i tenint en compte la incorporació del material al dispositiu final, es va estudiar la influència de les propietats del substrat en les propietats del material dopat dipositat. En aquest sentit, és important recordar que, independentment de l'arquitectura usada (*p-i-n* o *n-i-p*), sempre és una capa dopada la que es diposita directament sobre el substrat.

5.1. Material dopat tipus n

Els principals requeriments que ha de satisfer l'a-Si:H tipus *n* per ser incorporat en una cèl·lula solar son: σ_d elevada ($> 10^{-3}\ \Omega^{-1}cm^{-1}$), E_A baixa (< 0.3 eV) indicant la proximitat del nivell de Fermi a la banda de conducció, i un coeficient d'absorció baix per tal de minimitzar les pèrdues òptiques. Pel que fa referència al darrer punt esmentat, cal tenir en

compte que els portadors generats a les capes dopades no contribueixen al corrent col·lectat degut a les pobres propietats de transport del material dopat, de manera que la generació en elles ha de ser reduïda tant com sigui possible.

En el nostre cas, les mostres tipus *n* foren obtingudes mitjançant l'addició de fosfina (PH_3) a la barreja de gasos. La resta de paràmetres es mantingueren al voltant dels que resultaren en a-Si:H intrínsec de qualitat: *P* entre 1×10^{-2} i 3×10^{-2} mbar, T_s = 200 ºC, D_H = 0% i T_f = 1640 ºC. Per altra banda, una relació d'àtoms de fòsfor a àtoms de silici en fase gas ([P]/[Si]) de l'1% fou emprada. Aquestes condicions van permetre obtenir capes amb bones propietats elèctriques: $\sigma_d \sim 1.5\times10^{-2}\ \Omega^{-1}cm^{-1}$ i $E_A \sim 0.25$ eV, valors comparables (o fins i tot lleugerament superiors) als exigits per a l'ús del material en dispositius. Per altra banda, les mesures de FTIR i PDS mostraren un desordre superior al del a-Si:H intrínsec, essent aquest fet atribuïble al desordre introduït pels àtoms de P.

5.2.Material dopat tipus p

El dopatge tipus *p* del material es va aconseguir mitjançant la introducció de diborà (B_2H_6) al reactor. És sabut que el dipòsit d'a-Si:H tipus *p* amb Hot-Wire CVD presenta més dificultats que quan s'empra PECVD. A més, la il·luminació de les cèl·lules solars es realitza a través d'aquesta capa, motiu pel qual és especialment important reduir al màxim la seva absorció òptica. En aquest sentit, l'ús de nc-Si:H, el qual presenta un menor coeficient d'absorció i unes propietats elèctriques adequades, es planteja com a alternativa.

- a-Si:H tipus p

De la mateixa manera que en el cas del a-Si:H tipus *n*, en aquest cas també es va partir de les condicions de dipòsit que resultaren en bon a-Si:H intrínsec. Tot i així, T_s va haver de ser reduït a 125ºC degut a la inestabilitat tèrmica del diborà. La dificultat d'obtenir a-Si:H tipus *p* de qualitat amb Hot-Wire CVD es va posar de manifest, de manera que només es van poder obtenir propietats comparables a les habitualment mesurades amb PECVD després d'emprar relacions en fase gas ([B]/[Si]) molt elevades (al voltant del 10%) o després de realitzar un recuit de les mostres (a temperatures al voltant de 375ºC durant 1 hora) per a les mostres obtingudes amb una relació estàndard de l'1%. Aquests recuits

van semblar induir un procés d'activació del dopant, possiblement degut a l'evaporació d'hidrogen, el qual es trobaria en el material de manera excessiva i enllaçat amb àtoms de bor, impedint d'aquesta manera l'actuació d'aquests últims com a elements dopants. Així, σ_d va augmentar d'1×10^{-6} a $1\times10^{-4}\ \Omega^{-1}cm^{-1}$, i E_A va disminuir de 0.55 a 0.4 eV, després de dur a terme els esmentats recuits.

- nc-Si:H tipus p

L'ús de nc-Si:H dopat *p* va permetre obtenir material *p* amb excel·lents propietats elèctriques ($\sigma_d \sim 2\ \Omega^{-1}cm^{-1}$ i $E_A \sim 0.03$ eV) i coeficient d'absorció força baix. Tot i així, cal tenir en compte que el material nanocristal·lí incorpora una significativa fase amorfa, fet que duu el material a presentar una absorció no tan baixa com es podria predir del perfil d'absorció del material purament cristal·lí (c-Si). A més, resultats recentment publicats mostren l'efecte beneficiós d'emprar nc-Si:H amb X_c moderades. Per altra banda, es va estudiar el dipòsit de capes *p* primes (gruixos al voltant de 50 nm) per tenir en compte la posterior incorporació al dispositiu, obtenint-se propietats comparables a les observades amb capes gruixudes després de variar lleugerament els paràmetres de dipòsit. Aquest estudi es considera especialment crític en aquest cas (nc-Si:H) degut a la influència que els primers estadis dels creixement poden exercir sobre la microstructura de les mostres.

En definitiva, la possibilitat d'obtenir nc-Si:H tipus *p* amb propietats aptes per a la implementació en cèl·lules solars semblaven assenyalar-lo com a candidat ideal. Tot i així, existeixen alguns inconvenients associats a l'ús de nc-Si:H derivats especialment de la discontinuïtat a les bandes d'energia quan s'empra conjuntament amb una capa intrínseca d'a-Si:H (deguda a la diferent amplada de la banda prohibida) i a l'elevat contingut d'H present a la cambra durant el seu dipòsit. Així, l'ús d'a-Si:H (tot i la limitació en les seves propietats), el de nc-Si:H, i el de combinacions d'ambdós materials fou analitzat en la implementació de dispositius com es mostrarà al *Capítol 6*.

5.3. Influència del substrat

Les propietats de les capes dopades depenen del substrat (morfologia i/o conductivitat). Les cèl·lules solars amb estructura *p-i-n* (emprades en aquesta tesi) presenten una capa *p*

dipositada sobre un TCO, mentre que les *n-i-p* solen presentar una capa *n* crescuda sobre un metall. En el nostre cas es van estudiar les propietats de capes *p* i *n* crescudes alhora sobre vidre, vidre recobert de ZnO:Al i acer inoxidable. Es van emprar condicions properes a la transició a-Si:H/nc-Si:H amb dilució variable (85 – 96 %), T_f = 1800ºC, $P = 3\times10^{-2}$ mbar i T_s = 200 (tipus n) o 125 ºC (tipus p) per tal d'accentuar el possible paper del substrat.

Els resultats obtinguts mostraren la dependència de les propietats elèctriques i les òptiques amb el substrat. L'ús d'acer inoxidable promogué el creixement cristal·lí per al material tipus *n*, mentre que el vidre augmentà la cristal·linitat de les capes tipus *p*. Per altra banda, també es va analitzar el comportament elèctric en la direcció perpendicular al substrat (direcció del moviment dels portadors en el dispositiu real). Aquest comportament es va veure majoritàriament afectat per les propietats de la interfície substrat/capa. Totes les mostres mostraren un comportament lineal de la corba corrent(tensió), fet que demostrà el caràcter òhmic de la unió amb la resistència majoritàriament controlada per la interfície i la fase d'incubació amorfa. El material tipus *n* va mostrar un millor comportament que el tipus *p* independentment de les propietats estructurals. En concret, una caiguda de tensió prou significativa d'entre 20 i 60 mV es mesurà per a la unió TCO/*p* quan corrents similars als esperats en el funcionament estàndard d'un dispositiu fotovoltaic (20 mA/cm^2) foren tingudes en compte. Per altra banda una caiguda menyspreable d'1 mV s'observà per a la unió acer inoxidable/*n* quan el mateix corrent fou considerat. Cal tenir present que aquestes caigudes de potencial repercuteixen directament en el funcionament de la cèl·lula, reduint-ne la màxima potència de treball.

6. Cèl·lules solars

En el present capítol es mostren els primers resultats obtinguts per a cèl·lules solars basades en a-Si:H i dipositades íntegrament mitjançant Hot-Wire CVD a la Universitat de Barcelona. En particular, s'ha prestat especial atenció al funcionament de dispositius amb estructura *p-i-n* crescuts sobre substrats texturats. A més, la temperatura de substrat es va mantenir per sota dels 200ºC per tal de permetre la futura utilització de substrats de baix cost. A continuació es mostrarà l'efecte que diferents estratègies, introduïdes especialment per tal de millorar les propietats dels contactes frontal (TCO i capa *p*) i posterior (capa *n* i

reflector posterior), tingueren sobre el comportament dels dispositiu. Com és lògic, els paràmetres de dipòsit per a les diferents capes (tant intrínseques com dopades) es van seleccionar després de considerar els resultats obtinguts en els capítols anteriors.

Pel que fa al contacte frontal, es va analitzar la implementació de dos tipus diferents de TCO: SnO_2:F (disponible comercialment com a U-Type TCO d'Asahi Glass Co.) i Asahi-U recobert amb una capa de 50 nm de ZnO:Al obtingut al nostre propi laboratori mitjançant polvorització catòdica. Pel altra banda, es van estudiar tres alternatives pel que fa a la capa *p*: a-Si:H, nc-Si:H i una combinació d'una capa amorfa i una altra de nanocristal·lina per tal d'intentar aprofitar els avantatges que l'ús de cadascun dels materials presenta.

Els millors resultats foren obtinguts amb estructures amb capa *p* íntegrament amorfa crescudes sobre Asahi-U, o amb estructures amb doble capa *p* i obtingudes sobre Asahi-U recobert, amb les quals s'assoliren eficiències de conversió inicials de 4.3 i 4.5% respectivament. L'ús d'Asahi-U va dur a l'obtenció de cèl·lules solars amb comportament força satisfactori degut a les seves òptimes propietats optolectròniques. Dissortadament, el seu ús es va veure restringit al creixement de cèl·lules amb contactes frontals íntegrament amorfs, ja que la presència d'una elevada quantitat d'hidrogen atòmic a la cambra durant el dipòsit de nc-Si:H n'indueix la reducció (i conseqüent enfosquiment). És per aquest motiu que els millors resultats amb la doble capa *p* (nc-Si:H/a-Si:H) foren assolits amb l'Asahi-U recobert amb ZnO:Al, el qual mostra una elevada resistència als processos de reducció associats a la presència d'hidrogen.

Pel que fa al contacte posterior, la implementació del reflector va ser duta a terme amb èxit, resultant-ne un increment significatiu del corrent col·lectat pel dispositiu. En concret, la resposta dels dispositius es va incrementar a longituds d'ona elevades. El reflector introduït va consistir en una capa de TCO dipositada sobre la capa *n* (per evitar la difusió de metalls), una capa de plata (100 nm) amb un excel·lent coeficient de reflexió, i una capa d'alumini (200 nm) per proporcionar un bon contacte amb l'exterior. Pel que fa a la capa *n*, en aquest cas també es va procedir a créixer una estructura de doble capa (a-Si:H/nc-Si:H/reflector), la qual es mostra com la més escaient per tal de suportar el posterior creixement del reflector.

Malauradament, diferents resultats mostraren les limitacions en el comportament de les nostres cèl·lules en tots els casos analitzats, essent especialment dramàtic el baix valor del corrent en curtcircuit (J_{sc}), fins i tot en el cas d'incorporar reflector posterior. Així, J_{sc} va romandre al voltant de 10 mA/cm^2 ens els millors dels casos. El bon comportament del reflector posterior i les observacions dutes a terme mitjançant resposta espectral mostraren un comportament acceptable del material intrínsec i del contacte posterior, de manera que fou el contacte frontal el que va semblar limitar de forma més dràstica el funcionament de les nostres cèl·lules. En concret, la baixa resposta de les cèl·lules solars a longituds d'ona baixes apunta a seriosos problemes al contracte frontal (format pel TCO i la capa *p*) i/o a la interfície p/i. En aquest sentit, l'optimització del recobriment de l'Asahi-U amb ZnO:Al es mostrà necessària per tal de gaudir de les excel·lents propietats de l'Asahi-U. En el nostre cas, l'ús de gruixos elevats de ZnO:Al va dur probablement a certa degradació de les propietats optoelectròniques. Per altra banda, i com s'ha comentat en el *Capítol 5*, l'a-Si:H tipus *p* va mostrar-se com a un material de difícil obtenció a baixes temperatures de substrat. La baixa eficiència de dopatge va obligar a emprar capes *p* força gruixudes (40 nm pels contactes íntegrament amorfs i 50 nm de nc-Si:H i 10 nm d'a-Si:H en els dispositius amb doble capa p). Aquest fet empitjora la transmitància del contacte frontal (limitant així J_{sc}) com va poder observar-se en les mesures de transmitància de capes *p* crescudes sobre vidre amb gruixos d'aquest ordre. Finalment, cal tenir en compte que tot i el comportament acceptable a longituds d'ona elevades, l'elevada densitat d'enllaços no saturats (N_{DB}) és esperable que presenti algun efecte perjudicial degut a la gran influència que la seva presència exerceix sobre els perfils de camp elèctric i de recombinació, especialment a les interfícies. En aquest sentit, s'espera que N_{DB} limiti el gruix de la capa intrínseca (d_i). Cal tenir en compte que valors elevats de d_i permeten incrementar la generació de portadors però, per altra banda, porten a una reducció del camp elèctric intern i a un increment en la distància que els portadors han de recórrer per ésser col·lectats, fets que poden esdevenir crítics per N_{DB} elevada. En el nostre cas, es van obtenir cèl·lules solars amb d_i = 0.2, 0.3 i 0.4 μm, obtenint-se els millors resultats pels dos gruixos majors

7. ***Simulació de cèl·lules solars***

El comportament de dispositius fotovoltaics es va analitzar primerament mitjançant la tècnica basada en l'eficiència de col·lecció dinàmica interna (Dynamic Inner Collection

Efficiency, DICE) i, posteriorment, mitjançant la resolució numèrica de les equacions físiques que descriuen el comportament del dispositiu. En concret, es va estudiar el comportament de dispositius fotovoltaics tant en la situació ideal com en el cas de considerar diferents no-idealitats, especialment les associades al contacte frontal. L'estudi es dugué a terme per tal d'intentar aportar més llum al comportament observat en el capítol anterior pels dispositius obtinguts al nostre laboratori.

Per tal de dur a terme les esmentades simulacions, va ser necessari establir els models òptics que defineixen els coeficients d'absorció dels diferents materials involucrats en el dispositiu: a-Si:H, pel qual es va emprar un model analític i el seu posterior ajust a les dades experimentals, i nc-Si:H, pel qual es va triar un model de medi efectiu en el que es combinen les propietats tant del silici amorf com del cristal·lí i també es va comparar amb mesures experimentals.

Les simulacions realitzades van permetre concloure el paper fonamental de les pèrdues òptiques associades a l'ús de capes *p* excessivament gruixudes. Així, la simulació de la resposta espectral va evidenciar eficiències de col·lecció molt baixes a longituds d'ona curtes, fins i tot en el cas de considerar material intrínsec amb propietats idealment bones.

Per altra banda, la simulació de les respostes espectrals en funció del gruix de la capa intrínseca (0.2, 0.3 i 0.4 μm) va permetre obtenir important informació més subtil referida a la física del dispositiu. En concret, una major degradació de les propietats elèctriques a la zona propera a la interfície p/i va ser observada a mida que d_i fou incrementada, essent aquest resultat comparable a l'experimentalment observat. Com a conseqüència, i tenint en compte que la major part de la radiació amb longitud d'ona curta és absorbida en la regió propera a la interfície p/i, les característiques elèctriques determinaren la resposta del dispositiu en aquesta regió de l'espectre ($\lambda \leq 550$ nm), per a les quals s'observà un empitjorament de la resposta espectral a mida que d_i s'incrementà. Per contra, l'increment en l'absorció òptica per a d_i elevades va dur a millors respostes per a d_i altes en la regió de longituds d'ona llargues, superant l'empitjorament de les propietats elèctriques. En conjunt, les cèl·lules solars van semblar estar elèctricament o òpticament limitades a longituds d'ona curtes o llargues respectivament. Aquest efecte pot ser explicat de diferents maneres. Per una banda, la presència d'una densitat de defectes elevada al

material intrínsec (el nostre a-Si:H presenta valors de N_{DB} al voltant de 5×10^{16} cm^{-3}) condueix la cèl·lula a presentar important pèrdues per recombinació a les zones properes a les interfícies. Per altra banda, les simulacions realitzades també posen de manifest un efecte similar quan es considera una distribució d'impures acceptadores (bor) provenint de la capa p. En aquest cas, s'obté un comportament similar a l'experimental fins i tot en el cas de considerar material intrínsec amb baixa densitat de defectes. Tenint en compte el bon comportament de les cèl·lules solars a longituds d'ona llargues i les propietats satisfactòries mesurades a les capes intrínseques, el problema associat a la inestabilitat química de la capa *p* es planteja com el mecanisme fonamental causant de les dificultats observades.

En definitiva, els resultats mostren la possibilitat d'obtenir cèl·lules solars amb Hot-Wire CVD a baixa temperatura de substrat. Tot i així, la millora de certs aspectes és encara necessària per tal d'optimitzar el funcionament dels dispositius. Tant el material intrínsec com el contacte posterior van mostrar un comportament prou satisfactori però cal introduir una sèrie de millores en el contacte frontal. En concret, l'optimització del TCO és necessària per tal d'aconseguir bones propietats optoelectròniques. A més, la millora de les propietats del material tipus *p*, o fins i tot, l'ús d'a-SiC:H en comptes d'a-Si:H es presenten com a elements claus per millorar el comportament de les cèl·lules.

8. Conclusions

- S'ha estudiat el creixement d'a-Si:H mitjançant la tècnica de Hot-Wire CVD, de manera que la influència dels diferents paràmetres (T_f, P, D_H, T_s) en les propietats del material obtingut ha estat avaluada, permetent l'optimització del material. Tot i així, T_s s'ha mantingut a valors baixos ($T_s \leq 200$ºC) durant la major part dels experiments per tal de mantenir la compatibilitat amb l'ús de substrats de baix cost.

- La possibilitat d'obtenir capes primes de silici amb un ampli ventall de microestructures (des de $X_c = 0$ a $X_c > 0.65$) ha estat demostrada. En particular, la utilització de valors elevats de T_f, P i/o D_H permet el creixement de material altament cristal·lí, fins i tot amb baixes temperatures de substrat. En tots els casos, l'augment en la producció d'hidrogen atòmic s'apunta com el mecanisme responsable de l'esmentat

comportament. També cal destacar que la transició d'a-Si:H a nc-Si:H es produeix de manera abrupta, indicant la influència crítica dels diferents paràmetres de dipòsit. Per altra banda, l'increment de mobilitat superficial associat a l'ús de T_s elevades es va mostrar com a insuficient per aconseguir nc-Si:H, sempre i quan la resta de paràmetres no es modifiquessin a condicions afavoridores de la producció d'hidrogen.

- Es va identificar el conjunt de paràmetres que ens permet obtenir el nostre millor a-Si:H, el qual presenta propietats estructurals i optoelectròniques prou satisfactòries per a la seva implementació en dispositius fotovoltaics. Cal tenir en compte que aquest conjunt depèn críticament de diferents factors geomètrics (àrea del filament, distància filament-substrat, volum de la cambra de dipòsit,...), fet que impedeix una extrapolació a altres sistemes de dipòsit. En qualsevol cas, la natura de les espècies precursores del creixement i la concentració d'hidrogen atòmic es mostraren com els factors que més influeixen en la qualitat de les capes.

  - L'ús de T_f entre 1550 i 1650ºC va produir el nostre millor material degut a la generació adequada d'H. Tot i així, la generació d'hidrogen depèn també de la geometria del filament, de manera que aquestes temperatures tingueren que ser augmentades per a filaments amb àrea més petita.

  - La natura dels precursors del creixement depèn críticament de la pressió i de la distància entre el filament i el substrat: $d_{f\text{-}s}$, de manera que $P \cdot d_{f\text{-}s} \sim$ 4-12 Pa·cm permet el dipòsit del nostre millor material degut a un adequat nombre de reaccions secundàries. Tenint en compte la nostra geometria ($d_{f\text{-}s}$ entre 3 i 5 cm), P fou variada entre 1×10^{-2} i 3×10^{-2} mbar.

  - La influència de D_H fou especialment crítica ja que la generació d'H en el nostre reactor és molt eficient. Conseqüentment, l'ús de dilució no sembla necessari i només s'observà una millora subtil per a valors moderats ($D_H \leq 25\%$). De fet, valors més elevats d'aquest paràmetre poden dur al creixement de material de baixa qualitat o a nc-Si:H.

- La possibilitat de dopar el nostre material (tant tipus *p* com *n*) mitjançant Hot-Wire CVD a través de l'addició de B_2H_6 o PH_3 a la barreja de gasos fou analitzada.

  - L'a-Si:H tipus *n* amb bones propietats fou aconseguit amb el mateix conjunt de paràmetres que dugueren al millor material intrínsec. Una relació d'àtoms en fase gas ([P]/[Si]) de l'1% portà a bones propietats elèctriques (($\sigma_d > 10^{-3}\ \Omega^{-1}cm^{-1}$ i $E_A < 0.3$ eV).

- El dipòsit d'a-Si:H tipus *p* amb bones propietats es va mostrar com un procés força més complex, ja que les propietats elèctriques obtingudes amb el conjunt de paràmetres anterior foren insuficients per al seu ús en cèl·lules solars ($\sigma_d \sim 10^{-6}\ \Omega^{-1}cm^{-1}$). Així, calgué emprar relacions d'àtoms en fase gas molt elevades ([B]/[Si] ~ 10%) o tractaments de recuit (a 375ºC durant 1 hora) per tal d'assolit propietats elèctriques acceptables ($\sigma_d \sim 10^{-4}\ \Omega^{-1}cm^{-1}$ i $E_A \sim 0.4$ eV). El comportament observat semblà ser conseqüència de l'elevat contingut d'hidrogen de les mostres ($C_H \sim 16\%$), el qual s'enllaça amb el bor impedint la funció com a dopant d'aquest. Mitjançant el recuit de les mostres s'allibera hidrogen del material, de manera que es permet que més àtoms de bor actuïn efectivament com a espècies dopants.

- Les capes dopades són dipositades sobre diferents substrats quan s'incorporen en estructures fotovoltaiques, de manera que la influència del substrat en les propietats del material dipositat ha de ser analitzada. En concret, l'ús d'acer inoxidable va semblar promoure el creixement de material cristal·lí per a mostres tipus *n*. Per altra banda, el creixement de nc-Si:H es veié afavorit pel vidre quan s'estudià el material tipus *p*. Pel que fa a les propietats elèctriques, aquestes es mesuraren en la direcció perpendicular al substrat, evidenciant un comportament dominat bàsicament per les propietats de la unió capa/substrat, les quals foren clarament millors en el cas de les capes tipus *n*.

- El resultats presentats anteriorment foren emprats en el dipòsit de les nostres primeres cèl·lules solars basades en tecnologia d'a-Si:H i íntegrament obtingudes mitjançant Hot-Wire CVD. Aquests primers estudis es van centrar en l'anàlisi de diferents estructures incloent diferents dissenys tant pel contacte frontal com pel posterior. Pel que fa als resultats obtinguts, els millors foren assolits amb dispositius amb contactes frontals íntegrament amorfs crescuts sobre substrats texturats de SnO_2:F (Asahi-U) o amb contactes frontals basats en una doble capa *p* (a-Si:H/nc-Si:H) dipositades sobre Asahi-U recobert amb ZnO:Al. A més, en ambdós casos es va observar una millora en el comportament dels dispositius després d'implementar un reflector posterior per tal d'incrementar l'absorció de llum. En concret, aquests dispositius resultaren en eficiències de conversió inicials del 4.3 i el 4.5% respectivament.

- La resposta dels nostres dispositius en la regió de longituds d'ona llargues va corroborar el comportament acceptable de la capa activa i el contacte posterior, mentre que fou el contacte frontal el que va semblar limitar el comportament dels dispositius. En concret, el corrent en curt-circuit va presentar un valor força baix (10 mA/cm^2) en els casos més favorables. En aquest sentit, dos aspectes es van mostrar com especialment perjudicials. Per una banda, es van trobar dificultats en el TCO emprat, de manera que l'ús d'Asahi-U sense recobrir ens portà a problemes degut a la reducció del mateix, mentre que el seu recobriment amb ZnO:Al es traduí en la degradació de les seves propietats optoelectròniques. Per altra banda, la dificultat de dopar adequadament el material tipus *p* també va provocar serioses dificultats, essent la més crítica la necessitat d'emprar capes molt gruixudes per assegurar un bon funcionament del díode. Com a contrapartida, aquestes capes tan gruixudes provocaren pèrdues òptiques per absorció molt significatives.

- El comportament de les nostres cèl·lules solars fou simulat mitjançant la tècnica del *DICE* (Dynamic Inner Collection Efficiency) i mitjançant la resolució numèrica de les equacions que defineixen el comportament dels dispositius fotovoltaics. D'acord amb els resultats experimentals, les pèrdues òptiques van manifestar-se com a un dels punts crítics en la limitació del comportament dels nostres dispositius.

- Els resultats obtinguts mitjançant simulació numèrica van mostrar que les propietats elèctriques, les quals empitjoren per a gruixos creixents de la capa activa, determinaren el comportament del dispositiu a longituds d'ona curtes. En canvi, l'increment de l'absorció òptica per a gruixos elevats va dur a un millor funcionament de la cèl·lula solar a longituds d'ona llargues. Aquest comportament fou reproduït després de considerar el valor de la densitat de defectes (N_{DB}) pel nostre millor material i la possible presència d'impureses acceptadores a la interfície p/i. Tenint en compte les propietats acceptables observades en el material intrínsec, aquest segon mecanisme associat a inestabilitats químiques a la capa *p* es proposa com a mecanisme fonamental causant del comportament observat.

- Les nostres primers cèl·lules solars basades en a-Si:H dipositades mitjançant Hot-Wire CVD a baixa temperatura de substrat foren obtingudes. Les propietats del material intrínsec són prou satisfactòries i prometedores de cara a la integració a nivell industrial de

la tècnica seleccionada. Tot i així, aquest pas requereix abans de l'optimització del contacte frontal, tenint especialment en compte el comportament del TCO i la capa dopada tipus *p*.

Annex: Altres aplicacions

Tot i que la major part dels nostres esforços han estat centrats en el desenvolupament d'a-Si:H dipositat mitjançant Hot-Wire CVD per a cèl·lules solars en capa prima, el nostre material fou incorporat també en altres aplicacions. En concret, la viabilitat d'emprar el material crescut al nostre laboratori en transistors en capa prima (*Thin Film Transistor*, TFT) o en cèl·lules solars d'heterounió fou analitzada. Cal dir que aquestes tasques es portaren a terme en col·laboració amb altres centres de recerca. En particular, l'estudi dels TFTs es dugué a terme conjuntament amb la *Université de Rennes 1*, mentre que la recerca relacionada amb les cèl·lules d'heterounió es realitzà en cooperació amb la *Universitat Politècnica de Catalunya (UPC)*.

A.1. Transistors en capa prima

El desenvolupament de TFTs juga un paper molt important degut al gran nombre d'aplicacions que es deriven del seu ús. En concret, cada dia són més el instruments que ens envolten i que disposen de visors de cristall líquid (*active matrix liquid crystal display*, AMLCD): rellotges, telèfons mòbils, ordinadors portàtils, etc. Aquests AMLCD estan formats per una sèrie d'elements (píxels) que conformen la imatge final a partir de l'estat de cadascun d'ells. L'estructura d'aquests elements presenta diverses capes, essent-ne les fonamentals les que es mostren a continuació

polaritzador/vidre/matriu de TFTs/cristall líquid/ITO/vidre/polaritzador

Una font de llum es situa a un dels extrems, mentre que l'observació es realitza per l'extrem oposat. El cristall líquid (LC) és l'element fonamental de l'estructura mostrada, ja que el seu estat determina si el píxel és clar o fosc. Igualment important és la matriu de TFTs, la qual presenta tants elements com píxels té el display. De fet, és l'estat dels TFT

(on, off) el que determina l'estat del cristall líquid i, per tant, si el píxel deixa (clar) o no deixa (fosc) passar la llum a través seu.

D'acord amb aquesta aplicació, els TFTs, els quals actuen com a interruptors, han de satisfer una sèrie de requeriments bàsics:

- Corrents en estat de conducció elevats per tal de permetre transicions clar/fosc i viceversa ràpides. En aquest sentit, la mobilitat (μ) dels portadors en el material que conforma el canal del transistor ha de ser alta.
- Corrents de fuites baixos en estat de no conducció per tal d'evitar la descàrrega del sistema a través dels corrents de fuites.
- Tensions llindars (threshold, V_T) o de transició entre els estats de conducció i de tall del transistor baixes.
- Pendent de la transició off/on (S) elevada per assegurar una transició abrupta entre els dos estats.

En concret, els esmentats requeriments poden ser satisfets per l'a-Si:H de qualitat, motiu pel qual es va estudiar la viabilitat del nostre material en aquest tipus de sistema.

En el nostre cas, l'a-Si:H presentat al Capítol 4 de la tesi fou emprat en cooperació amb la *Université de Rennes 1*. Es van dipositar TFTs en configuració top-gate, els detalls de la qual poden trobar-se a l'annex d'aquesta tesi. Els resultats obtinguts foren molt prometedors, obtenint-se valors de S al voltant de 0.6 V/dec indicant una transició força abrupta i V_T al voltant de 3.5 V. Per altra banda, s'assoliren mobilitats al voltant d'1.3 $cm^2V^{-1}s^{-1}$, essent aquest valor comparable (o fins i tot superior) als millors valors reportats fins ara. Pel que fa a l'estabilitat dels TFTs, s'observà un mecanisme de degradació que es traduí en un desplaçament de V_T d'uns 5 V, essent aquest resultat atribuïble a una elevada densitat de defectes al material deguda probablement a l'ús de baixes temperatures de substrat ($T_s \sim 200$ ºC). Tot i així, els resultats obtinguts foren molt satisfactoris i indicadors de les prometedores propietats del material emprat.

A.2. Cèl·lules solar d'heterounió

El creixement de cèl·lules solars d'heterounió combinant silici cristal·lí (c-Si) i silici amorf (a-Si:H) es troba entre les alternatives més prometedores per assolir eficiències de conversió elevades. En aquest tipus d'estructura, la difusió de la capa dopada que actua com a emissor és substituïda pel dipòsit d'una capa prima, evitant d'aquesta manera l'ús de temperatures elevades. Cal tenir en compte que temperatures al voltant de 1000ºC són necessàries per dur a terme aquests processos de difusió, mentre que T_s d'uns 200ºC són usades pel dipòsit de les capes primes. Fins ara, la major part de la recerca en cèl·lules solars d'heterounió s'ha dut a terme mitjançant PECVD, tècnica que ha permès arribar a eficiències de fins al 19.5% mitjançant la introducció del concepte de cèl·lula solar tipus HIT (*Heterojunction with Intrinsic Thin Film layer*) desenvolupat per Sanyo, en el qual una capa intrínseca molt prima (d'uns 10 nm) és crescuda entre l'oblia (c-Si) i la capa prima dopada dipositada per actuar com a emissor. Pel que fa al dipòsit amb Hot-Wire CVD, valors al voltant d'entre l'11 i el 13 % han estat reportats, mostrant l'elevat potencial de la tecnologia.

En el nostre cas, la col·laboració amb la *Universitat Politècnica de Catalunya* ha dut al creixement d'heterounions amb la següent estructura

contacte posterior(Au)/capa p/capa i/oblia p/capa i/capa n/ITO/contacte frontal (Ti/Ag)

on la doble capa p/i al contacte posterior permet reduir les pèrdues per recombinació. Els materials presentats als Capítols 4 i 5 foren emprats per a les capes de silici en capa prima. S'estudiaren diferents combinacions amb diferents gruixos per a les capes intrínseques i dopades, així com capes dopades d'a-Si:H i nc-Si:H. Els millors resultats s'obtingueren amb capes *p* i *n* de nc-Si:H i a-Si:H respectivament, presentat ambdues gruixos de 50 nm. Per altra banda, la capa intrínseca amorfa entre les capes dopades i l'oblia presentà un gruix de 5 nm. Aquestes condicions van dur a l'obtenció de dispositius amb eficiències al voltant del 9%, amb $V_{oc} \sim 0.58$ V, $J_{sc} \sim 24$ mA/cm^2 i FF ~ 0.65, essent aquest valors molt prometedors i indicant d'aquest mode el potencial de les nostres investigacions.